UNIVERSITY OF CALIFORNIA, SAN DIEGO

Applications Bioinspired by Sea Urchins and Spongy Bone

A dissertation submitted in partial satisfaction of the
requirements for the degree of Doctor of Philosophy

in

Materials Science and Engineering

by

Michael Brian Frank

Committee in charge:

Professor Joanna McKittrick, Chair
Professor Shengqiang Cai
Professor Olivia Graeve
Professor Robert Sah
Professor Mike Tolley

2017

The Dissertation of Michael Brian Frank is approved, and is acceptable in quality and form for publication on microfilm and electronically:

_____

_____

_____

_____

_____

Chair

University of California, San Diego

2017

DEDICATION

In recognition of support throughout my graduate school odyssey, I would like to dedicate this thesis to my wife Emi, my children Layla, Mila and Hugo, my parents Steve and Susie, their dog Shmuley, my brother Dave, my sister-in-law Amy, my nieces and nephew Jana, Eleanor and Evan, and their two dogs, Gracie and Bebop (both deceased). As my research changed due to unforeseen circumstances, each of you provided me with the joy, courage and strength that I needed exactly when I needed it. I couldn't have persevered to finish my Ph.D. without your love and support. Thank you all so much.

I would also like to sincerely thank all the graduate students (Mike Porter, Steven Naleway, Jae-Young Jung, Wei Huang, Frances Su, Yuchen Zhang, Yi-Hsuan "Sharon" Hsiao, Jungmin Ha, Keisuke Matsushita, Sean Garner), undergraduate and high school students (Tsuk Haroush, Alejandro Valdivia, Angelica Esparza, Ming Chengmingjtt, Taylor Wirth, Sandra Medina, Faviola Loera, Charlene Cheung, Sze Hei Siu, Ivan Torres, Khalid Niles-Rodney, Kerry Chou, Jerry Ng, Ali Ismail, Kai Prager, Cindy Ayala, Louis Guibert, Damian Gonzalez, Joyce Mok, Yajur Maker, Chris Yu, Jordan Furlong) I worked with during my time doing research with the McKittrick Group.

Last, but certainly not least, I want to thank Prof. Joanna McKittrick for taking a chance on me and allowing me to join her group in January 2014. I was seriously considering leaving graduate school after everything that had happened before, but she accepted me and then granted me the freedom to be able to find my way towards doing the research work described in this thesis. It has been the most rewarding and creative time in my life, so I'm truly forever thankful to her for seeing some potential in me.

EPIGRAPH

Here's what you get for things that haven't happened yet.

Elliott Smith

TABLE OF CONTENTS

LIST OF FIGURES

LIST OF TABLES

ACKNOWLEDGEMENTS

I would like to gratefully acknowledge my wife, parents and kids for putting up with me throughout my time as a graduate student. I would also like to thank all the mentors who guided me as well as all the undergrads who joined me on the path towards scientific discovery. My research was greatly assisted through samples provided by various suppliers, including Ferrotec (Bedford, NH), Baikowski (Malakoff, TX), Kinsei Matec Co., Ltd. (Osaka, Japan) and Plastic Suppliers, Inc. (Columbus, OH). The work presented in this dissertation was supported by a National Science Foundation Biomaterials Program Grant (1507978) and a Multi-University Research Initiative through the Air Force Office of Scientific Research of the United States (AFOSR-FA9550-15-1-0009).

Chapter 2, in part, is published as "A Protocol for Bioinspired Design: A Ground Sampler Based on Sea Urchin Jaws" Journal of Visualized Experiments, vol. 110, e53554, 2016. This work was coauthored by S.E. Naleway, T.S. Wirth, J-Y. Jung, C.L. Cheung, F.B. Loera, S. Medina, K.N. Sato, J.R.A. Taylor and J.M. McKittrick. The dissertation author is the first and corresponding author of this work.

Chapter 3, in part, is published as "Stiff, porous scaffolds from magnetized alumina particles aligned by magnetic freeze casting" Materials Science and Engineering: C, 77, 484-492, 2017. This work was coauthored by S. E. Naleway, T. Haroush, C-H Liu, S. H. Siu, J. Ng, I. Torres, A. Ismail, K. Karandikar, M. M. Porter, O. A. Graeve and J. M. McKittrick. The dissertation author is the first author of this work.

Chapter 3, in part, is accepted as "Synergistic structures from magnetic freeze casting with surface magnetized alumina particles and platelets" Journal of the Mechanical Behavior of Biomedical Materials, Published Online, 2017. This work was coauthored by

S. H. Siu, K. Karandikar, C-H Liu, S. E. Naleway, M. M. Porter, O. A. Graeve and J. McKittrick. The dissertation author is the first author of this work.

Chapter 3, in part, is in progress as "Biodegradable Spongy Bone Implants: Strength Through Bioinspiration," 2017. This work will be coauthored by A. Ismail, C. Ayala, L. Guibert, K. Karandikar, C-H Liu, S. H. Siu, J. Mok, J. Ng, O. A. Graeve and J. McKittrick. The dissertation author is the first author of this work.

VITA

2017 Ph.D. Materials Science and Engineering

University of California, San Diego

Dissertation: Applications Bioinspired by Sea Urchins and Spongy Bone

Advisor: Professor Joanna McKittrick

2009 M.S. Bioengineering

San Diego State University

Dissertation: High Sensitivity MEMS Biochemical Sensor Using PMN-PT

Advisor: Professor Sam Kassegne

2004 B.S. Psychobiology

University of California, Los Angeles

PUBLICATIONS

Niksiar P, Frank MB, McKittrick J, Porter MM. Microstructural Evolution of Porous Materials by Magnetic Freeze Casting. In progress, 2017.

Zaheri A, Frank MB, McKittrick J, Espinosa H. Direct Measurement of Abrasion Resistance in Sea Urchin Teeth. In progress, 2017.

Frank MB, McKittrick J. Magnetic color wall panels. UCSD Office of Innovation and Commercialization, Docket No. SD2017-296, Submitted e-Disclosure, 2017.

Frank MB, Ismail A, Ayala C, Guibert L, Karandikar K, Liu C-H, Siu SH, Mok J, Ng J, Graeve OA, McKittrick J. Biodegradable Spongy Bone Implants: Strength Through Bioinspiration. In progress, 2017.

Frank MB, Siu SH, Karandikar K, Liu C-H, Naleway SE, Porter MM, Graeve OA, McKittrick J. Synergistic structures from magnetic freeze casting with surface magnetized alumina particles and platelets. Journal of the Mechanical Behavior of Biomedical Materials, Accepted, 2017.

Frank MB, Naleway SE, Haroush T, Liu C-H, Siu SH, Ng J, Torres I, Ismail A, Karandikar K, Porter MM, Graeve OA, McKittrick JM. Stiff, porous scaffolds from magnetized alumina particles aligned by magnetic freeze casting. Materials Science and Engineering: C, 77, 484-492, 2017.

Frank MB, Naleway SE, Wirth TS, Jung J-Y, Cheung CL, Loera FB, Medina S, Sato KN, Taylor JRA, McKittrick JM. A Protocol for Bioinspired Design: A Ground Sampler Based on Sea Urchin Jaws. Journal of Visualized Experiments, 110, 1-8, e53554, 2016.

Li Y, Frank M, Tauber MJ, Jin S, Ryoo J. Electrochemical solar cells. Patent: WO2014165830A2, 2014.

ABSTRACT OF THE DISSERTATION

Applications Bioinspired by Sea Urchins and Spongy Bone

by

Michael Brian Frank

Doctor of Philosophy in Materials Science and Engineering

University of California, San Diego, 2017

Professor Joanna McKittrick, Chair

A protocol for study of a bioinspired sediment sampler progressed through biology, materials science, bioinspiration and bioexploration. First, the natural structure of the sea urchin mouthpiece, Aristotle's lantern, and its open and close mechanism were examined. Second, the Aristotle's lantern and tooth microstructure were analyzed with several materials science characterization methods. Third, a sediment sampler bioinspired by the open and close mechanism of the Aristotle's lantern was designed and fabricated through

an iterative prototyping process. Fourth, engineering analysis methods were used to explain why a tooth reinforcing keel structure evolved in the biology of modern sea urchins.

Magnetic field assisted ice templating, also known as magnetic freeze casting, was used to align surface magnetized ceramic particles in water into chains to make multi-axis strengthened porous scaffolds bioinspired by spongy bone. Magnetized particles aligned in the ice crystal growth direction and into chains to form lamellar walls in the applied transverse magnetic field direction during the magnetic freeze casting process. Aligned lamellar walls in the axis transverse to the ice crystal growth direction stiffened the porous scaffold similarly to spongy bone with multi-axis aligned porosity. Magnetized particle chain alignment in the scaffold center during magnetic freeze casting depended on several factors, including magnetic field strength, magnetized particle moment, particle size, length of time before freezing, slurry temperature and slurry concentration. Magnetic freeze casting was done with different magnetized alumina particle sizes and morphologies followed by mechanical compression in different axes.

A lower magnetic field strength was applied for alignment of larger magnetized hydroxyapatite particles based on preliminary empirical results that agreed with predictive theoretical equations for superparamagnetic particle aggregation in a liquid medium. Radial strengthening by shrink wrapping scaffolds with a biodegradable polymer was bioinspired by keratin based porcupine quills that have a cortex sheath wrapped around a closed cell foam. The porous scaffold microstructure was strengthened by infiltration with a dual network hydrogel that bound to phosphate in the hydroxyapatite lamellar walls to make an interconnected composite structure bioinspired by spongy bone.

CHAPTER 1: BIOINSPIRED RESEARCH BACKGROUND

1.1 Why Bioinspired?

Observation of the natural world around us began when we did and has evolved within us to the point today where bioinspired designs based on natural structures can have functionality extended to new and exciting applications. Aristotle famously observed and wrote about the sea urchin mouthpiece resembling a horn lantern from his time, which led to the natural structure name being identified with its initial observer. Materials scientists have explored bioinspired development of many natural structures around us, including abalone nacre and gecko setae, with an aim towards understanding how natural designs perfected through evolution over millions of years can be applied to benefit mankind. An aim for this dissertation is to focus the incredibly broad realm of bioinspired possibilities down to a few that can be developed for potential applications.

1.2 Bioinspired Research Objectives

Bioinspired research examples reviewed in this dissertation include a sediment sampler based on the sea urchin mouthpiece, Aristotle's lantern (Chapter 2), and a resorbable bone implant based on human trabecular bone (Chapter 3). The primary focus of this work is to elucidate how surface magnetized materials aggregate and align within lamellar walls along an applied magnetic field direction to form multi-axis strengthened porous structures using a recently developed materials processing method called magnetic freeze casting [1]. One aim for this dissertation is to push magnetic freeze casting as a bioinspired research enterprise past the realm of interesting empirical observation and towards one that fits within rational materials design.

This premise begins with a new experimental design predicated upon removal of limitations from materials (e.g. weakly paramagnetic titania) or mixtures (e.g. large quantities of ferromagnetic magnetite nanoparticles) responsible for lamellar wall alignment in previous magnetic freeze casting work [1-4]. A surface magnetization process [5] was used to make any material magnetically responsive, which opened up the magnetic freeze casting materials toolbox far beyond previous limitations of mixtures based on particle interactions between weakly paramagnetic or diamagnetic materials with ferromagnetic materials [1-4]. One model material system with less material variables based on alumina was used to explore other important parameters involved in lamellar wall alignment during magnetic freeze casting, including particle size (Section 3.2) and morphology (Section 3.3) that show no material dependence (Section 3.4). The last part takes aim at implementation of an experimental design that can incorporate exterior and interior strengthening mechanisms for spongy bone implants (Section 3.5). Combination of the bioinspired processes described in Chapter 3 may lead future researchers closer to the fabrication of biocompatible, resorbable spongy bone composite implants that are strong and tough like titanium alloy implants, but without the typically associated stress shielding and bone remodeling problems that go with them.

CHAPTER 2: ARISTOTLE'S LANTERN BIOINSPIRED SEDIMENT SAMPLER

2.1 Introduction to the Sea Urchin Mouthpiece (Aristotle's Lantern)

The fields of biology, biological materials science, biomaterials, bioengineering and biochemistry employ the premiere scientific techniques and minds in an attempt to provide a deeper understanding of the incredible natural world. This research has explained many of the most amazing biological structures and organisms; from the intrinsic toughness of human bone [6, 7] to the large beak of the toucan [8]. However, much of this knowledge is difficult to employ in a manner that can provide a benefit to society. As a result, the tangential field of bioinspiration employs the lessons learned from nature to modern materials in order to solve common problems. Examples include superhydrophobic surfaces inspired by lotus leaves [9-11], adhesive surfaces inspired by the feet of geckos and insects [12, 13], tough ceramics inspired by the nacre of abalone [14-16] and biopsy harvesters inspired by the mouthpiece of the sea urchin, also known as the Aristotle's lantern [17, 18].

Sea urchins are invertebrate animals covered with spines whose habitat most commonly consists of the rocky beds on the ocean floor. The body (called a test) in the largest urchin species can be more than 18 cm in diameter; test size in pink sea urchins (Strongylocentrotus fragilis) examined in this study can grow to 10 cm diameter. The Aristotle's lantern is composed of five predominately calcium carbonate teeth supported by pyramid structures composed of mineralized tissue and arranged into a dome-like formation that enclose all but the distal grinding tips of the teeth (Figure 2.1a).

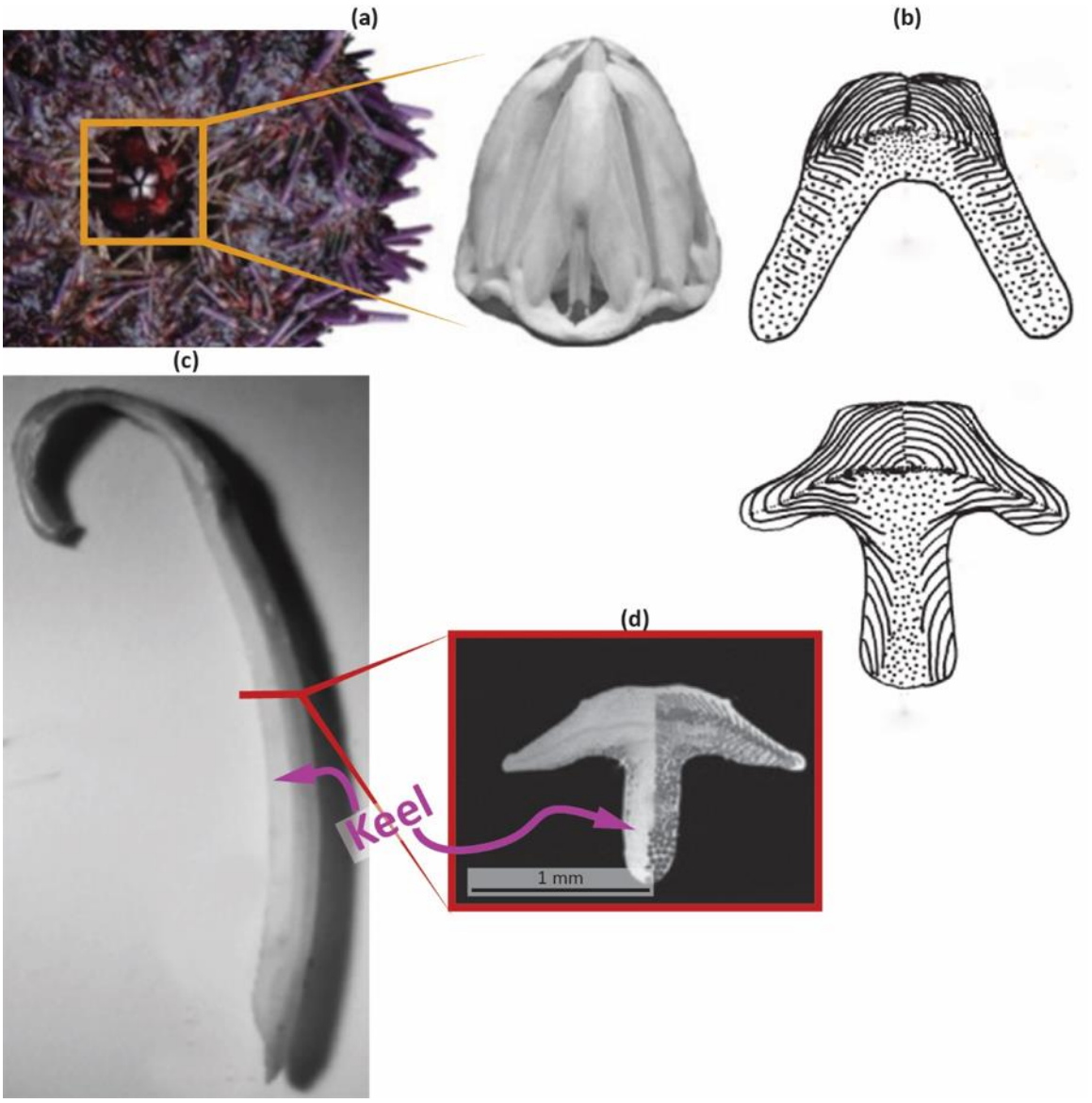

Figure 2.1: Sea urchin Aristotle's lantern and tooth morphology. (a) Close-up of the ventral view of a sea urchin (left) and the Aristotle's lantern (right) [18]. (b) Cross-sections of the grooved tooth of a primitive cidaroid urchin (top) and the keeled tooth of a modern camarodont urchin (bottom) [19]. (c) An isolated tooth seen from its side with the tip (bottom) and indicated keel (left side) [20]. (d) SEM image of a polished tooth cross-section with the indicated keel (bottom) [20]. Images adapted from indicated references for (a), (b), (c) and (d).

The muscle structure of the jaws is capable of efficient chewing and scraping even against hard ocean rocks and corals. When the jaws open, the teeth protrude outwards and when the jaws close, the teeth retract inwards in a single smooth motion. Comparison between primitive (above) and modern (below) sea urchin tooth cross-sections (Figure

2.1b) indicates that a keeled tooth evolved to strengthen the tooth when grinding against hard substrates. Each individual tooth has a slightly convex curvature and a T-shaped morphology in the transverse plane (normal to the growth direction) due to the longitudinally attached keel (Figure 2.1c, d).

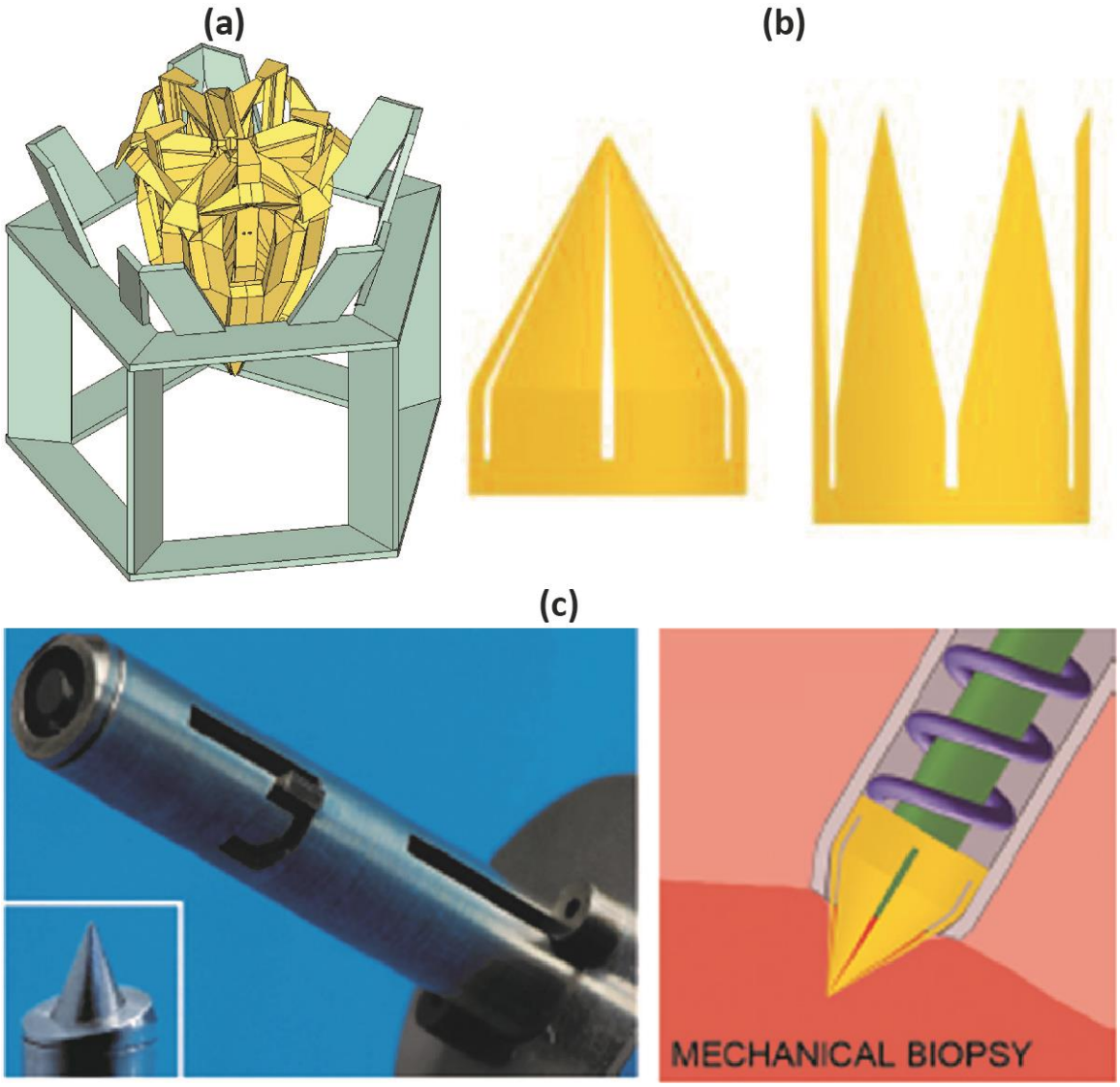

Figure 2.2: Bioinspired designs based on the Aristotle's lantern. (a) Isometric view of a drawing for a bionic model of the Aristotle's lantern, which has 3D printed plastic parts connected by rubber bands (not shown) for the attached musculature [21]. (b, c) The Aristotle's lantern served as a biological inspiration for a biopsy harvester [18].

Bioinspiration begins with observation of interesting natural phenomena, such as the efficient chewing motion of the Aristotle's lantern in sea urchins. This natural structure initially captivated Aristotle because it reminded him of a horn lantern with the panes of horn left out. More than two millennia later, Scarpa was fascinated by the complexity of the Aristotle's lantern that he and later Trogu mimicked the natural chewing motion using only paper and rubber bands (Figure 2.2a) [21, 22]. Similarly, Jelinek was bioinspired by the chewing motion of the Aristotle's lantern and developed a better biopsy harvester that could safely isolate tumorous tissue without spreading cancerous cells (Figure 2.2b, c) [17, 18]. In this case, bioinspired design was utilized to make a biomedical device that fit a specific need for a desired application.

The design protocol described here applies to a sediment sampler bioinspired by sea urchins. Through biological materials science, the natural structure of the Aristotle's lantern is characterized. Bioinspired design identifies potential applications where the natural mechanisms can be enhanced through the use of modern materials and fabrication techniques. The final design is re-examined through the prism of bioexploration to understand how the natural tooth structure evolved (Figure 2.3). The last bioexploration step, proposed by Porter [2, 23], uses engineering analysis methods to explore and explain biological phenomena.

All the important steps of the bioinspiration process are presented as an example for harnessing technology, pre-approved by nature, which can be used for solving modern problems. Our protocol, motivated by previous bioinspiration procedures presented for specific applications by Arzt [12], is targeted for biologists, engineers and anyone else who is inspired by nature.

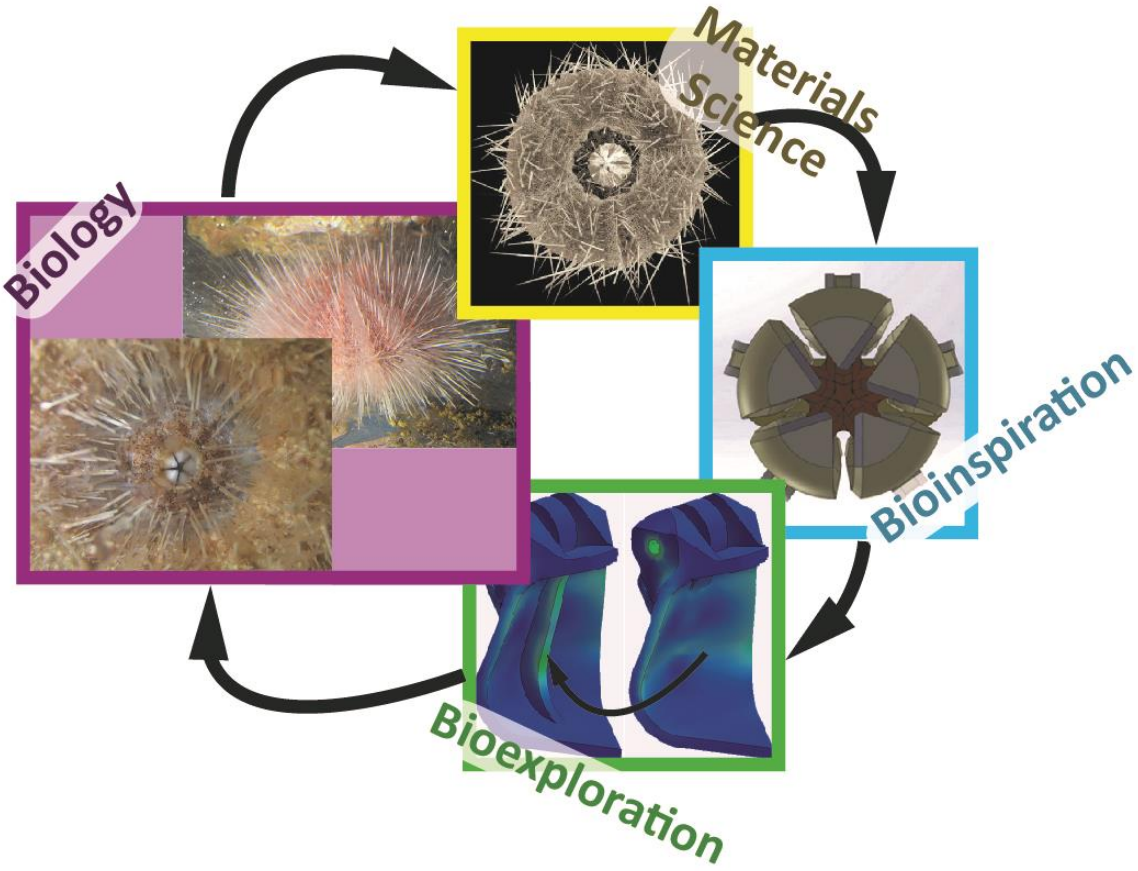

Figure 2.3: Four steps of the bioinspiration process. (clockwise from left) The bioinspiration process begins with learning from nature through observation of the pink sea urchin and the Aristotle's lantern. (top) Analysis of the sea urchin and the Aristotle's lantern structure from μ-CT scans (left). (right) Collected results are used to generate a bioinspired design prototype. (bottom) Engineering analysis methods were applied to explore biological phenomena and the bioinspired design [2, 23].

2.2 Biological Materials Science Protocol

1) Wear personal protective equipment (i.e., gloves, safety glasses and lab coat) and follow all applicable safety procedures for using dissecting tools.

2) Rinse off the forceps and scalpel with deionized (DI) water to use for dissection.

3) Thaw a frozen pink sea urchin at room temperature for 1 hour. Place a thawed specimen in a glass dish with sufficient space to be able to maneuver the urchin and cutting tools. Turn the urchin upside down so that the teeth tips face up.

3.1) Cut away the connective tissue around the perimeter of the Aristotle's lantern with the scalpel and carefully lift out the lantern. Rinse the lantern off with running DI water. Discard unused urchin parts in a proper waste disposal container.

3.2) Turn the Aristotle's lantern over again so the tips of the teeth face down. Locate the plumula end of each tooth (opposite to the tip) facing up and use the forceps to carefully slide out individual teeth from the lantern.

4) Prepare epoxy to pot the teeth. Weigh 5 g of resin and add 1.15 g of hardener (e.g., 100 parts resin to 23 parts hardener by weight) in a shallow disposable plastic tray. Mix contents together slowly without forming bubbles. Note: Do not leave leftover mixed epoxy in a container with insufficient exposure to the atmosphere. The curing process is exothermic and can ignite nearby flammables. Keep any leftover mixed epoxy in a well-ventilated fume hood away from flammable items.

4.1) Lubricate a 2.5 dram plastic tube (22 mm inner diameter, 39 mm length) using petroleum jelly applied with a finger and wipe off any excess with a tissue. Fill up the tube halfway with mixed epoxy.

4.2) Use the forceps to pick up a tooth and carefully submerge it in the epoxy with the curved concave side facing up. Let the epoxy cure at room temperature for 24 hours. Note: Prevent the tooth tip from drifting to touch the plastic tube wall as the epoxy cures since this will make polishing the tip more difficult.

5) Place the plastic tube with cured epoxy in a vise. Tighten the vise slowly until a fissure is made in the plastic tube. Peel away residual plastic from the epoxy surface.

5.1) Use a sectioning saw to cut the epoxy around the tooth down to a smaller block (1 cm^3).

6) Prepare a clean area for polishing and set up a flat work station with a hard plastic board. Fill a squirt bottle with distilled water.

6.1) Start with the lowest grit sandpaper available (e.g., 120) and squeeze a small amount of water from the wash bottle onto the sandpaper. Using light pressure, rub the sample in one back and forth direction (e.g., left-right) for 5 minutes.

6.2) Wash off the surface of the sample over a sink and wipe off with a particle-free tissue. Remove any leftover sandpaper grit with compressed air for 15 s.

6.3) Use progressively higher grit sandpaper (e.g., 600 and 2400) to repeat protocol steps 6.1 and 6.2. Using light pressure, rub the sample in a back and forth direction perpendicular to the previous polish step (e.g., up-down, left-right). Note: Use a light microscope at 20x magnification to see perpendicular scratch marks intersect with each grit level (e.g., 120, 600, 2400). Move to the next higher grit sandpaper when scratch marks from the previous grit level disappears.

6.4) Prepare a squirt bottle with 3-μm diamond polishing suspension in a 1:1 DI water solution. Use a polish cloth for diamond suspensions to repeat protocol steps 6.1 and 6.2.

6.5) Prepare a squirt bottle with 0.5-μm alumina polishing suspension in a 1:1 DI water solution. Use a microcloth polishing surface to repeat protocol steps 6.1 and 6.2. Note: Fine scratch marks from protocol steps 6.4 and 6.5 will not be visible at 20x magnification. For these protocol steps, polish for 5 minutes in a circular motion to remove all previous scratches.

6.6) Clean the polished surface with DI water and use particle-free tissue with compressed air to carefully dry. Wrap with particle-free tissue to maintain mirror polished finish. Note:

Dry all polishing surfaces face down on large particle-free tissues. Store in a plastic sleeve to avoid dust particles settling on the surface between polishing times.

7) Characterize the sea urchin tooth microstructure using scanning electron microscopy (SEM). Use a sputter coater to sputter iridium with a deposition current of 85 mA for 10 s onto the polished tooth surface for a coating thickness of ≈ 20 nm.

7.1) Obtain micrograph images at 250x – 4000x magnification using a SEM. Note: Use 5 kV in the scanning electron (SE) mode and 15 kV in the back-scattered electron (BSE) mode. Use BSE mode to identify calcite fibers interspersed with Mg-enriched polycrystalline matrix.

8) Perform micro-computed tomography (μ-CT) scans of a whole pink sea urchin and a freshly dissected Aristotle's lantern. Position each thawed sample inside the closed chamber container with a moistened tissue to provide a humidified environment while scanning.

8.1) Scan the whole urchin and the Aristotle's lantern by μ-CT with an isotropic voxel size of 36.00 μm and 9.06 μm, respectively. Apply an electrical potential of 100 kVp and 70 kVp with current of 100 mA and 141 mA, for the whole urchin and the Aristotle's lantern, respectively, using a 1.0 mm aluminum filter for both.

8.2) Apply a beam hardening correction algorithm during image reconstruction to account for beam hardening artifacts that result from the μ-CT x-ray source emitting x-rays of multiple energies using manufacturer's protocol.

9) Use imaging software to refine image segmentation and acquire a triangle mesh model for the Aristotle's lantern structure.

9.1) Load and preview Aristotle's lantern image data from the μ-CT scan. Match the voxel size (9.06 μm) to the values from the micro-CT scan.

9.2) Use a volume rendering function to visualize the Aristotle's lantern in 3D space. Adjust the 2D orthogonal slice with the Bounding Box module and adjust the threshold value/color with the Volume Rendering module.

9.3) Make mask segments for the region of interest (e.g., sea urchin tooth) using the segmentation editor. Select XY, YZ, and XZ planes and the 3D isometric view. Use the magic wand (black arrow) to distinguish between simple structures (tooth vs. pyramid) in the Aristotle's lantern.

9.4) Reconstruct the model surface from the extracted mask segments. Select the Surface Generation module and apply. Deselect the Volume Rendering Settings to have the visible top surface disappear. Add the Surface View module to display the surface result.

9.5) Simplify the model surface by reducing the number of faces to < 18,000.

9.6) Edit individual triangle mesh on the model surface as needed. Save the model as a stereolithography (STL) file for exporting to use with computer-assisted design (CAD) modeling software.

2.3 Bioinspired Design Protocol

1) Use the Aristotle's lantern from the micro-CT scan as a reference to make a bioinspired design with CAD modeling software. Note: The bioinspired design has five curved teeth with height 6 cm and diameter 8 cm for the closed lantern. It is scaled up ≈ 5x from the size of the natural Aristotle's lantern.

2) Save the STL file parts to a flash drive and upload the files to a fused deposition modeling (FDM) 3D printer.

2.1) Load acrylonitrile butadiene styrene (ABS) plastic material cartridge into the appropriate slot on the front of the 3D printer.

2.2) Insert the modeling base on the Z platform and align tabs with slots on the metal tray.

2.3) Slide the modeling base back until the front handle edge is flush with the front tray edge and secure the base with retainers.

2.4) Open each of the STL file parts and follow the display screen steps to print all the lantern parts at the same time. Note: Lantern parts must fit within the building envelope (25 x 25 x 30 cm) for the 3D printer. All five teeth are arranged on the modeling base and printed simultaneously with the tooth tip facing up. The build rate is 16 cm^3 per hour and the total build time is approximately 8 hours.

2.5) Release the modeling base retainers when all file parts are printed and slide the base out of the 3D printer along the tray guides.

2.6) Flex the ends of the modeling base with attached parts back and forth (e.g., front-right to back-left) until the parts loosen from the base.

2.7) Use a metal spatula to pry all parts off the base and a metal file to wear down any extra plastic attached to the parts.

3) Fasten each tooth to a joint arm with a link rod and two E-retaining rings on either side. Note: Refer to (Figure 2.6) for assembly of the bioinspired Aristotle's lantern.

2.4 Bioexploration Protocol

1) Use the CAD file for the bioinspired tooth to do a finite element modeling (FEM) stress analysis test.

1.1) Open the file (xx.sldprt) to do further engineering analysis. Above the "Office Products" tab, select the "SolidWorks Simulation" button.

1.2) Above the “Simulation” tab, select the “Study Advisor” button and then the drop-down option “New Study”.

1.3) Select the type of simulation test to be run by choosing “Static”.

1.4) On the Static Test list, right-click on “Fixtures” and select “Fixed Geometry”.

1.5) Click on the inner faces to add fixtures to the mounting holes where pins will go.

1.6) On the Static Test list, right-click on “External Loads” and select “Force”.

1.7) Click on the tooth grinding tip faces to apply 45 N force to the edges.

1.8) On the Static Test list, right-click on “External Loads” and select “Gravity”.

1.9) Indicate “Top Plane” for the gravity force applied normal to the plane.

1.10) On the Static Test list, right-click on “Mesh” and select “Create Mesh”.

1.11) Move the scale bar for “Mesh Density” all the way to the right for “Fine”.

1.12) On the Static Test list, right-click on “Static” and select “Run” to run the test. Note: The colored scale bar for areas of highest stress and the “Yield Strength”.

2) Compare stress analysis test results for the bioinspired tooth with and without the keel.

2.5 Representative Results

Bioinspired design of the Aristotle’s lantern sampling device depends heavily upon the quality of the characterization methods used. Non-invasive techniques like µ-CT are helpful for analyzing the whole lantern and individual teeth to apply application specific enhancements for the bioinspired design (Figure 2.4). Meanwhile, the tooth microstructure can be explored via secondary electron and back-scattered electron micrographs of the polished cross-section of an individual tooth (Figure 2.5). The darker gray region is the harder stone part of the tooth grinding tip and consists of up to 40 mol % magnesium atoms that replace the calcium atoms.

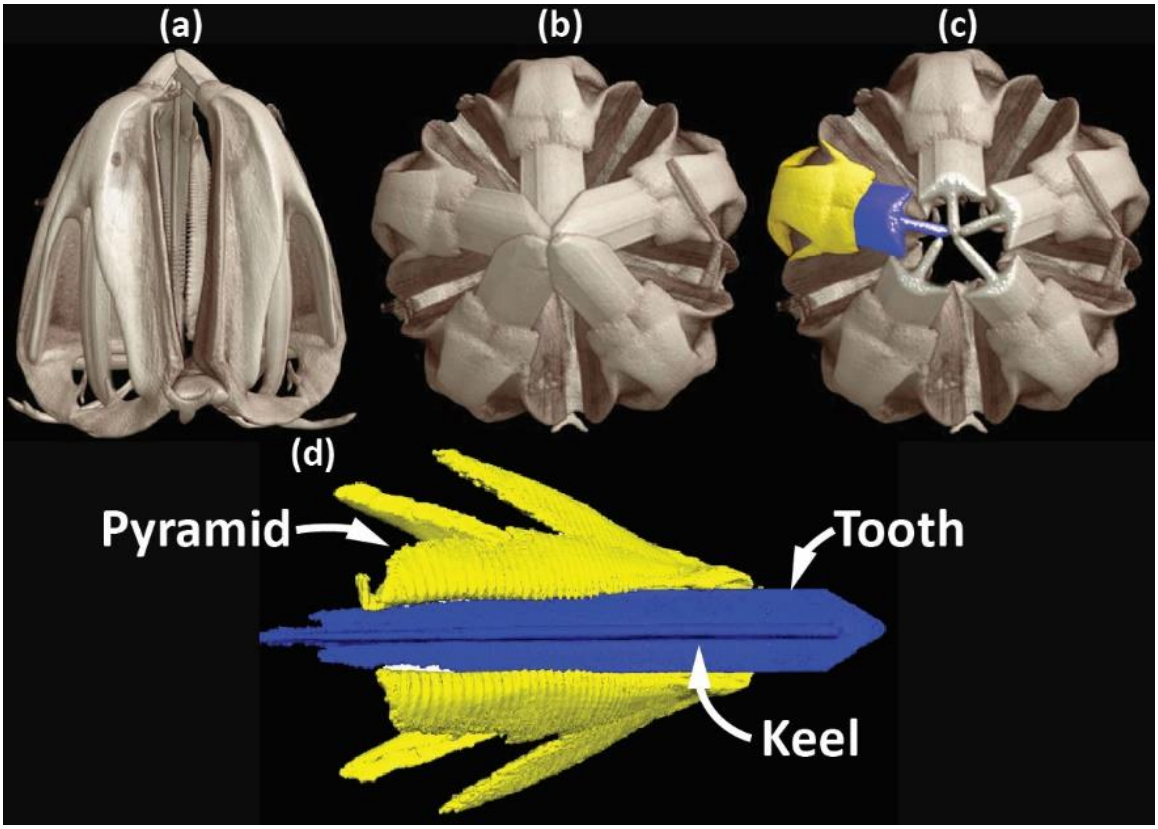

Figure 2.4: Micro-computed tomography analysis of the Aristotle's lantern structure. (a) Side view of the pyramid structures that help to support the teeth. (b) Sea urchin teeth stack on top of each other and exhibit five-fold symmetry. (c) Distal tip portions are removed to show the longitudinally attached keel structures for all five teeth. (d) An individual tooth and keel (blue) with corresponding pyramid (yellow) are shown and also indicated in (c).

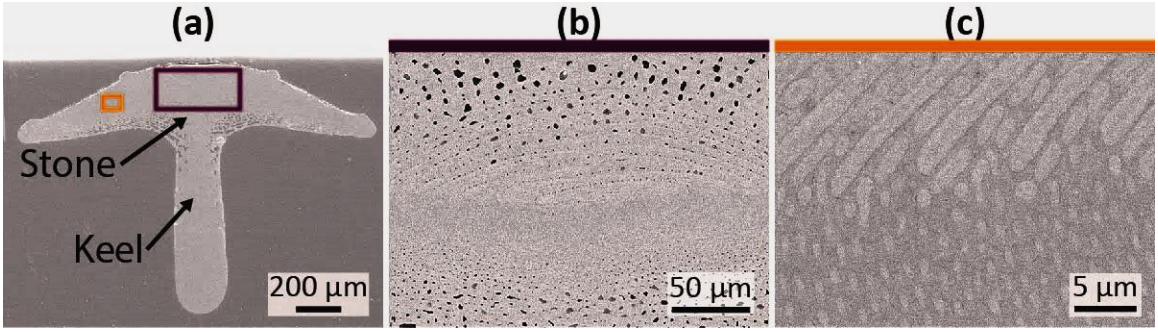

Figure 2.5: Scanning electron microscopy (SEM) analysis of the sea urchin tooth microstructure. (a) SEM micrograph of a polished tooth cross-section with the faint stone stripe region and keel (bottom) indicated. (b, c) Backscattered electron SEM micrographs of the purple and orange boxes from (a) show curved plate and round fiber calcite primary elements situated above a denser Mg-enriched polycrystalline matrix (darker gray).

Analysis of the tooth microstructure with BSE-SEM (Figure 2.5) confirmed the structural importance of the Mg-enriched stone part in the tooth grinding tip. Plate and fiber

primary elements (calcite monocrystals, lighter gray in Figure 2.5c) are connected together by a matrix of secondary elements (calcite and magnesium carbonate polycrystals, darker gray in Figure 2.5c), that make up the hardest stone region of the tooth grinding tip.

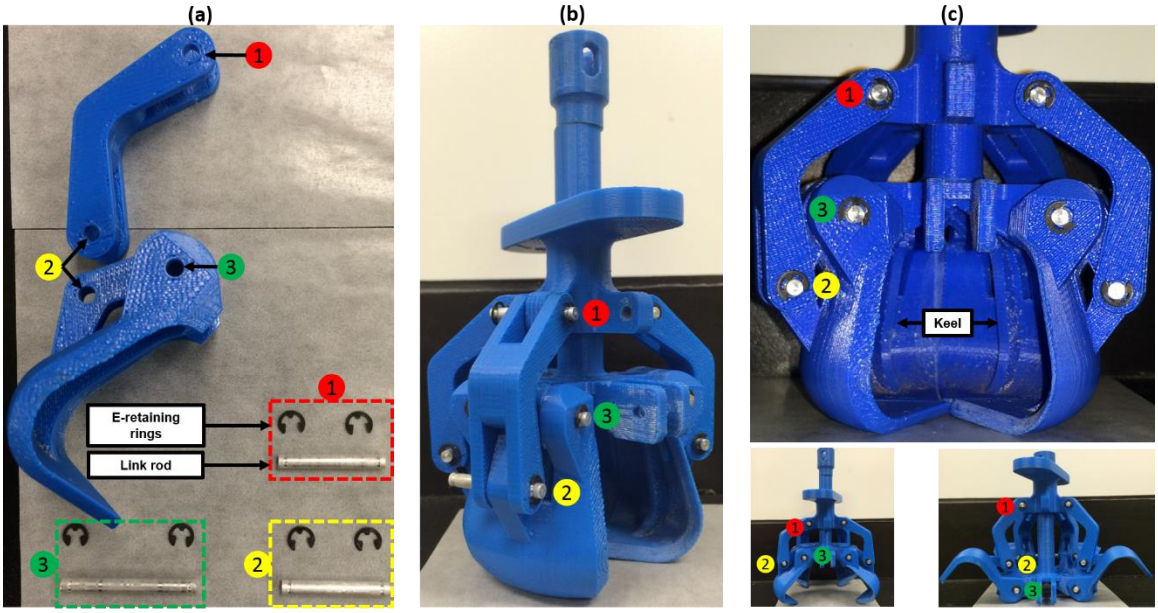

Figure 2.6: Assembled 3D printed bioinspired Aristotle's lantern parts. (a) E-retaining rings and link rods are used to fasten the 3D printed tooth parts at three joint positions. (b) Assembled bioinspired Aristotle's lantern with one tooth removed. (c) View of the keel for individual teeth and the changing joint positions when the lantern is partially (left) and fully open (right).

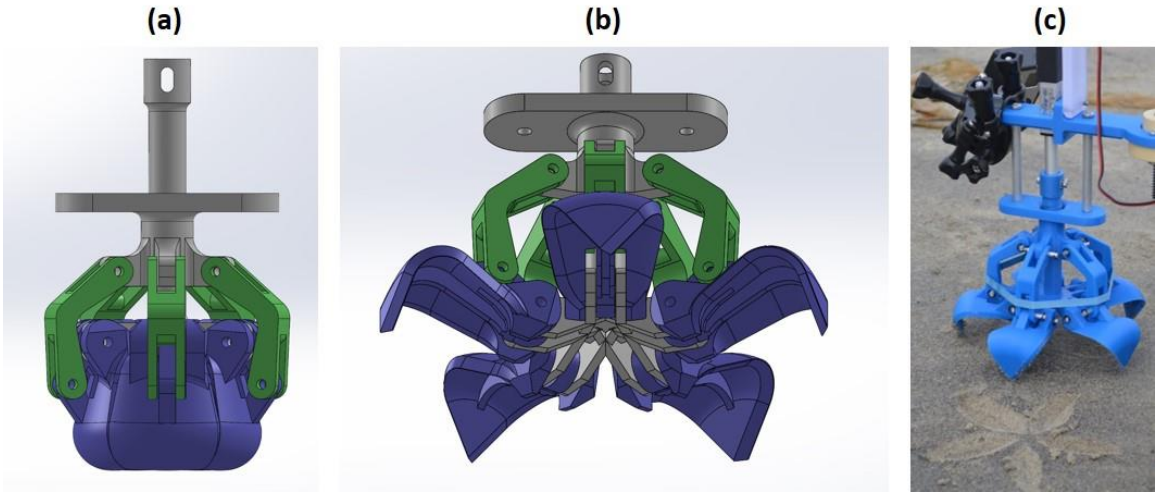

Figure 2.7: Bioinspired Aristotle's lantern design and usage at the beach. (a, b) Computer aided design images of the bioinspired Aristotle's lantern while closed and fully open, respectively. (c) The 3D printed bioinspired Aristotle's lantern collected different types of sand on the beach.

The bioinspired lantern was designed with CAD software, 3D printed and assembled (Figure 2.6) for collection of sand at the beach (Figure 2.7). Stress analysis tests were used to calculate the von Mises stress of two tooth designs, one without the keel (Figure 2.8a) and the other with the keel (Figure 2.8b). A solid mesh composed of tetrahedrons was employed over the geometry of the tooth. The force value chosen (45 N) matched measurements from tests at the beach to penetrate 1 cm deep into hard sand with lantern teeth perpendicular to the surface.

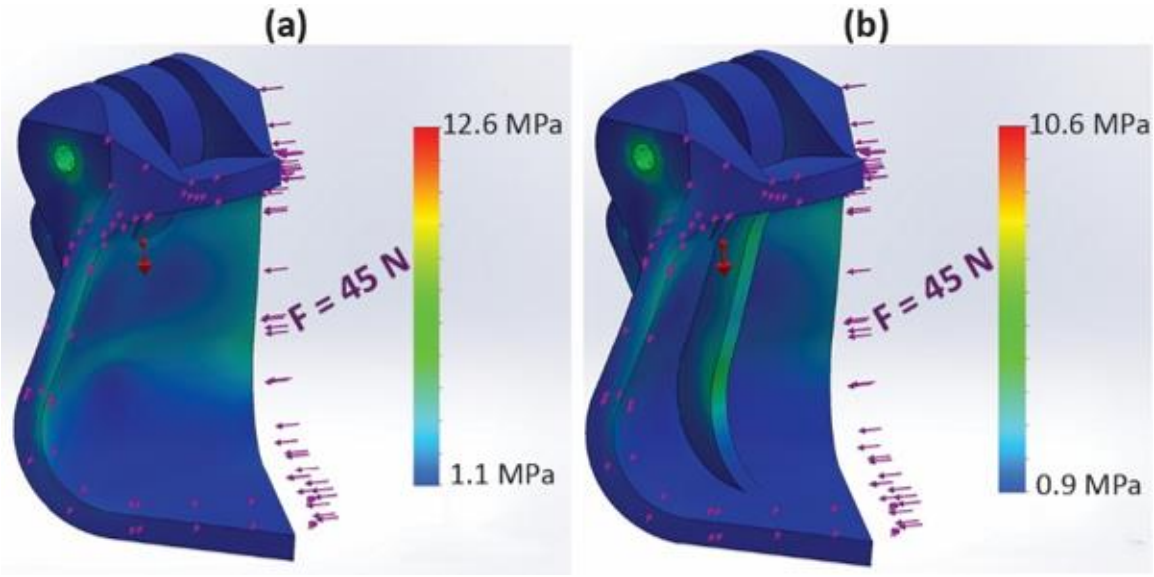

Figure 2.8: Bioinspired sea urchin tooth stress analysis test. (a, b) Finite element analysis shows the non-keeled (a) versus keeled (b) tooth when force is applied at the tooth edges. The keeled tooth design experienced ≈ 16% less stress due to addition of the keel.

The mass of the keeled tooth design (12.72 g) was compared with that of the non-keeled tooth design (12.26 g) to find a ≈ 4% increase for the added keel. For 45 N applied force, the maximum stress experienced by the keeled tooth design (10.6 MPa) versus the non-keeled tooth design (12.6 MPa) was ≈ 16% less for the keeled tooth (Figure 2.8a, b). The mass increase is small compared with the decrease in stress that the keel provides. The

decrease in stress demonstrates the effectiveness of this bioinspired design for concentration of stress within the keeled region.

2.6 Discussion

Sea urchins use the Aristotle's lantern (Figure 2.1a) for a variety of functions (feeding, boring, pivoting, etc.). The fossil record indicates that the lantern has evolved in shape and function from the most primitive cidaroid type to the camarodont type of modern sea urchins [19]. Cidaroid lanterns have longitudinally grooved teeth (Figure 2.1b, top) and non-separated muscle attachment to its pyramid structure. This limits their up and down movement and robs them of the greater scraping power generated by lateral movement, which is observed in the more modern camarodont lanterns (Figure 2.1b, bottom). Biologists have speculated that the keeled tooth (Figure 2.1c, d) evolved in camarodonts to reinforce the tooth under the strong tensile forces generated by scraping hard substrates [2, 20, 24].

The bioinspired design protocol in this work combined biology, biological materials science, bioinspired design and bioexploration (Figure 2.3) to develop a bioinspired device with a specific function for sampling sediment. The μ-CT scan of the Aristotle's lantern (Figure 2.4) was imported as an STL file for reference only since the final sampler design did not mimic the complex muscle attachment in the natural structure. Instead the bioinspired design employed a simpler opening and closing mechanism with parts that could be manufactured easily by a 3D printer for assembly into the Aristotle's lantern sampler. Overall, we used a circular approach for bioinspired design since the bioexploration step allowed for new conclusions to be drawn from the natural biology. Potential modifications of the bioinspired design can address different applications besides

sampling sediment. A limitation of this protocol is that it is focused on one specific application of the bioinspired process for a device based on the Aristotle's lantern. However, the protocol outlined here can be applied to the analysis, development and ultimate fabrication of other bioinspired designs based upon biological samples.

The primary application for this assembled bioinspired Aristotle's lantern sampler (Figure 2.6) was for collecting loose and compacted sand (Figure 2.7). Looking ahead, NASA has a plan to bring back Martian samples to Earth using a sample-return rover after a succession of missions over many years [25]. A sample-return rover outfitted with a bioinspired Aristotle's lantern sampler may be beneficial to future missions. A smaller sampler that resembles the size of a natural Aristotle's lantern may also be useful for other applications. The anisotropy of hardness in natural urchin teeth, while interesting in its own right, was not incorporated in this bioinspired design.

Bioexploration of keeled versus non-keeled teeth confirmed the important structural purpose of the keel in natural sea urchins (Figure 2.8). The bioexploration result provides data that helps explain why modern sea urchins evolved keel structures. We acknowledge that Porter [2, 23] was the first to propose the bioexploration step applied in this work, which was essential for using engineering analysis methods to quantify the mechanical advantage of the keel structure in the sea urchin tooth. Future bioinspired design that connects natural observation, biological materials science, bioinspired design and bioexploration can be beneficial for incorporating a deeper rooted familiarity with natural design principles.

2.7 Conclusions and Future Applications

The Aristotle's lantern bioinspired sediment sampler went through three design iterations and each one mimicked the natural structure less than the preceding version. This indicates that a careful balance must be struck between mimicry (of nature) and utility (for mankind) when charting a bioinspired design path. Nature can provide a general template, but it would be unreasonable to expect a complete solution for human derived problems. For this application, the jaws needed to open wider and the teeth needed to have more curvature to increase the volume of sediment sampled. A slider-crank mechanism was responsible for opening and closing the jaws. Significantly less reaction force was localized at point *A* when the crank angle (α) range of motion was kept above ≈ 30° (Figure 2.9). Joint arm (*AB*) redesign from straight to bent and link rod attachment (*A*) reposition to further down the tooth exterior (Figure 2.6) enabled excellent device performance. The actual musculature that opens and closes Aristotle's lantern did not need to be mimicked.

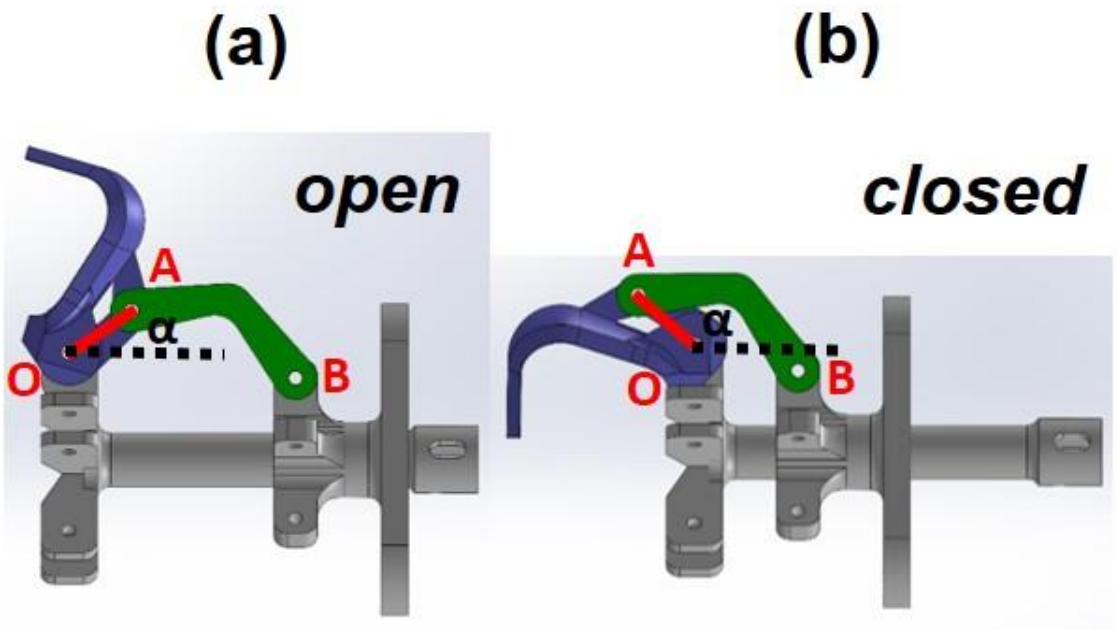

Figure 2.9: Final design for the bioinspired sediment sampler. The open (a) and closed (b) positions are activated by a slider-crank mechanism when pushing down or pulling up on the plunger end, respectively.

An iterative design process that resulted in a functional bioinspired device would typically be the end of the story. However, inclusion of an additional bioexploration step [2, 23] that used engineering analysis methods to explore and explain biological phenomena provided an avenue for connection back to the natural structure (Figure 2.3). Evolutionary biologists have speculated that a keeled tooth (Figure 2.1b) developed to withstand increased grinding force from enhanced Aristotle's lantern functionality due to complex movements enabled by more advanced musculature. Finite element analysis confirmed that stress concentrated primarily in the keel and that less stress was experienced overall by a keeled versus non-keeled tooth (Figure 2.8). Experimental evidence confirmed by sea urchin tooth biology can be useful for the design of future sediment sampler devices.

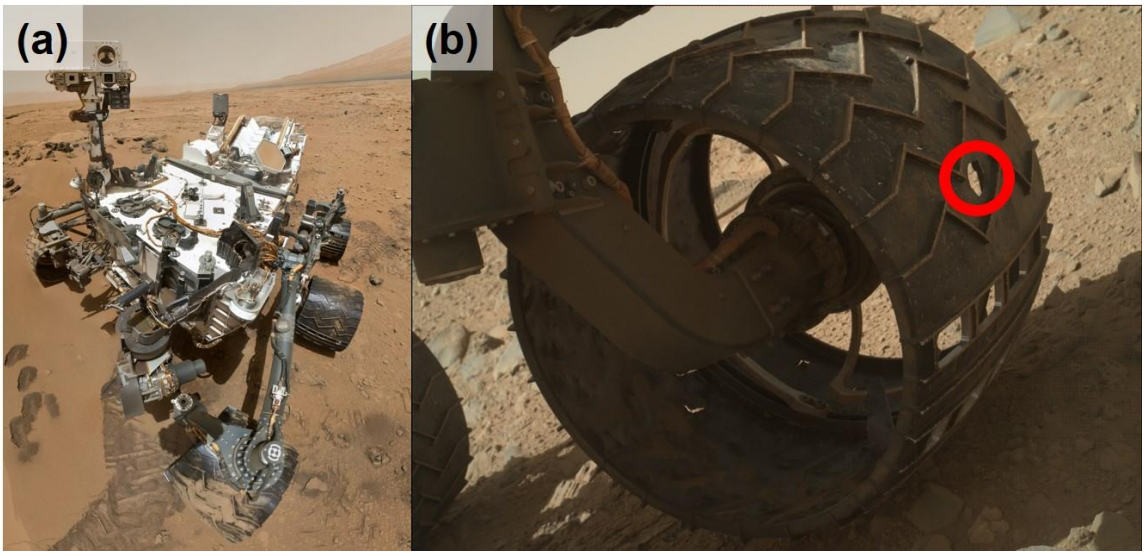

Figure 2.10: Mars rover Curiosity (a) and the puncture (within red circle) on one of its aluminum wheels (b). Wheel cutouts below the puncture imprint 'JPL' in Morse code as the wheels traverse the surface of Mars. Images taken from [26].

Planetary surface exploration applications for this bioinspired sediment sampler, as well as further modifications made to its design, can be guided by observations of what has and has not worked well for the Mars rover Curiosity (Figure 2.10a). The overall mission

was to analyze sediment from various locations with its advanced instrumentation, however, front wheel damage incurred early on by Curiosity has altered or delayed the stated objectives (Figure 2.10b). Future planetary surveys can be more expansive by using smaller, specialized rovers that traverse rough terrain to collect and return samples to the main rover for further analysis. This concept would fit well with the stated mission in 2020 for the rover to collect and store samples in a cache that can be analyzed by astronauts on Mars or sent back to Earth via another rover that fetches from the main rover (Figure 2.11a). The Mars 2020 rover will have new capabilities for conducting sediment analysis (Figure 2.11b), but planetary surface coverage may once more depend on limitations to its mobility.

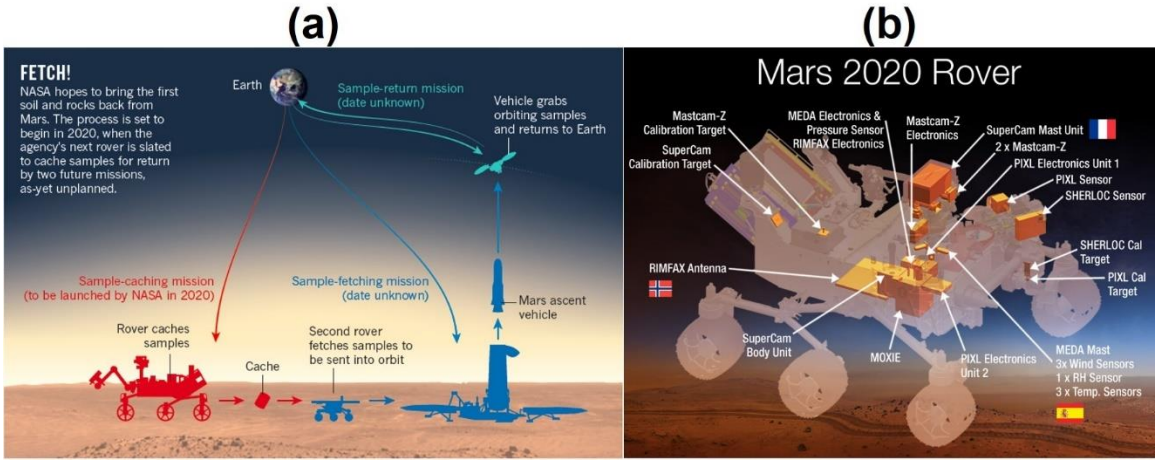

Figure 2.11: The next Mars rover mission in 2020 will be to collect and eventually return sediment samples (a). Many advanced instruments will be installed on the new rover. Images taken from [25, 27].

Following publication in the Journal of Visualized Experiments (JoVE) [28], representatives from the Pacific International Space Center for Exploration Systems (PISCES) in Hilo, HI reached out to learn more about this bioinspired sediment sampler. The Additive Construction with Mobile Emplacement (ACME) project [29] is a collaborative effort between PISCES, NASA Kennedy Space Center (KSC) and Honeybee Robotics to develop technology to build structures on planetary surfaces using in-situ

resources, which includes a rover for building a Vertical Takeoff / Vertical Landing (VTVL) Pad. PISCES mentioned that a small sediment sampler rover tethered to a main rover could explore Mars lava tubes and collect otherwise inaccessible specimens protected from ultraviolet radiation and extreme temperatures on the planetary surface. Previously, researchers have speculated this type of sheltered environment might provide sufficient minerals and nutrients for chemosynthetic organisms, similar to those found near volcanic vents on Earth [30], such that constant temperatures could be maintained by internal heat to permit liquid water to persist [31].

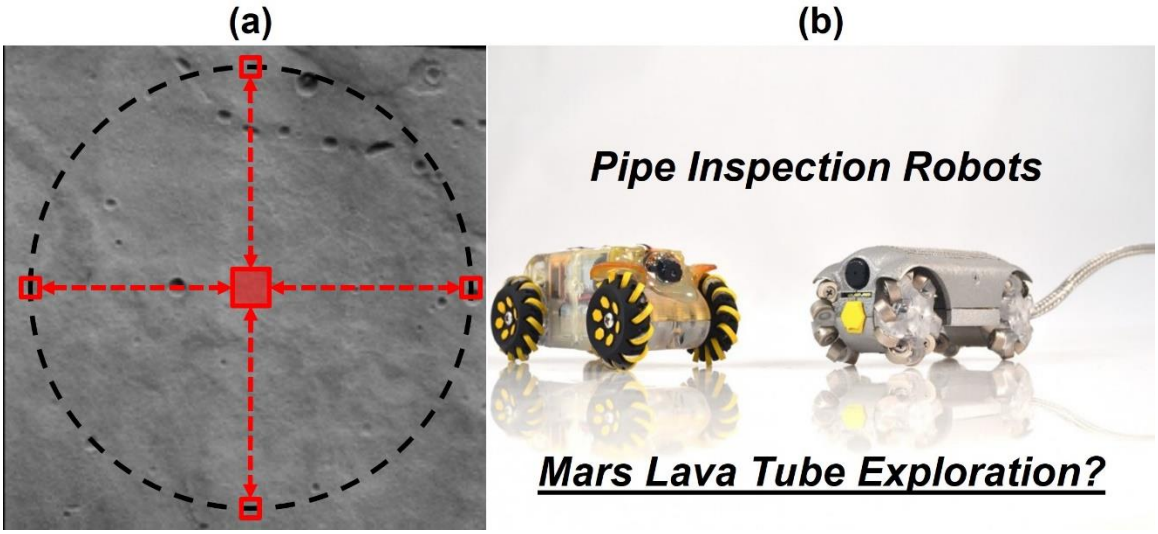

Figure 2.12: Potential strategy for small rovers (unfilled red boxes) to collect sediment samples from the surface of Mars (a) and return to the main rover (filled red box) for analysis [31]. Robust and compact natural gas pipe inspection rovers (b), which are freestanding or tethered to the main rover, may be modified with an attached sampler device for Mars lava tube exploration [32]. Images adapted from [31, 32].

A combination of several ideas discussed may be beneficial for future Mars exploration missions. An Aristotle's lantern bioinspired sediment sampler with keeled tooth design can efficiently collect samples. Small, rugged sample collecting rovers can cover much more planetary surface and be tethered to a main rover for Mars lava tube exploration (Figure 2.12a). Honeybee Robotics has already developed small, rugged robots

for natural gas pipe inspection (Figure 2.12b), so a similar style device might be outfitted with a bioinspired sediment sampler for the ACME project in collaboration with NASA KSC and PISCES.

Figure 2.13: The Aristotle's lantern bioinspired sediment sampler, also known as the "Mars Urchin" (a), was profiled on the science, technology, engineering and math (STEM) series for kids called "Xploration Station: Nature Knows Best" (b).

Further collaboration on the rover design may come from unexpected sources through additional media exposure. A science, technology, engineering and math (STEM) series for kids called "Xploration Station: Nature Knows Best" (Figure 2.13a) profiled the Aristotle's lantern bioinspired sediment sampler, also known as the "Mars Urchin" (Figure 2.13b), to "showcase the fun and clever ways scientists, engineers, and innovators are copying plants, animals and more to create some of the world's most amazing advancements" [33]. The show's host, Danni Washington, made the connection that a potential need for the Mars Urchin to traverse the Martian planetary surface might be met with a solution in the form of an innovative all-terrain wheel design derived by a startup called Shark Wheel (Figure 2.14 a, b). Previous attempts by Shark Wheel to connect with rover scientists at NASA had been unsuccessful, so perhaps an alternative path facilitated

through connection with the Mars Urchin can provide the impetus for collaboration on a novel wheel design for lightweight sinusoidal aluminum wheels that can enhance future Mars rovers.

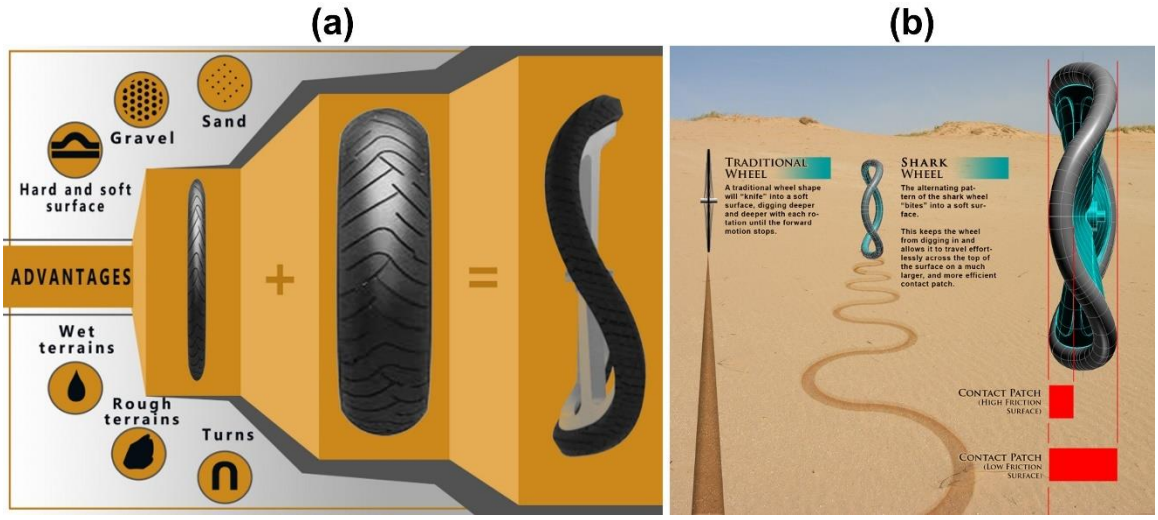

Figure 2.14: The Shark Wheel (a) can address problems with traditional wheel design in four unique ways. First, instead of hitting small obstacles directly, the wheel can push them right and left as it rolls to make for a smoother ride over rough terrain. Second, there is less friction due to less rolling resistance, so the rover can presumably move around with less energy consumed. Third, the wheel can last 20% longer due to multiple center points that result in more even wear. Fourth, the wheel lip shape makes for a "catch-release" mechanism that resembles an antilock brake for a car, so that the rover wheels can spin as they slide for greater slide control. Images taken from [34].

Chapter 2, in part, is published as "A Protocol for Bioinspired Design: A Ground Sampler Based on Sea Urchin Jaws" Journal of Visualized Experiments, vol. 110, e53554, 2016. This work was coauthored by S.E. Naleway, T.S. Wirth, J-Y. Jung, C.L. Cheung, F.B. Loera, S. Medina, K.N. Sato, J.R.A. Taylor and J.M. McKittrick. The dissertation author is the first and corresponding author of this work.

CHAPTER 3: SPONGY BONE BIOINSPIRED POROUS CERAMIC SCAFFOLDS

3.1 Freeze Casting Background

Ice templating, often called freeze casting, refers to a physical process whereby a typically aqueous slurry of ceramic particles, dissolved polymer and dispersant are templated into lamellae between directionally growing ice crystals (Figure 3.1). Most particles get segregated into lamellae between the ice, but some get engulfed depending on the speed of the solid growing ice front through the liquid medium.

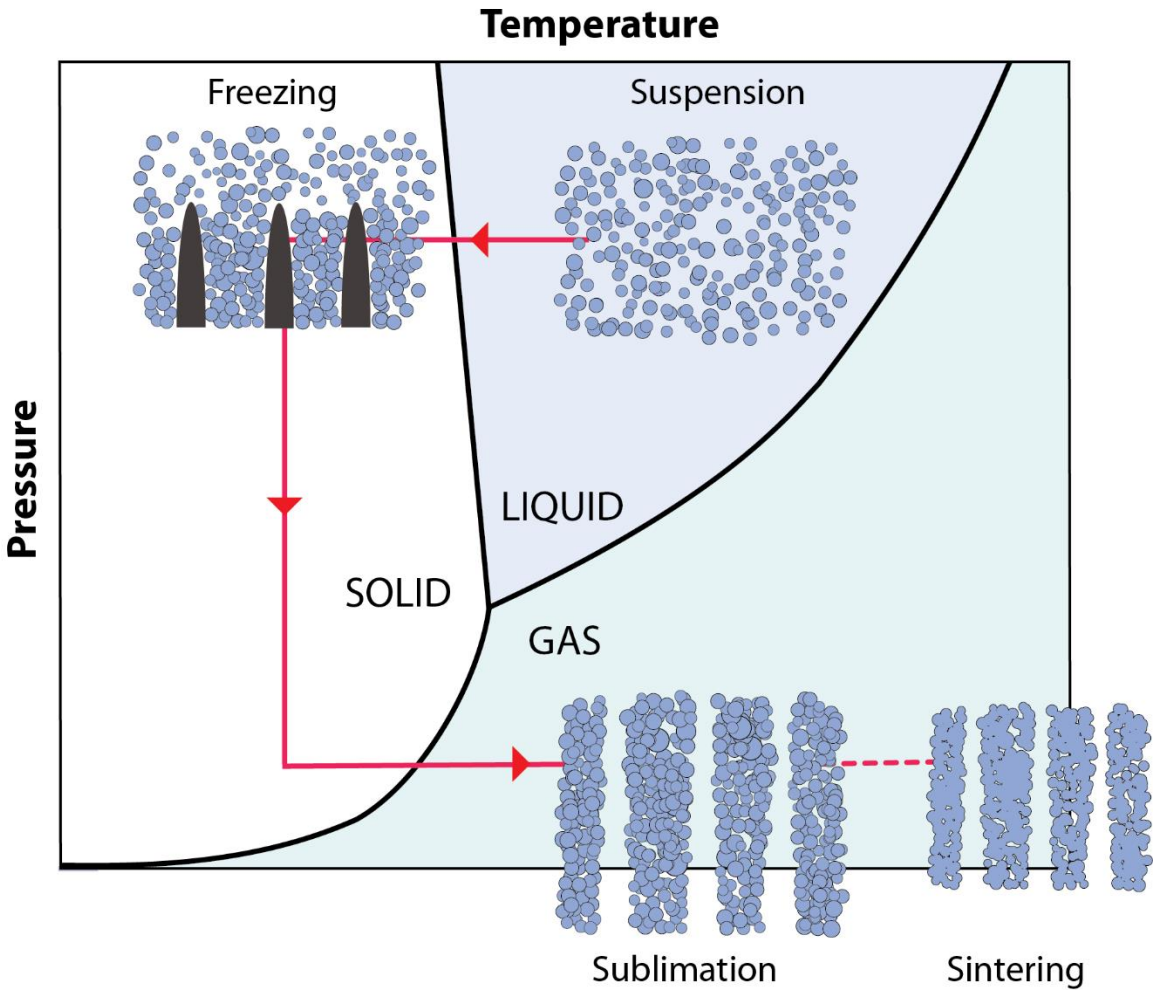

Figure 3.1: Schematic representation of ice-templating principles. The process is used to prepare macroporous materials, where the porosity is templated by ice crystals grown during freezing. After freezing, the ice crystals are sublimated, to leave behind imprints of concentrated particles that are sintered [35].

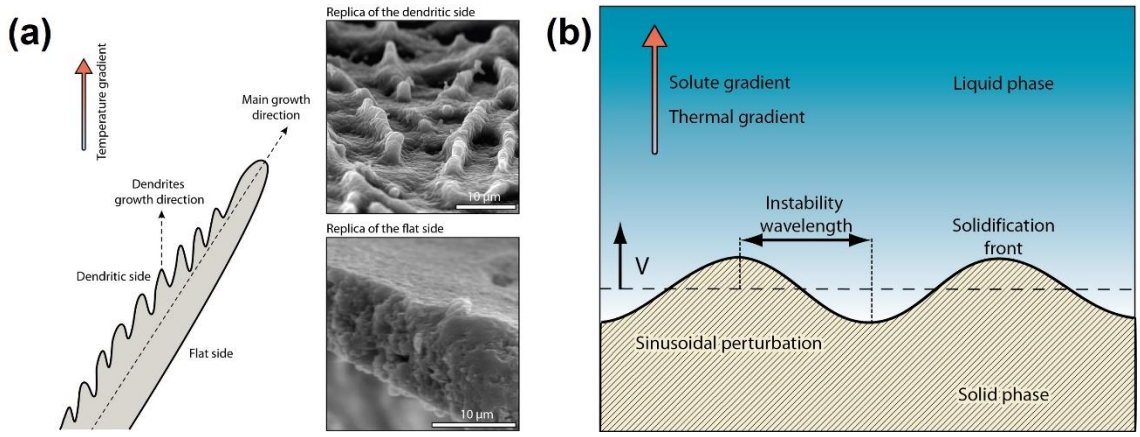

Figure 3.2: (a) Schematic representation of a dendritic ice crystal growing in a temperature gradient, and micrographs showing a replica of crystal morphology in ice-templated structures. The replica of the dendritic crystals (when grown in a particle suspension) has numerous dendritic surface features. This phenomenon is encountered in materials processing routes called ice-templating or freeze-casting. (b) Schematic of a Mullins-Sekerka instability with planar freeze front destabilized by a sinusoidal perturbation [35].

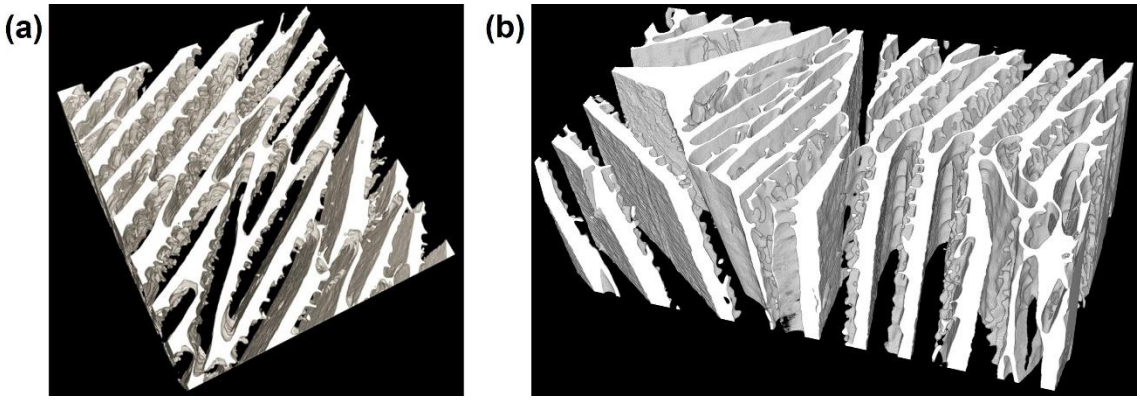

Figure 3.3: (a) Typical three-dimensional reconstruction of ice-templated alumina obtained by X-ray tomography. The ceramic here is alumina. (b) Three-dimensional representation of the typical structure of a porous ice-templated material. The image was obtained by X-ray computed tomography. The pores are aligned along the freezing direction (direction of the temperature gradient, vertical in this case). Dendritic surface features that originate from the dendritic growth of the ice crystals cover the walls. The typical wall thickness is in the 10-50 microns range [35].

Dendritic ice crystal growth driven mostly by Mullins-Sekerka instabilities (Figure 3.2) makes a frozen block that gets lyophilized into a "green body" of particles held loosely together by the polymer that was dissolved within the initial slurry. The last sintering step fuses particles together as polymer burns out to produce a porous scaffold (Figure 3.3).

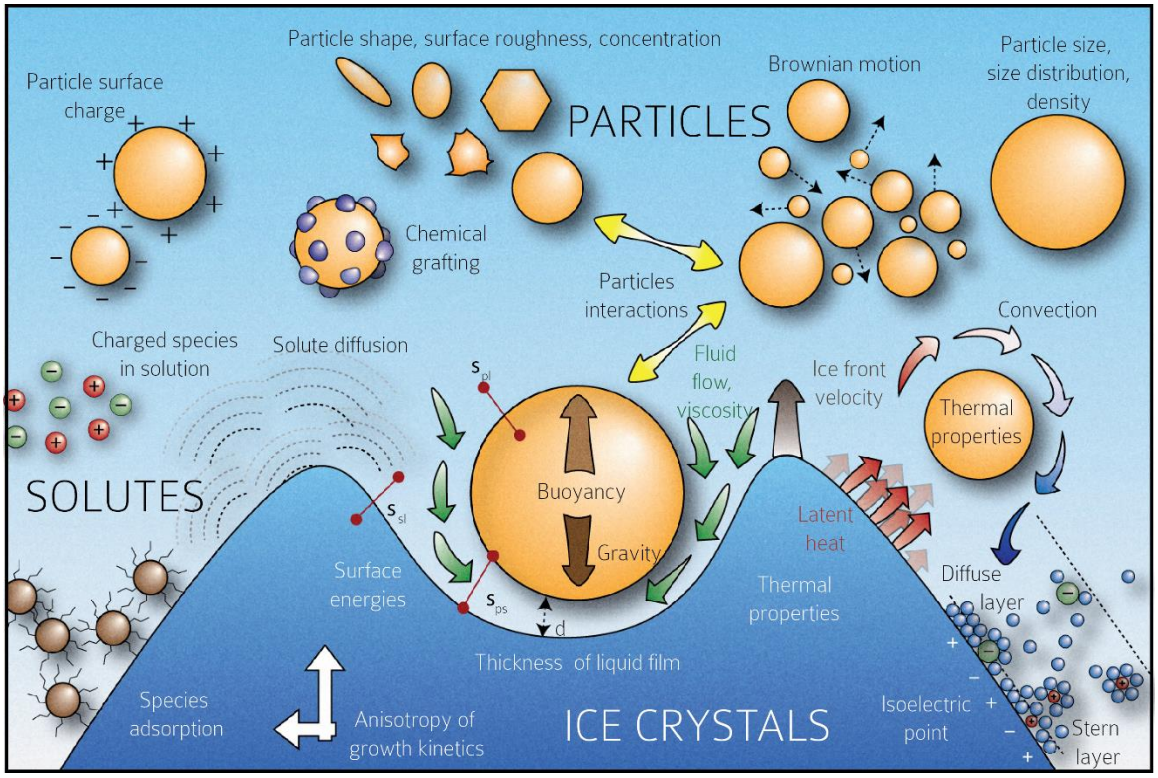

Figure 3.4: An all-inclusive schematic that shows the multitude of interactions that can occur at the interface between a growing ice crystal and a particle. These all constitute intrinsic methods of control over the freeze casting process [35]. Schematic representation of the interactions between a solidification front and objects such as particles. The scheme shows most of the phenomena and parameters that takes place when objects such as particles interact with a solidification front. This is useful in particular in materials science process called ice-templating or freeze-casting.

Many intrinsic methods of control over the freeze casting process are driven by modifiable aspects of the slurry itself that include various particle (size, morphology, surface charge, etc.) and solution factors (liquid viscosity, additives, freezing agents, other solutes, etc.), as shown in Figure 3.4. In fact, the overall freeze casting process can be further complicated by the presence of extrinsic methods of control such as inclusion of external templates, and applied electrical, magnetic or thermal gradients (Figure 3.5). Both

intrinsic and extrinsic methods can be used to guide the freeze casting process to make porous scaffolds with features that resemble the porosity observed in spongy bone.

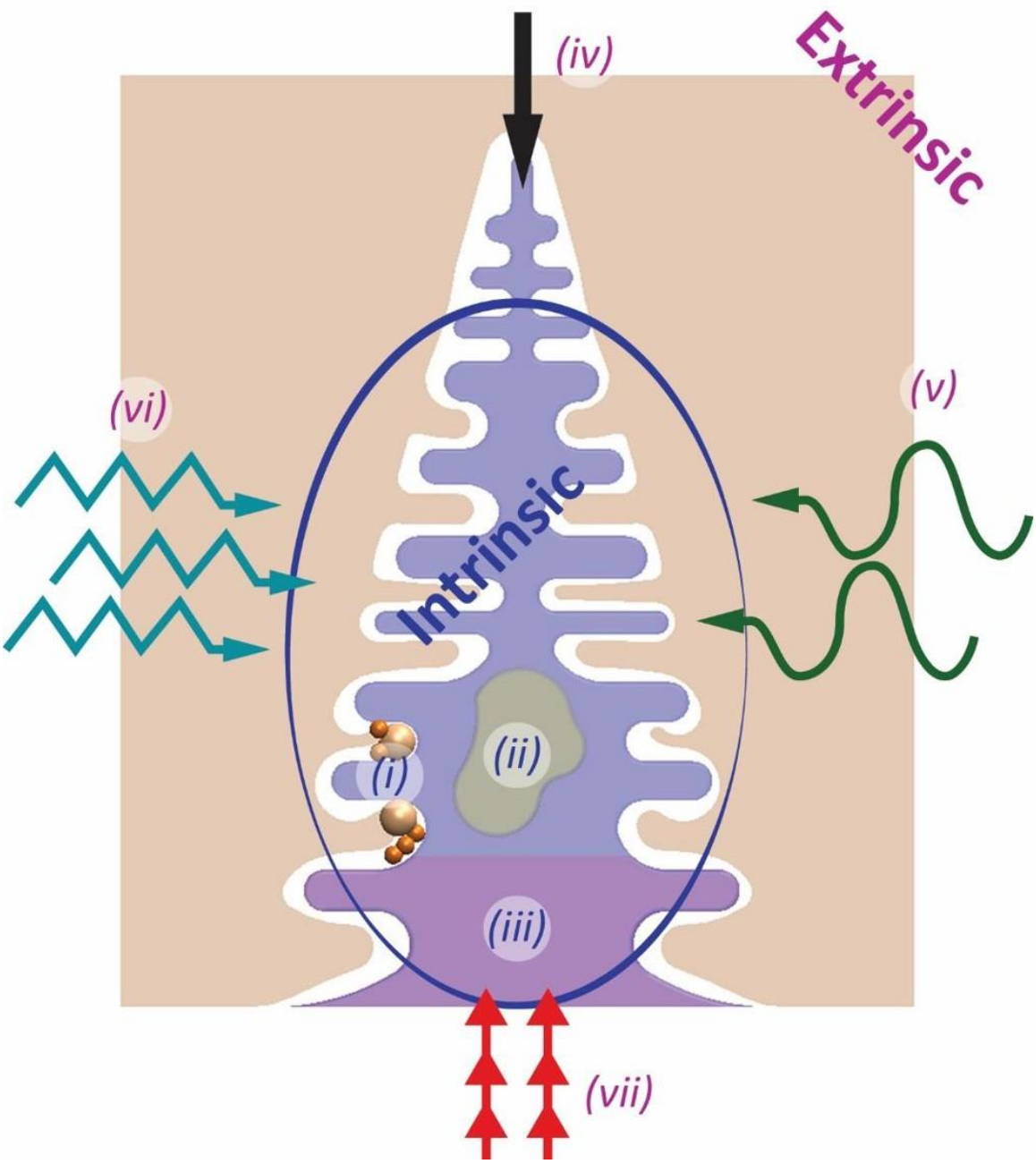

Figure 3.5: Diagram of intrinsic and extrinsic methods of control over the freeze casting process. Intrinsic methods: (i) Variations of particle size; (ii) Additives to the slurry; (iii) The use of different freezing agents. Extrinsic methods: (iv) The use of external templates; (v) The use of magnetic fields; (vi) The use of electrical fields; (vii) Variations to the freezing rate [36].

3.2 Magnetic Freeze Casting with Different Size Magnetized Alumina Particles

3.2.1 Introduction

Gravity and electromagnetism are natural forces responsible for celestial body assembly in the universe. Earth's magnetic field plays a role in "biological body" assembly, or how living organisms orient themselves with respect to their surrounding environment [37]. Biogenic magnetite (Fe_3O_4) has been found in sharks [38], pigeons [39], honeybees [40], humans [41], and most notably in magnetotactic bacteria that align parallel to the earth's magnetic field direction in search of microaerophilic regions of low oxygen concentration [42]. These bacteria have single domain Fe_3O_4 crystals packaged within organelle magnetosomes that form a chain along the long axis of the bacteria. Magnetosome alignment within these bacteria provides an interesting avenue for bioinspired applications that use aligned materials to resemble naturally ordered structures.

Strong magnetic fields (≈ 9-18 T) have been used along with a slip casting process to finely control and texture anisotropic ceramic particles to improve their physical, chemical and mechanical properties [43-51]. Macroscopic alignment occurs when the magnetic energy on rotation exceeds the thermal energy for the slurry particles. In addition to the strong magnetic field, the degree of particle orientation depends on several processing factors, such as heating temperature, particle size and suspension viscosity [46]. Magnetic slip casting used at much lower magnetic field strength (< 40 mT) can also be used to manipulate surface magnetized alumina (Al_2O_3) platelets [52]. Fine control over these materials has led to reinforced composites [5, 53-55], self-shaping composites [56], tunable fluorescence emission [57], and additive manufacturing processes such as 3D magnetic printing [58, 59].

Bone consists of nanomaterials (grains, platelets or fibers) organized into a hierarchical structure that form a composite with high strength and toughness [60]. It must be strong to support the body, tough to absorb impact forces, lightweight to enable movement, and porous to replenish nutrients [61, 62]. Cortical bone provides a dense outer sheath while the inner trabecular bone enables marrow production and cell growth within the large interconnected pores of the spongy bone interior [62]. Pore alignment in load bearing regions is an important design feature along with prevention of pore expansion due to osteoporosis [63]. Fabrication of aligned porous structures that resemble trabecular bone necessitates methods that can provide dual levels of control over structural features with disparate length scales and along multiple directions.

Freeze casting is a physical process that uses an aqueous slurry consisting of a particulate solid phase (e.g., ceramic particles) and a freezing agent (e.g., water) to fabricate a porous scaffold [14, 64-67]. First, ice templated crystal growth separates particles into lamellar structures aligned along the freezing direction (z-axis). Following freeze drying and sintering steps to remove ice crystals and strengthen the overall macrostructure, respectively, the resulting porous scaffold has lamellar walls interconnected by mineral bridges. The quantity and dimension of the pores can be modified by adjusting the solid loading [68, 69], changing the liquid freezing agent [70-72], and introducing additives [73-77]. Alumina has often been used for the solid particles in prior freeze casting work that varied experimental parameters and characterization techniques [77-80]. Although scaffolds are typically strong in the ice growth direction, mechanical properties in transverse directions (*x*, *y*-axes) normal to the freezing direction are generally poor due to non-aligned lamellar walls.

Various techniques for transverse lamellar alignment within freeze cast scaffolds exist [81-84], however, Porter, et al. were first to apply a magnetic field during freeze casting for that purpose [1]. When subjected to a transverse magnetic field (≈ 120 mT, *y*-axis) normal to the ice growth direction (*z*-axis), a slurry of paramagnetic titania (TiO_2, 200-500 nm) and ferromagnetic Fe_3O_4 (≈ 50 nm) aligned lamellar walls to make mechanically enhanced scaffolds. Magnetic freeze casting with a slurry of diamagnetic zirconia (ZrO_2, 200-500 nm) and Fe_3O_4 in a rotating magnetic field (≈ 120 mT) made torsion enhanced helical banded scaffolds [3], while a transverse magnetic field (≈ 90 mT) made scaffolds with bridge-like features [4]. Distinct phase separation occurred with ZrO_2, but not with TiO_2, which was due to lack of interparticle interaction with Fe_3O_4 when subjected to the applied magnetic field.

Superparamagnetism occurs in smaller Fe_3O_4 particles (< 15-20 nm) as a super moment that can easily flip in response to a changing magnetic field when the particle thermal energy (k_BT, Boltzmann's constant · temperature) exceeds the magnetic anisotropy energy barrier ($K_{eff}V$, anisotropy constant · particle volume) [85]. Dynabeads® (Thermo Fisher Scientific, Waltham, MA) use a superparamagnetic Fe_3O_4 particle core and functionalized polystyrene shell for magnetic separation applications [86]. An alternative surface magnetization method uses an aqueous suspension of dispersed superparamagnetic Fe_3O_4 (ferrofluid) coated with charged surfactant that can electrostatically adsorb onto particles. This method uses the point-of-zero charge (PZC), the pH when particles become electrostatically neutral in water [87], and the hydroxylated surface is protonated or deprotonated according to Gouy-Chapman theory [88]. Since Al_2O_3 (PZC ≈ 9) [89] in

water (PZC ≈ 7) is protonated, anionic charged Fe_3O_4 can surface magnetize Al_2O_3 particles through electrostatic adsorption.

Equations that describe chain formation of single domain Fe_3O_4 (≈ 50 nm) in magnetosomes of magnetotactic bacteria [90] can be used to predict how isolated superparamagnetic Fe_3O_4 particles [91] and Dynabeads® [92, 93] in water respond to a magnetic field gradient. The maximum value of the magnetic interaction energy (U^*) is indicated in Eqn. 1:

$$U^* = \frac{\mu_0 m^2}{2\pi d^3} \tag{1}$$

where μ_0 is the magnetic permeability of free space (4π x 10^{-7} H/m), m is the particle magnetic moment dipole and d is the center-center interparticle distance (equal to one particle diameter for particles touching in a chain) [94]. The ratio between U^* and thermal energy (k_BT) is the magnetic coupling parameter (Γ) indicated in Eqn. 2 (Figure 3.6):

$$\Gamma = \frac{U^*}{k_B T} = \frac{\mu_0 m^2}{2\pi d^3 k_B T} \tag{2}$$

However, a value of $\Gamma > 1$ by itself does not account for thermodynamic considerations due to loss of entropy associated with chain formation. The solution conditions responsible for the balance between energy and entropy are incorporated in the aggregation parameter (N^*) indicated in Eqn. 3:

$$N^* = \sqrt{\phi_o e^{\Gamma - 1}} \tag{3}$$

where ϕ_o is the volume fraction (vol%) of the slurry. For example, a 10 vol% slurry necessitates $\Gamma > 3.31$ to get chain formation at $N^* > 1$. For magnetic freeze casting, where particle self-assembly into chains is desirable for fabricating aligned lamellar structures,

Eqn. 3 provides a valuable predictive tool based on measurable parameters that mechanical characterization of sintered scaffolds can further validate.

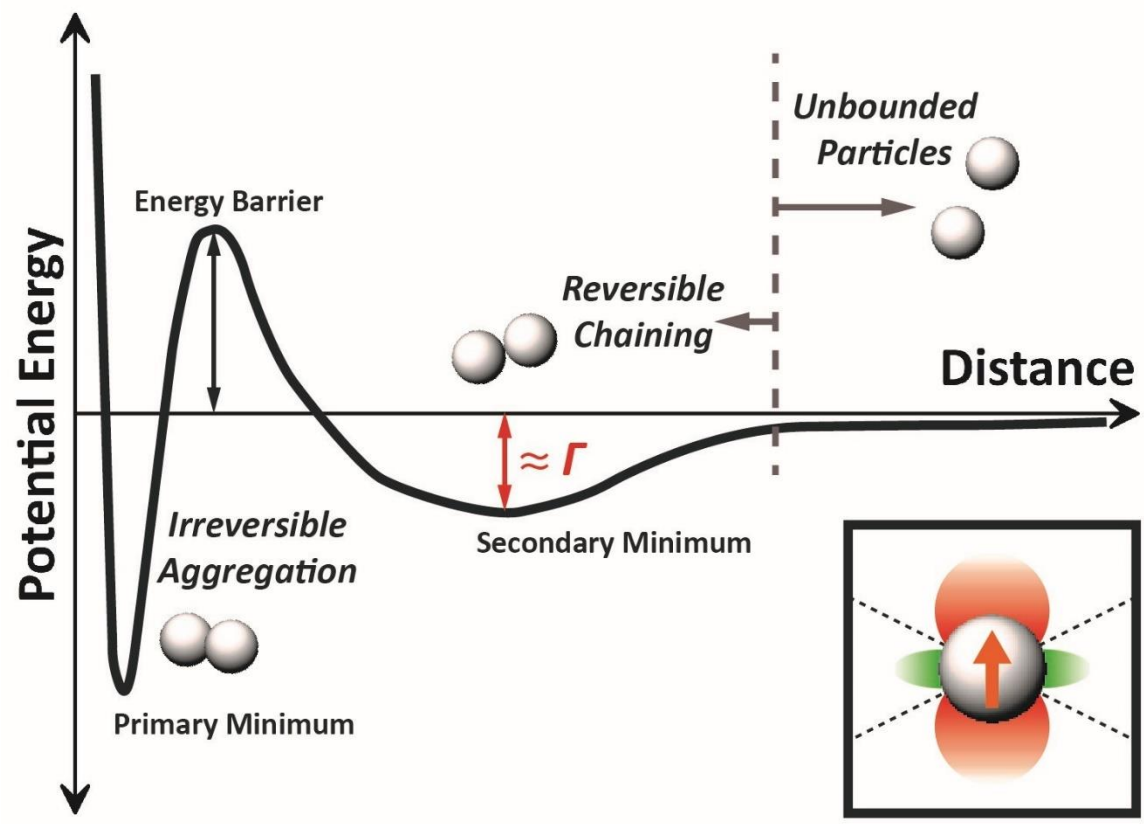

Figure 3.6: Free energy profile diagram of interaction between electrostatically stabilized spherical particles that have been surface magnetized with superparamagnetic particles and subjected to a strong magnetic field. Assumptions applied from a generalized DLVO theory include a deep primary minimum (van der Waals attraction), an energy barrier (electrostatic repulsion) and a secondary minimum (magnetic interaction, vertical, indicated in red) where chain formation occurs according to the magnetic coupling parameter (Γ) value. Repulsive regions (horizontal, indicated in green) exist on the sides due to the particle dipole (up arrow, indicated in orange) oriented in the magnetic field direction.

This work investigates a new method for making multi-axis strengthened porous structures that resemble trabecular bone by magnetic freeze casting with surface magnetized Al_2O_3 particles. Magnetic control over superparamagnetic Fe_3O_4 electrostatically adsorbed to Al_2O_3 particles leads to lamellar wall alignment and stiffness enhancement in the transverse direction. Structural materials typically used for freeze casting that are either paramagnetic (e.g., TiO_2) or diamagnetic (e.g., ZrO_2, Al_2O_3,

hydroxyapatite) can become magnetically responsive at low magnetic field strength. Thus, macro and microstructural feature control by magnetic freeze casting can provide a feasible fabrication pathway towards dynamic material systems that sense, interact with and even adapt to the surrounding environment [95].

3.2.2 Materials and Methods

3.2.2.1 Particle Surface Magnetization

Three different α-Al_2O_3 particles (BMA15, 150 nm; SM8, 350 nm; CR6, 500 nm; bulk density of 3960 kg/m^3 [96]; particle size estimated by supplier Baikowski, Malakoff, TX, USA) were surface magnetized (Figure 3.7). For each particle size, 2.5 g Al_2O_3 was stirred in 75 mL distilled water, while 100 µL of anionic ferrofluid (EMG-705, 1-4 vol% Fe_3O_4 nanoparticles, Ferrotec, Bedford, NH, USA) was diluted in 5 mL distilled water in a separate container and dropwise added to the stirring Al_2O_3 solution at 700-800 rpm (RO 15 P S1, IKA Works, Wilmington, DE, USA). After stirring for 12 hours, white colored Al_2O_3 particles changed to a light brown color and the surrounding solution became clear. Residual anionic surfactant was rinsed off from magnetized particles with distilled water and vacuum filtration. The magnetized Al_2O_3 was then dried for 12 hours at 100˚C before use in magnetic freeze casting slurries.

3.2.2.2 Magnetic Materials Characterization

Magnetized Al_2O_3 particles (≈ 15-30 mg) were characterized with a vibrating sample magnetometer (VSM, VersaLab, Quantum Design International, San Diego, CA, USA) with moment measured in response to a sweeping magnetic field (0-3000 Oe). Mass magnetization (*M*, emu/g) and particle magnetic moment (*m*, Am^2) were calculated from

magnetometer measurements coupled with particle volume (v) measured by the dynamic light scattering (DLS) technique, using Eqns. 4 and 5:

$$M = moment/sample\ weight \quad (4)$$

$$m = v \times M \quad (5)$$

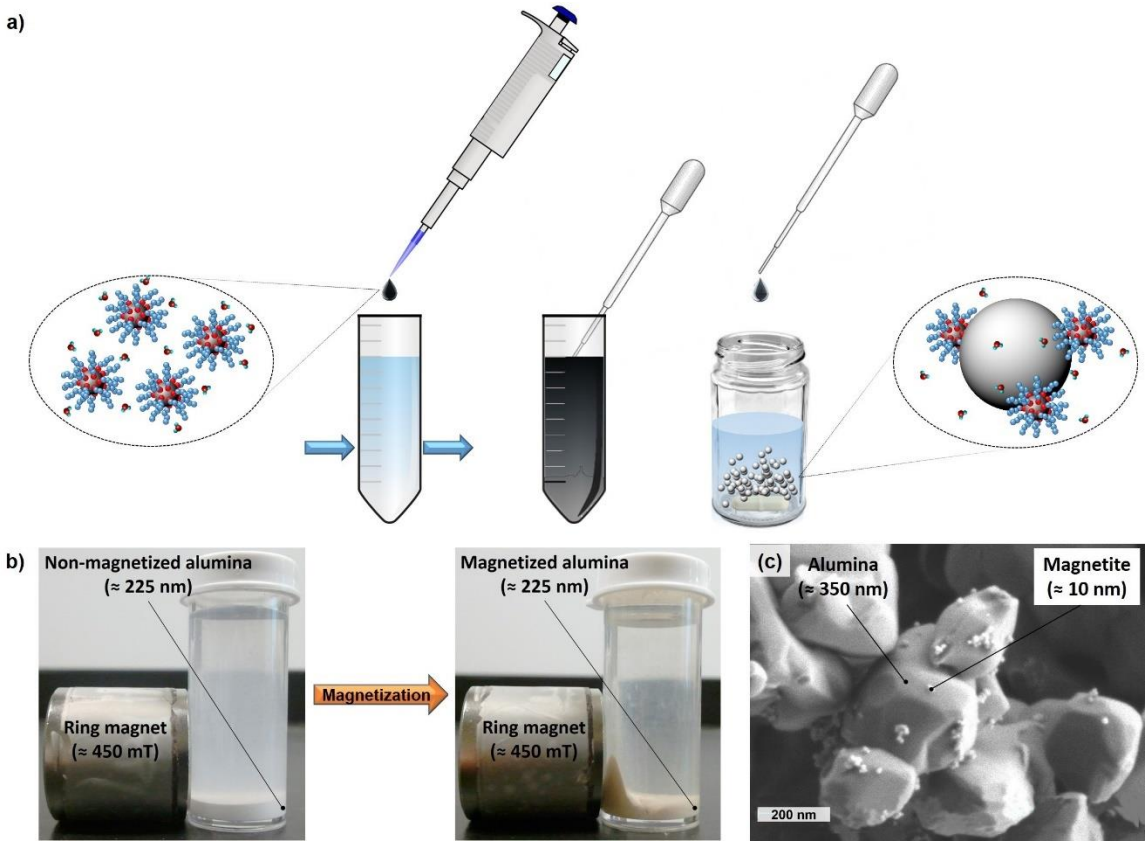

Figure 3.7: Preparation of surface magnetized Al_2O_3 particles. (a) Ferrofluid consisting of Fe_3O_4 nanoparticles (≈ 10 nm) coated with an anionic surfactant was diluted and dropwise added to a stirring Al_2O_3 slurry. (b) Non-magnetic Al_2O_3 particles (left) became magnetized (right) after stirring for 12 hours. (c) Scanning electron micrograph of Fe_3O_4 nanoparticles on Al_2O_3 (≈ 350 nm) appeared inhomogeneous, however, magnetic moment measurement of surface magnetized Al_2O_3 particles indicated Fe_3O_4 effectively functioned as though uniformly distributed onto Al_2O_3 in bulk.

3.2.2.3 Magnetized Slurry Preparation

Magnetized Al_2O_3 particle slurries (10 vol%) were prepared (by weight Al_2O_3) with polymer binders 1 wt.% polyvinyl alcohol (PVA, 100,000 g/mol molecular weight (MW), Alfa Aesar, Ward Hill, MA, USA), 1 wt.% polyethylene glycol (PEG, 10,000 g/mol MW, Alfa Aesar, Ward Hill, MA, USA) and 1 wt.% anionic dispersant (Darvan 811, R. T.

Vanderbilt Company, Inc., Norwalk, CT, USA). Al_2O_3 grinding media was added to the slurry and the mixture was ball milled for 24 hours. After milling, particle sizes measured at least twenty times by DLS (Microtrac Nanotrac Wave II, Montgomeryville, PA) provided a number distribution of the mean particle diameter [97-99].

3.2.2.4 Magnetic Freeze Casting

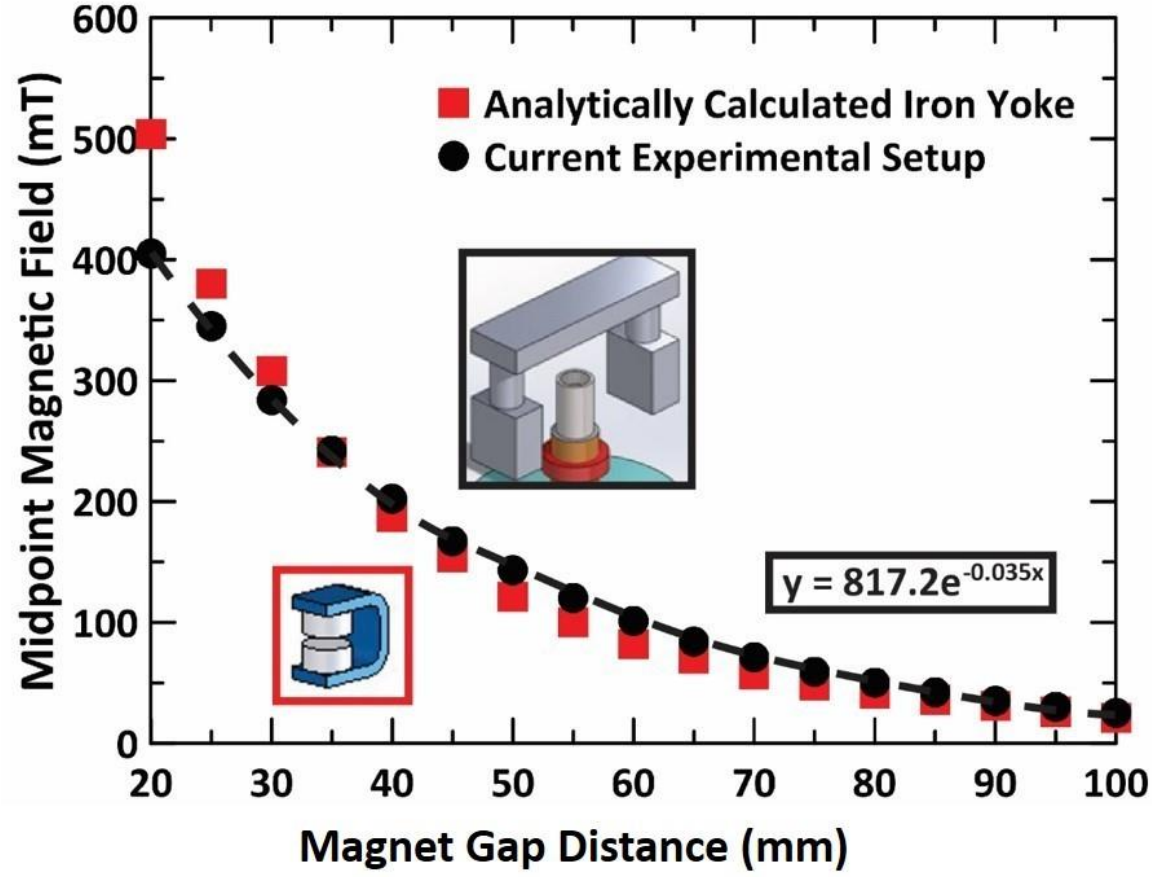

Figure 3.8: Gap magnetic field strength determination via theoretical calculation and measurement. Plotted red squares indicate calculated magnetic field strength at increasing gap distances for two disc magnets attached to an iron yoke. Plotted black circles and trend line indicate measured magnetic field strength at increasing gap distances with a Gauss meter at the center point between bar magnets.

A vise grip (Panavise, Reno, NV) with ≈ 420 mT bar magnets (N52 grade, K&J Magnetics, Inc. Pipersville, PA, USA) attached to either end allowed for a static magnetic field apparatus that was adjustable. A handheld Gauss meter measured the magnetic field

strength at the gap, located at the midpoint between the magnets. An exponential curve fit from the data points was acquired at successively increasing 5 mm gap intervals, yielding an equation for conversion of gap distance to magnetic field strength. The Gauss meter measurements closely resembled calculated values for two disc magnets attached to an iron yoke (Figure 3.8). Freeze casting with magnetized Al_2O_3 subjected to no magnetic field versus a static transverse magnetic field (≈ 25, 75, 150 mT) was accomplished in a polyvinyl chloride (PVC) mold. A groove was filed along the inside wall of the mold and aligned perpendicular to the magnetic field axis to provide a visual indicator where the magnetic field was applied on the sintered samples.

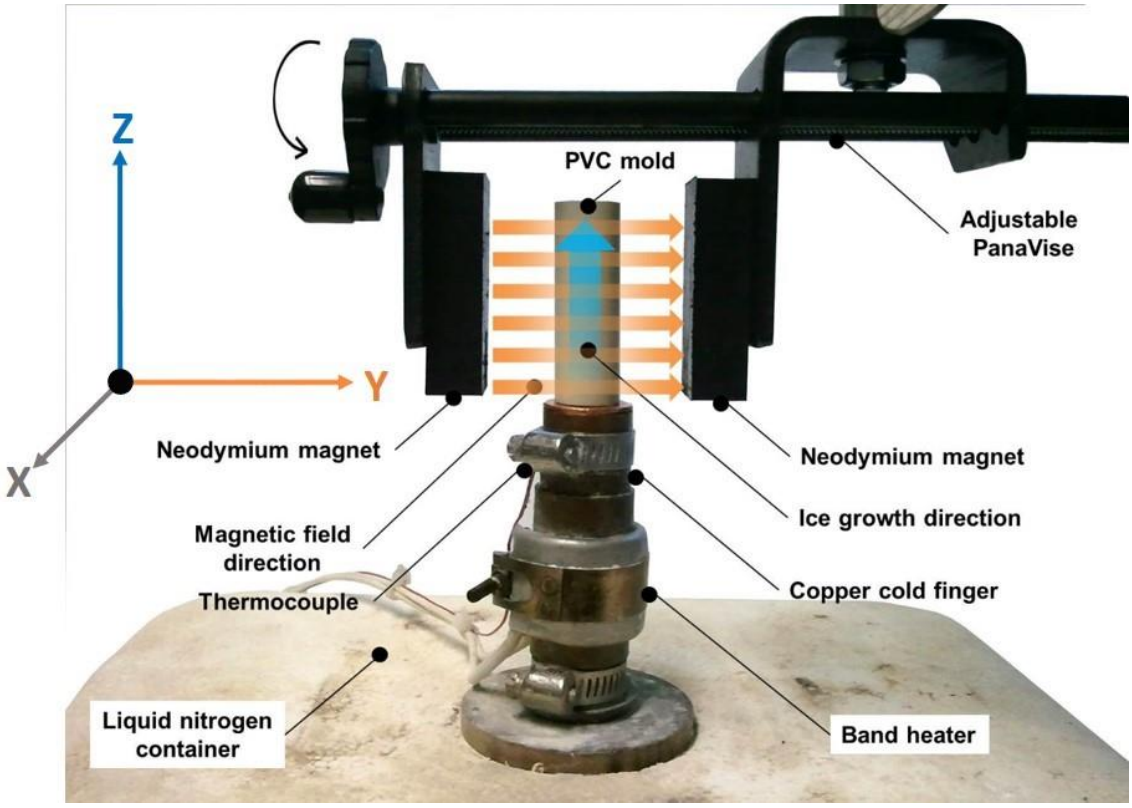

Figure 3.9: Magnetic freeze casting setup. Ice crystals grow along the z-axis while a static magnetic field is applied along the y-axis.

Each surface magnetized Al_2O_3 slurry was degassed under low vacuum for 15 minutes before pouring 5 mL into the PVC freeze cast mold. The static magnetic field apparatus was situated and centered over the PVC mold (Figure 3.9). Directional freezing occurred from the bottom upward using a custom built freeze casting device, as previously described [1]. Frozen solid samples were lyophilized with a bench-top freeze dryer (Labconco, Kansas City, MO, USA) at -50°C and 3.5 x 10^{-6} Pa for 48 hours. Ice crystals sublimed leaving behind fragile 'green body' scaffolds composed of particles held together by the polymer binders. Samples were sintered in an open air furnace for 3 hours at 1500°C with heating and cooling rates of 2°C/min, following a procedure that provided reproducible results with uniform porosity [1].

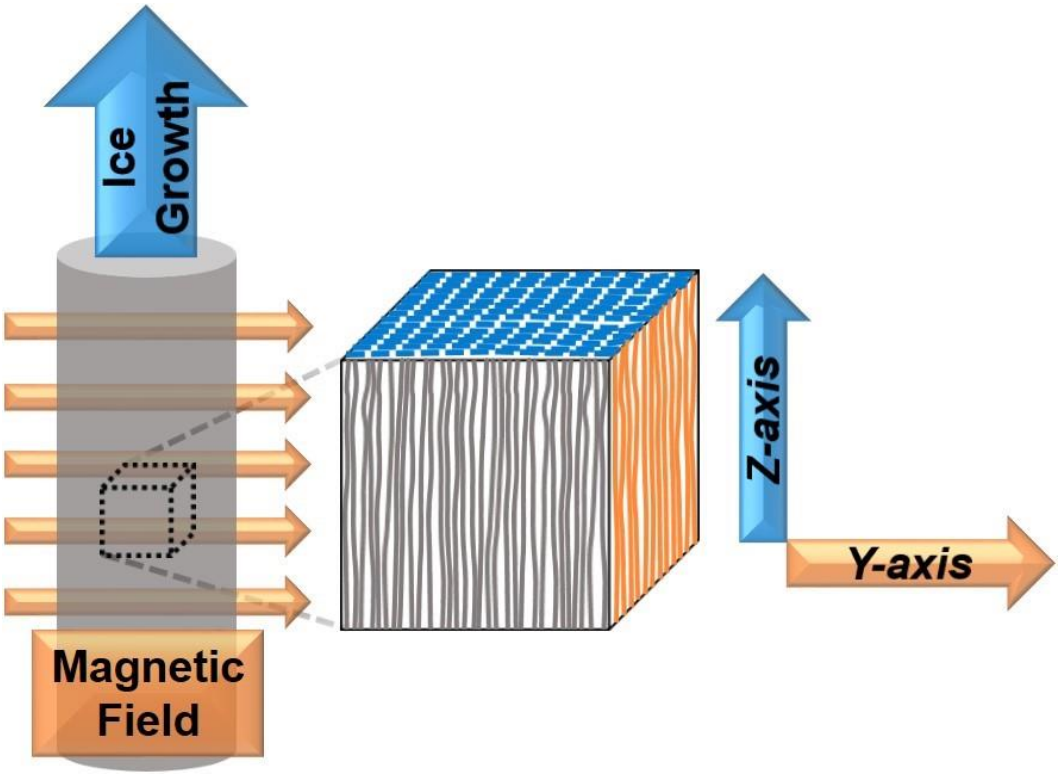

Figure 3.10: Sintered scaffold cube compression diagram. Mechanical properties are compared via cubes from the center of the sintered scaffold compressed in the ice growth direction (z-axis, blue cube face) and the magnetic field direction (y-axis, orange cube face).

3.2.2.5 Mechanical Characterization

A total of six scaffolds were prepared for each condition with Al_2O_3 particle size (195, 225, 350 nm) and magnetic field strength (75, 150 mT) as variables. Compression testing of sintered Al_2O_3 scaffolds was performed on a 3342 Instron materials testing machine (Instron, Norwood, MA) with a 500 N static load cell at a crosshead velocity of 0.005 mm/s following previous procedures [1, 4, 75, 76]. Two samples (≈ 5 mm^3 cubes) cut from each scaffold center (Figure 3.10) were compressed, one in the ice growth direction (*z*-axis) and the other in the magnetic field direction (*y*-axis). Ultimate compressive strength and Young's modulus were determined from the maximum stress and linear slope of the stress–strain curves, respectively.

3.2.2.6 Scanning Electron Microscopy Characterization

Two of the six sintered scaffolds for each condition were sectioned at midpoint height, mounted to a stage and coated with colloidal graphite along the bottom and side walls. Iridium was sputter coated (EMITech K575X, Quorum Technologies Ltd., West Sussex, UK) for 15 s at 85 mA onto the top. Scanning electron microscopy (SEM) micrographs at 10 kV (spot size 3 nm) from a Philips XL30 field emission environmental scanning electron microscope (FEI-XL30, FEI Company, Hillsboro, OR) were used to characterize scaffold pore dimensions and look for general trends in lamellar wall alignment (horizontal, angled, none). Image analysis with ImageJ software (National Institutes of Health, Bethesda, MD, USA) maintained a contrast threshold at a consistent value in all micrographs. An ellipse fit to each measured pore provided dimensions for the major axis (*a*) and minor axis (*b*). For each scaffold, 40 individual pores were measured to

obtain pore area ($A_p = \pi ab/4$) and lamellar wall thickness (t), which was how other scaffolds were analyzed in previous work [75, 76].

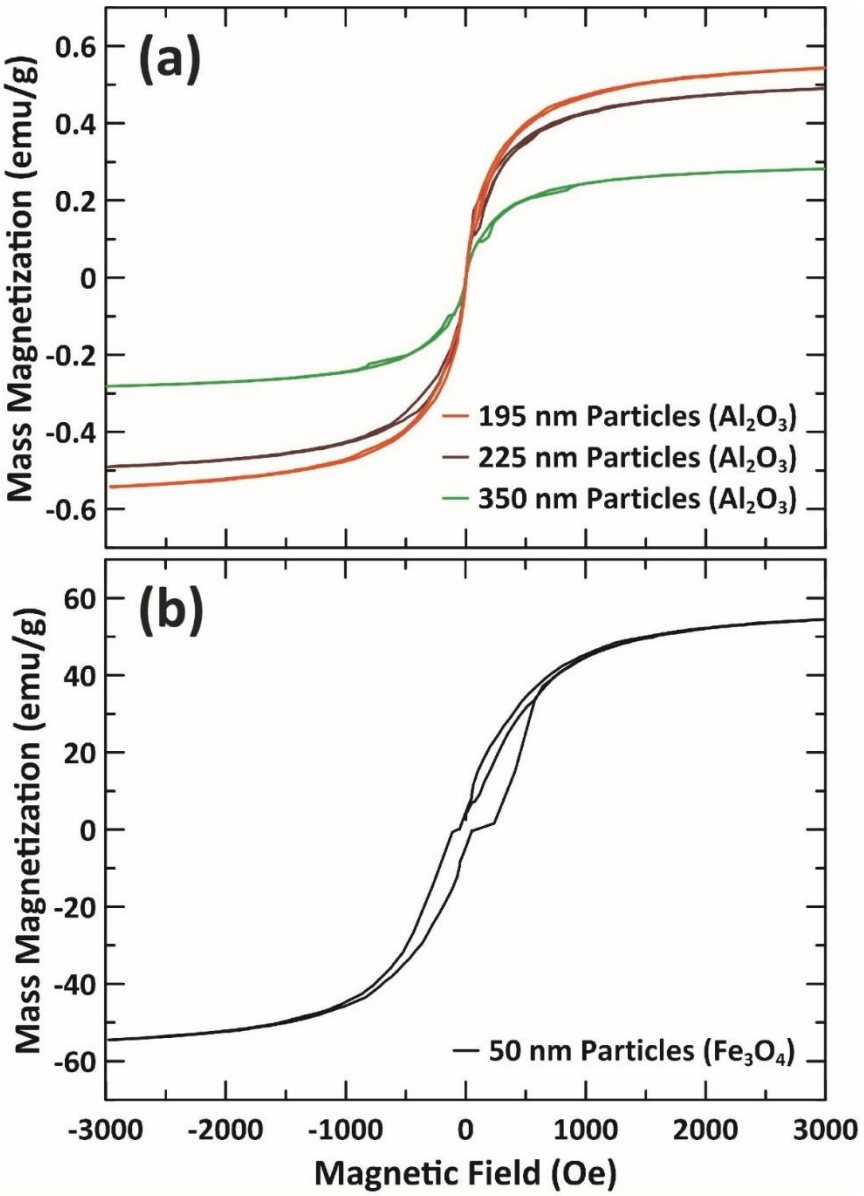

Figure 3.11: Comparison between surface magnetized Al_2O_3 particles (195, 225, 350 nm) and Fe_3O_4 nanoparticles (50 nm) subjected to a sweeping magnetic field (-3000 to 3000 Oe) and plotted versus mass magnetization (emu/g). (a) Curves for magnetized Al_2O_3 particles have an absence of hysteresis and magnetization at $H = 0$ due to adsorbed superparamagnetic Fe_3O_4 nanoparticles (10 nm). (b) 50 nm Fe_3O_4 nanoparticles exist in a single domain state and align uniformly with an applied magnetic field. Evidence of hysteresis and magnetization at $H = 0$ indicate ferromagnetic instead of superparamagnetic properties.

3.2.3 Magnetic Response of Magnetized Alumina Particles

M-H curves from VSM measurements for surface magnetized Al_2O_3 particles (Figure 3.11) subjected to a sweeping magnetic field, *H*, and plotted versus *M* (emu/g, Eqn. 4) indicated an absence of hysteresis and magnetization at $H = 0$. These results support the applicability of Eqns. 1-3 from Faraudo, et al. [94] for chaining of composite superparamagnetic colloids. Interactions between surface adsorbed 10 nm Fe_3O_4 on neighboring Al_2O_3 particles that might have affected overall superparamagnetic properties were not observed. *M-H* curve values for susceptibility (maximum slope) and saturation (maximum mass magnetization) from surface magnetized Al_2O_3 were lessened compared with superparamagnetic Fe_3O_4 nanoparticles alone [100], but resembled values for composites with superparamagnetic Fe_3O_4 cores [101]. Additional VSM measurement of 50 nm Fe_3O_4 not used in this work confirmed the presence of hysteresis and magnetization at $H = 0$ for single domain, ferromagnetic nanoparticles that are not superparamagnetic (Figure 3.11).

Al_2O_3 particle sizes were estimated by the supplier to be 150 nm (BMA15), 300 nm (SM8) and 500 nm (CR6), however, average particle sizes measured by DLS after ball milling were actually 195 nm, 225 nm and 350 nm, respectively (Figure 3.12). Since Al_2O_3 particles (195, 225, 350 nm) with equal mass (2.5 g) and density (3.96 g/cm^3) were surface magnetized with equal ferrofluid volume (0.1 mL), adsorbed amount of Fe_3O_4 nanoparticles (10 nm) onto each Al_2O_3 particle could be estimated with assumptions for spherical particle shape and Fe_3O_4 fraction in ferrofluid (4 vol%). Individual 195, 225 and 350 nm Al_2O_3 particles had an estimated 47, 72 and 272 adsorbed Fe_3O_4 nanoparticles, respectively.

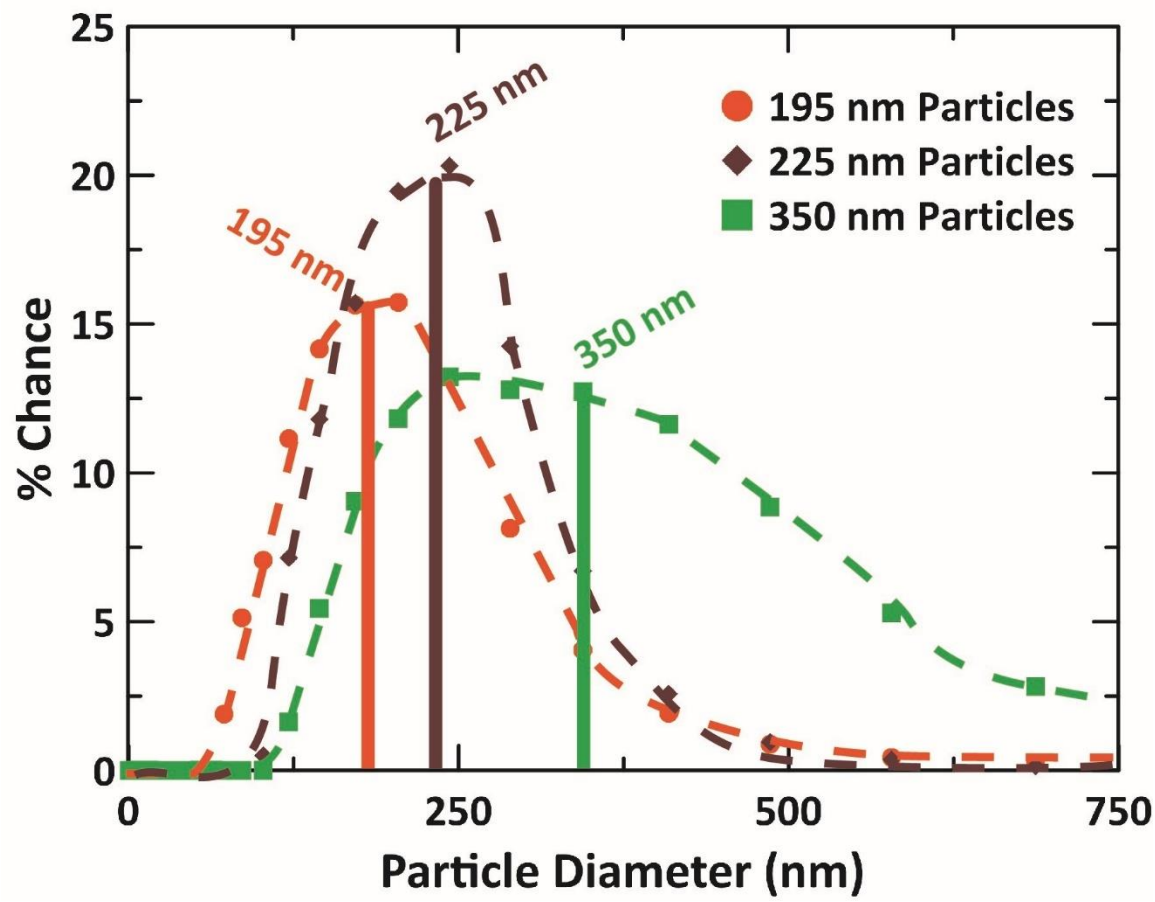

Figure 3.12: Dynamic light scattering measurement of alumina particle sizes. Each particle type was segmented into a mean number distribution that consisted of particle percentage at different particle size bins and plotted for comparison. The product of each particle percentage with corresponding bin size was summed to determine the reported mean for each particle type.

Comparison between Al_2O_3 particle sizes demonstrated that 195 and 225 nm particles had ≈ 1.9x and ≈ 1.7x greater *M* values, respectively, than 350 nm particles (Figure 3.13). Surface area to volume ratios for 195 nm and 225 nm particles were similarly ≈ 1.8x and ≈ 1.6x times greater, respectively, than for 350 nm particles. Multiplying *M* by mass of an individual Al_2O_3 particle (195, 225, 350 nm) plus adsorbed Fe_3O_4 (47, 72, 272 nanoparticles, respectively) yielded magnetization values of 6.83 x 10^{-15}, 9.46 x 10^{-15} and 1.97 x 10^{-14} emu for surface magnetized 195, 225 and 350 nm Al_2O_3, respectively, at 75 mT magnetic field strength. The magnetization per particle value for surface magnetized

350 nm Al_2O_3 was ≈ 2.1x and ≈ 2.9x greater than for 195 and 225 nm Al_2O_3, respectively, which mirrored *m* values (Am^2, Eqn. 5) for each composite particle size at varying magnetic field strength. Since Γ is proportional to m^2 (Eqn. 2), larger particles were more likely to overcome thermal agitation dominance and Brownian motion compared with smaller particles [92].

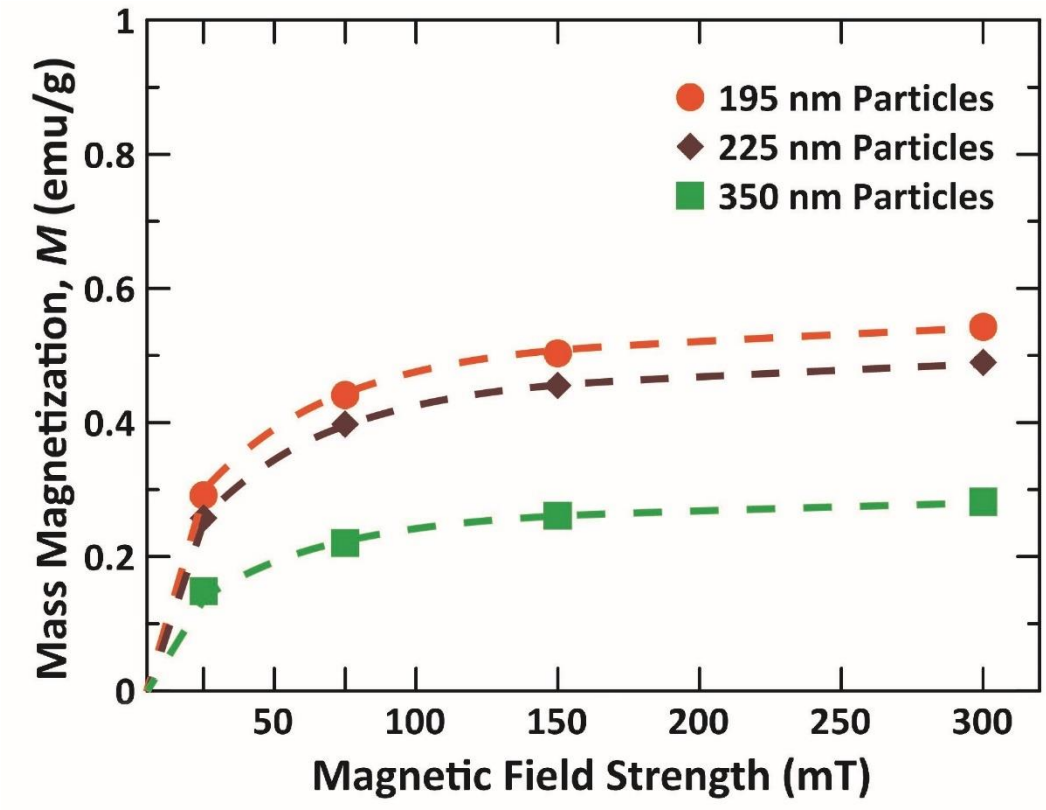

Figure 3.13: Comparison of mass magnetization, *M*, determined from magnetometer measurements for different sized magnetized alumina particles. The value *M* is the measured magnetic moment divided by the sample weight. Greater surface area to volume ratio for smaller particles leads to greater values for *M* at various magnetic field strengths.

DLS measured average Al_2O_3 particle size, *d*, and VSM measured moment, *m*, were combined in Eqn. 2 to obtain Γ as a function of applied magnetic field strength (left side, Figure 3.14a-c). For each average particle size, Γ fell below the threshold for dipole-dipole interaction dominance when magnetic interaction energy exceeds thermal agitation ($\Gamma > 1$)

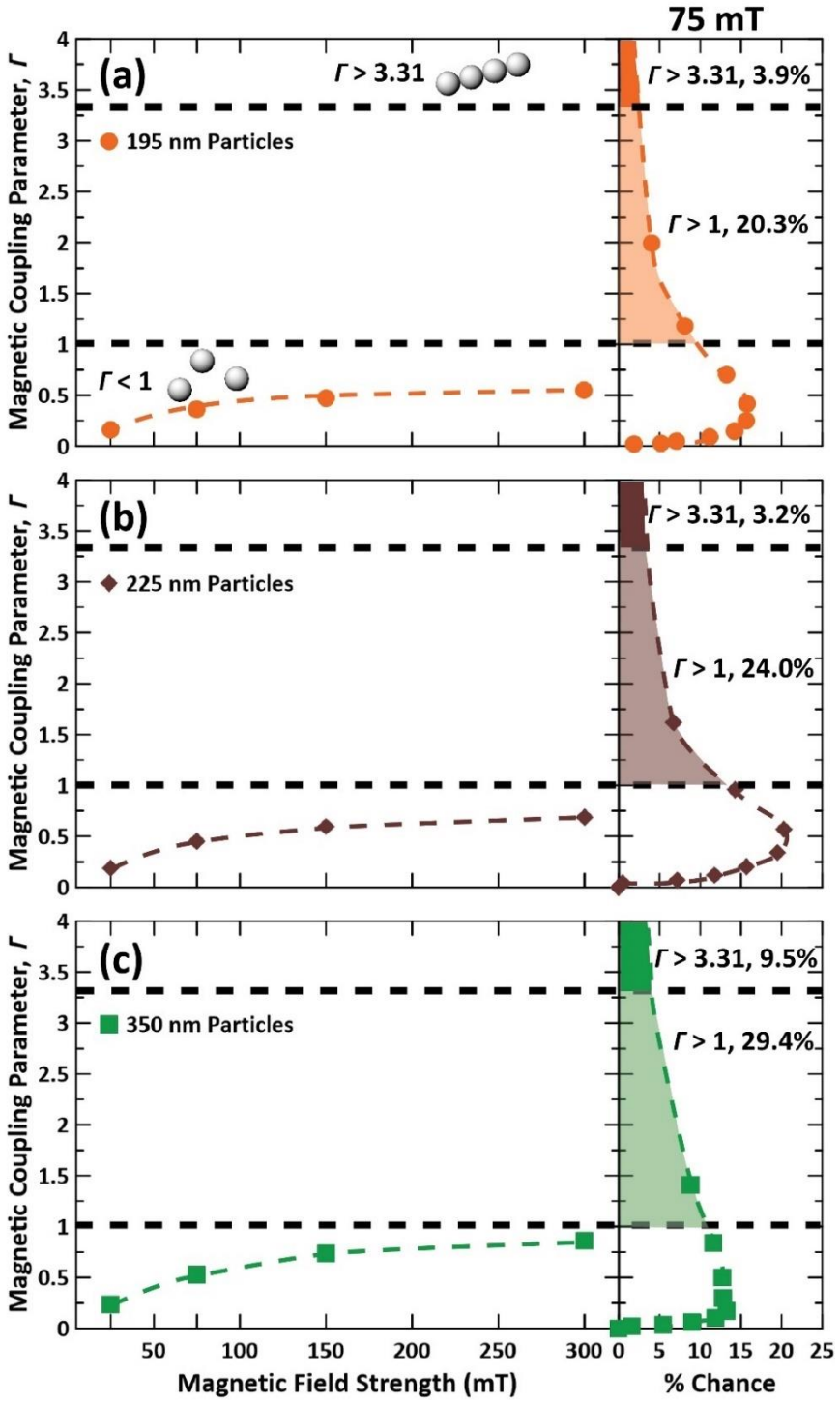

Figure 3.14: Comparison of calculated magnetic coupling parameter (Γ) values and mean number distribution of particle sizes for different sized alumina particles. Average particle sizes for (a) 195 nm, (b) 225 nm and (c) 350 nm particles did not exceed $\Gamma > 1$ or $\Gamma > 3.31$ thresholds at any magnetic field strength. Mean number distribution measurements for particle sizes indicated a higher percentage of larger particles (350 nm) exceeded $\Gamma > 1$ and $\Gamma > 3.31$ thresholds at 75 mT.

as well as the threshold for particle chain formation when $N^* > 1$ for a 10 vol% slurry ($\Gamma > 3.31$). Since average particle size poorly represents the actual size disparity evident in a mean number distribution for each Al_2O_3 particle type (Figure 3.12), Γ was calculated at each DLS measured particle size by percent chance within the overall slurry. The percentage of each particle type above $\Gamma > 1$ and $\Gamma > 3.31$ thresholds at a magnetic field strength of 75 mT is indicated (right side, Figure 3.14a-c). The 195, 225 and 350 nm particles had 20.3%, 24.0% and 29.4% of each type above $\Gamma > 1$, respectively, while 3.9%, 3.2% and 9.5% were above $\Gamma > 3.31$, respectively. Meanwhile at 150 mT, the 195, 225 and 350 nm particles had 26.9%, 34.3% and 37.4% of each type above $\Gamma > 1$, respectively, while 6.0%, 5.1% and 12.9% were above $\Gamma > 3.31$, respectively.

3.2.4 Lamellar Wall Alignment

During the time before freezing started, larger magnetized particles subjected to an applied magnetic field likely aggregated in a manner similar to previously reported 1D chain formation of Fe_3O_4 nanoclusters at room temperature in aqueous solution [102]. Additional experiments confirmed ice nucleation and crystal growth initiated at 247 K in freeze cast slurries, thus that temperature value was used in Eqn. 2 to calculate Γ values (Figure 3.14). As slurry temperature decreased steadily (-10 K/min) from 283 K to 103 K during freeze casting, the applied magnetic field increased interaction energy between magnetized Al_2O_3 particles within the supercooled slurry for 3-4 minutes until ice growth started at 247 K. The percentage of larger slurry particles with enhanced interaction energy above $\Gamma > 1$ and $\Gamma > 3.31$ likely guided the formation of lamellar walls aligned along magnetic field lines between growing ice crystals. Mineral bridges made up of particles

trapped within the growing ice front connected between adjacent lamellae in a similar fashion as in normal freeze casting.

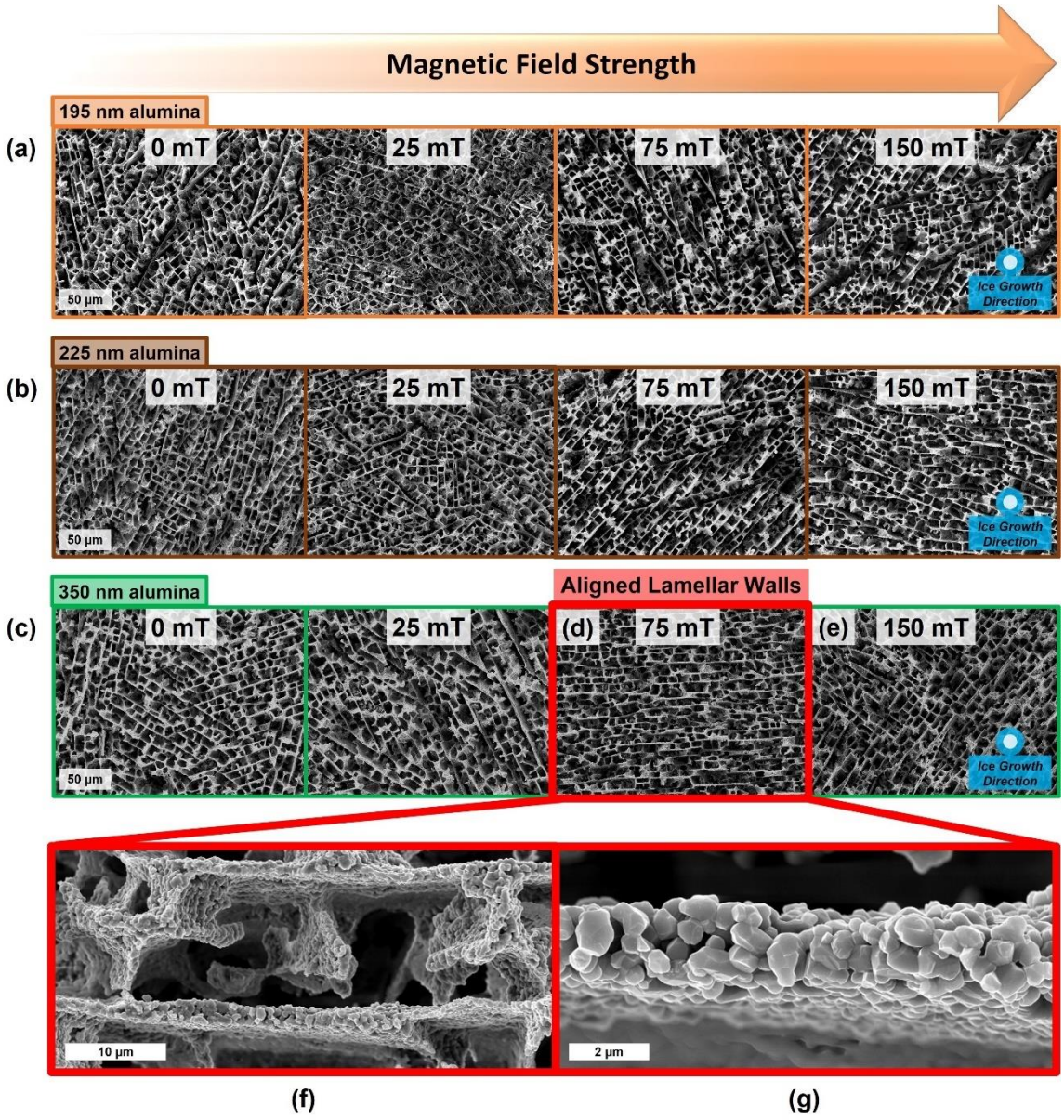

Figure 3.15: Scanning electron micrographs of scaffold center regions for different sized magnetized alumina particles after magnetic freeze casting at 0, 25, 75 and 150 mT. (a) 195 nm alumina particles did not exhibit lamellar wall alignment at any of the applied magnetic fields, while (b) 225 nm alumina particles had limited alignment at 150 mT. (c) 350 nm alumina particles had lamellar wall alignment that was most evident at (d) 75 mT, however, at (e) 150 mT there was angled alignment likely due to flux field effects. (f) Closer examination of the scaffold microstructures shows mineral bridge formation and (g) particles sintered together within lamellar walls aligned along the magnetic field axis.

In Figure 3.15, SEM micrographs from the center of the scaffolds show transverse cross-sections perpendicular to the ice growth direction (Figure 3.15a-c). No lamellar wall alignment occurred during freeze casting when there was no applied magnetic field. All the magnetic field conditions for 195 nm scaffolds had no lamellar wall alignment along the magnetic field axis (Figure 3.15a). Some aligned regions were evident for 225 nm scaffolds at 150 mT, but not at lower strength magnetic fields (Figure 3.15b). For 350 nm scaffolds (Figure 3.15c), more horizontal lamellar wall alignment occurred at 75 mT (Figure 3.15d) than at 150 mT (Figure 3.15e). High magnification SEM micrographs of 350 nm scaffolds showed horizontally aligned lamellar walls at 75 mT (Figure 3.15f,g) along the magnetic field axis.

Image analysis of stitched together SEM micrographs (6 mm x 2.7 mm) from the center of 350 nm scaffolds indicated ≈ 20% horizontal lamellar wall alignment at 75 mT (Figure 3.16a) and ≈ 12% horizontal alignment at 150 mT (Figure 3.16b). Among the scaffolds analyzed for each condition, a generally observed trend from SEM micrographs was that a sufficient (75 mT), but not excessive (150 mT), amount of applied magnetic field strength was best to induce horizontal, rather than angled, lamellar wall alignment in the 350 nm scaffold center. Since a greater percentage of magnetized 350 nm Al_2O_3 particles had greater Γ values (Figure 3.14), aggregation and subsequent alignment of those larger particles within lamellar walls should be indicative of more susceptibility to increased magnetic field strength. Lamellar wall alignment was not uniformly horizontal or angled at 75 mT or 150 mT, respectively, so further reproducibility of these results necessitates more samples or future magnetic freeze casting work with larger magnetized particles to confirm general trends observed in this study.

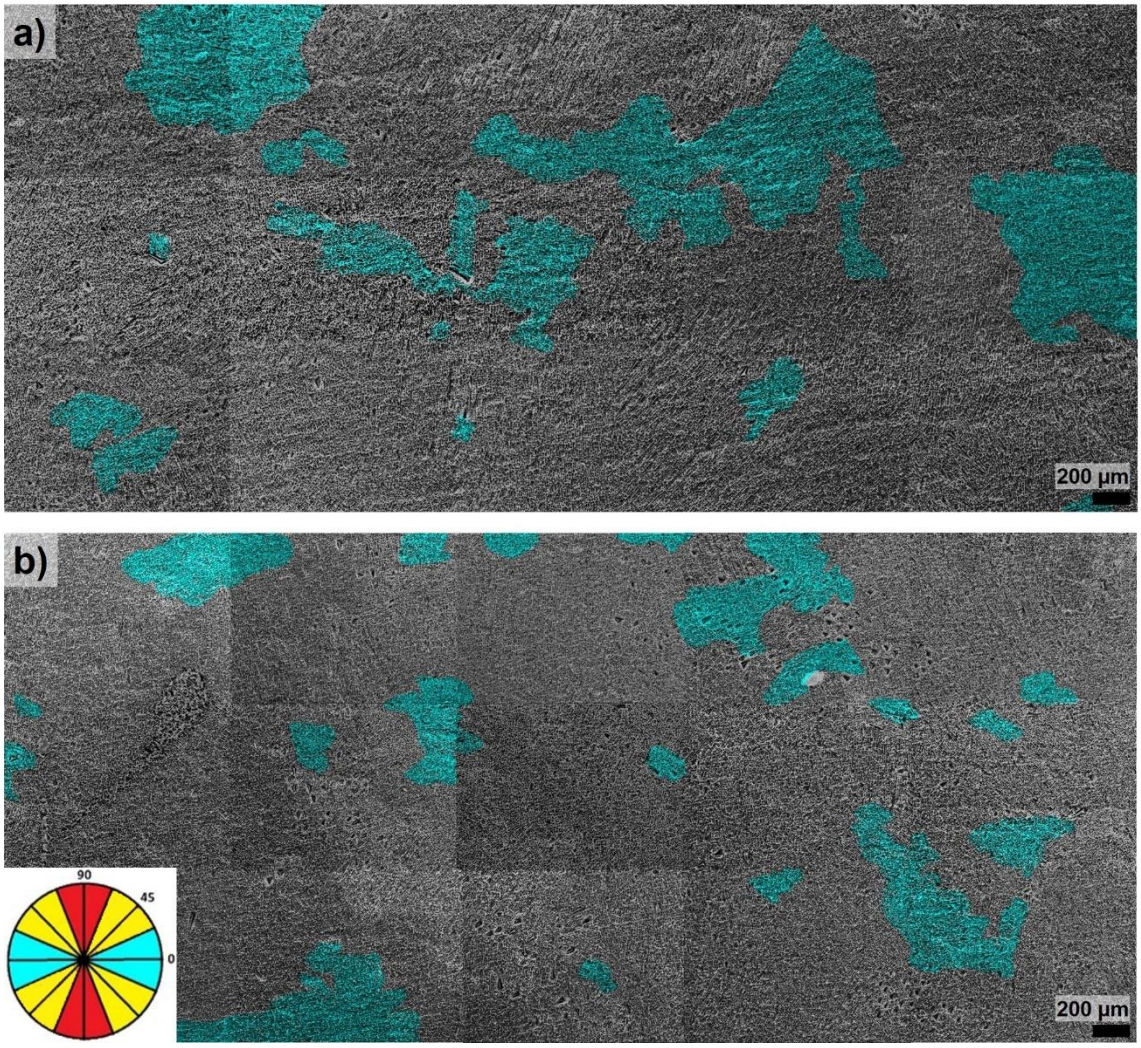

Figure 3.16: Stitched together scanning electron micrographs (6 mm x 2.7 mm) from scaffold center regions for 350 nm magnetized alumina particles after magnetic freeze casting at 75 and 150 mT. (a) More lamellar wall alignment (light blue) was evident for 350 nm alumina particles at 75 mT (≈ 20%) than at (b) 150 mT (≈ 12%). Percent lamellar wall alignment was quantified with ImageJ by dividing the summed area of the colored regions by the total stitched together area.

Different sized Al_2O_3 particles produced scaffolds with similar porosity (≈ 80-85%, Table 3.1) and lamellar wall thickness (2.3-3 µm, Table 3.1) as previous freeze casting work with ZrO_2 [69] and TiO_2 [75] that had the same processing conditions. However, the pore area for the Al_2O_3 scaffolds (35-45 μm^2, Table 3.1) was more than 20x and 5x smaller than for ZrO_2 [69] and TiO_2 [75] scaffolds, respectively, despite Al_2O_3 particles having similar sizes as ZrO_2 and TiO_2 particles. Molecular dynamic simulations indicate material

properties (e.g., surface morphology, hydrophobicity, lattice mismatch) [103] and particle surface modification with adsorbed molecules can significantly increase or decrease ice nucleation rate [104], which can help explain this discrepancy. Increased magnetic field strength (440-560 mT) can have a weak effect on physicochemical properties of water (e.g., surface tension, viscosity) [105-107], however, the lower magnetic field strength (25-150 mT) used in this study was assumed to have not affected ice nucleation or crystal growth.

Table 3.1: Porosity, pore area and lamellar wall thickness of alumina particle scaffolds freeze cast at various static magnetic fields (0, 75, 150 mT). Sample size for each condition: N = 6. All data reported are mean ± standard error (standard deviation / √N).

	Magnetic field strength (mT)	**195 nm particles**	**225 nm particles**	**350 nm particles**
Porosity (%)	0	83.74 ± 0.15	83.35 ± 0.17	82.60 ± 0.19
	75	84.77 ± 0.29	83.44 ± 0.18	82.33 ± 0.18
	150	85.29 ± 0.11	81.60 ± 0.33	81.83 ± 0.58
Pore area (μm^2)	0	37.28 ± 2.57	41.20 ± 2.56	43.33 ± 2.92
	75	37.82 ± 2.38	38.12 ± 2.17	47.29 ± 3.50
	150	34.64 ± 2.21	41.97 ± 2.69	42.54 ± 2.53
Lamellar wall thickness (µm)	0	2.32 ± 0.05	2.53 ± 0.06	2.85 ± 0.07
	75	2.31 ± 0.07	2.58 ± 0.07	2.91 ± 0.08
	150	2.34 ± 0.09	2.56 ± 0.08	3.04 ± 0.08

Freeze casting at a slower cooling ramp (-5 K/min) with a wider range of Al_2O_3 sizes (0.2-3.4 µm), Deville, et al. [108] speculated that smaller particles with higher surface area had more ice nucleation sites that led to scaffolds with larger pore area and lamellar wall thickness. For this study, a much narrower Al_2O_3 particle size range (195-350 nm) likely mitigated any large difference between number of nucleation sites, although pore area and lamellar wall thickness slightly increased for larger magnetized Al_2O_3 particles (Table 3.1). Altered ice nucleation rates in other freeze casting systems using different solidification rates, materials, particle sizes and unmodified surfaces can further complicate comparison of measured scaffold properties. Additional experimental work on heterogeneous ice nucleation is certainly needed to correlate empirical results with

fundamental understanding of physiochemical processes from molecular dynamics simulations [103].

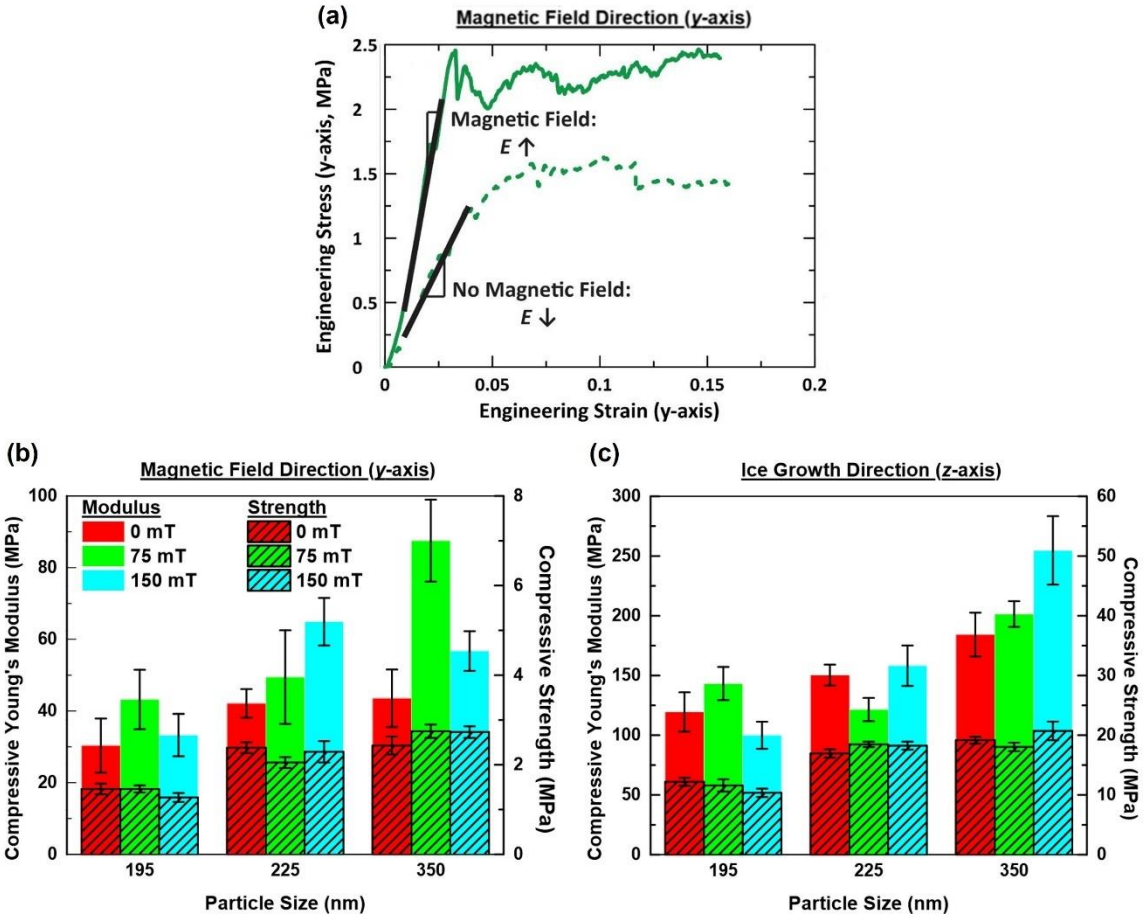

Figure 3.17: Comparison of compressive mechanical properties with stress-strain curve, modulus and strength values for porous scaffolds of magnetized alumina particles prepared by magnetic freeze casting. (a) A representative stress–strain curve for 350 nm particles made with no magnetic field (dotted line) and static magnetic field of 75 mT (solid line). Compressive Young's modulus and ultimate strength as a function of particle size and magnetic field strength in the (b) magnetic field (y-axis) and (c) ice growth direction (z-axis). Data points are the mean of N = 6 measurements with error bars representing ± standard error (standard deviation / √N).

Magnetic freeze casting used with slurries of 10 vol% ZrO_2 mixed with 50 nm Fe_3O_4 particles showed mineral bridge alignment and thickness increased as Fe_3O_4 content and transverse magnetic field strength increased [4]. In those slurry mixtures, larger Fe_3O_4 particles with ferromagnetic properties ($\Gamma >> 1$) led to particle chaining of Fe_3O_4 concentrated within aligned and thickened mineral bridges along the transverse magnetic

field axis. In the present study, slight thickening of the lamellar walls occurred at varying magnetic field strength for 350 nm particles only (Table 3.1) and resulted in mostly uniform microstructures compared with previous work.

3.2.5 Mechanical Properties

Freeze cast scaffold porosity from a slurry of 10 vol% Al_2O_3 was consistent across all samples (≈ 80-85%), so direct comparison of mechanical properties could be correlated between particle sizes. At no applied magnetic field, pore area and lamellar wall thickness increased with particle size (Table 3.1). Figure 3.17a shows a representative *y*-axis stress-strain curve for 350 nm scaffolds prepared with and without an applied magnetic field. The large uneven plateau region on the plot is typical of porous materials, where individual walls are fracturing over a large strain range. It is clear that Young's modulus (*E*) and ultimate compressive strength (UCS) are larger with an applied magnetic field, corroborating the results of Porter, et al. [1] who found the same effect in TiO_2 scaffolds.

Figure 3.17b,c summarizes *E* and UCS in the magnetic field, *y*-axis, and ice growth, *z*-axis, directions as a function of particle size and magnetic field strength. In Figure 3.17b, *E* and UCS in the *y*-axis ranged between ≈ 30-90 MPa and ≈ 1.2-2.8 MPa, respectively. In general, both *E* and UCS increased with increasing particle size, which is attributable to scaffolds with larger particles having thicker lamellar walls. For 225 nm scaffolds, *E* increased by ≈ 50% at 150 mT compared to 0 mT (Figure 3.17b), while *E* did not increase at any magnetic field strength for 195 nm scaffolds. The 350 nm scaffolds prepared at 75 mT had the highest *E* increase by ≈ 100% compared to 0 mT (Figure 3.17b), which correlated with more horizontal lamellar wall alignment observed in SEM micrographs. At 150 mT, magnetic flux lines displayed some curvature from origination at the bar magnet

poles and were not parallel throughout the sample, as found in finite element models [4]. Lower *E* value at 150 mT is attributable to curvature of the magnetic flux in the scaffold center, which caused less horizontal lamellar wall alignment. Overall, particle sizes < 350 nm show limited or no effect on transverse axis properties when a magnetic field is applied during solidification.

Figure 3.17c shows that *E* and UCS in the *z*-axis ranged between ≈ 100-260 MPa and ≈ 10-21 MPa, respectively. Both *E* and UCS values were much greater in the *z*-axis than the *y*-axis because ice templated crystal growth guided formation of aligned lamellar walls along the ice growth direction. In general, both *E* and UCS increased with particle size in the *z*-axis, again due to the increase in lamellar wall thickness (Table 3.1). For 350 nm scaffolds, more so than for scaffolds made up of smaller particles, increased magnetic field strength seemed to induce more aggregation between particles to form broader regions of aligned lamellar walls in "grains" oriented transverse to the freezing direction. Generally, scaffold compression along the *z*-axis causes crack formation and growth to occur due to local buckling of lamellar walls. However, for 350 nm scaffolds subjected to increased magnetic field strength, the compressive load was distributed more evenly by the ordered lamellar wall "grains" which had mineral bridges between parallel lamellae that prevented Euler buckling by hindering crack propagation [73, 75]. In both *y* and *z*-axes, *E* was a more reliable indicator of scaffold strengthening than UCS. Consistent trends for UCS were not evident in the *y* or *z*-axes for scaffolds of any particle size at increased magnetic field strength due to variable defects that can have a large impact during mechanical compression.

Previous work demonstrated enhancement of *E* and UCS due to lamellar wall alignment along the *y*-axis for a slurry mixture of TiO_2 mixed with ferromagnetic Fe_3O_4 (≈ 50 nm) at an applied magnetic field of 120 mT [1]. Similar improvement in the *y*-axis was evident for ZrO_2 and Fe_3O_4 at 90 mT, although mineral bridges were aligned rather than the lamellar walls [4]. The amount of magnetic material added to those TiO_2 and ZrO_2 slurries (up to 9 wt.% Fe_3O_4 particles) may have contributed to enhanced UCS values in the *y*-axis, which may help explain why similar trends were not observed in this work. From this work, surface magnetized Al_2O_3 particles subjected to a sufficient magnetic field produced observable lamellar wall alignment in the scaffold center at 75 mT for 350 nm scaffolds and 150 mT for 225 nm scaffolds. The extent of interaction energy between magnetized particles needed to induce lamellar wall alignment depended on particle size, thermodynamic variables (temperature, volume fraction) that affect aggregation and time evolution for chain formation before ice nucleation during freeze casting [91, 92, 94]. Exploration of these three factors will continue with further magnetic freeze casting experimental work.

The schematic diagrams in Figure 3.18 summarize how particle chaining (orange lines) can lead to lamellar wall alignment in the scaffold center (dotted box), or not (dotted gray box), for each magnetized particle size at varying magnetic field strengths. For 225 nm particles, greater magnetic field strength (150 mT) led to more interaction energy between particles that overcame thermal agitation force within the slurry and partially aligned lamellar walls within the scaffold center. For 350 nm particles with greater Γ than 195 or 225 nm particles (Figure 3.14), more horizontal lamellar wall alignment occurred

along the *y*-axis in the scaffold center at 75 mT compared with too strong of a magnetic field (150 mT) that produced angled lamellar wall alignment.

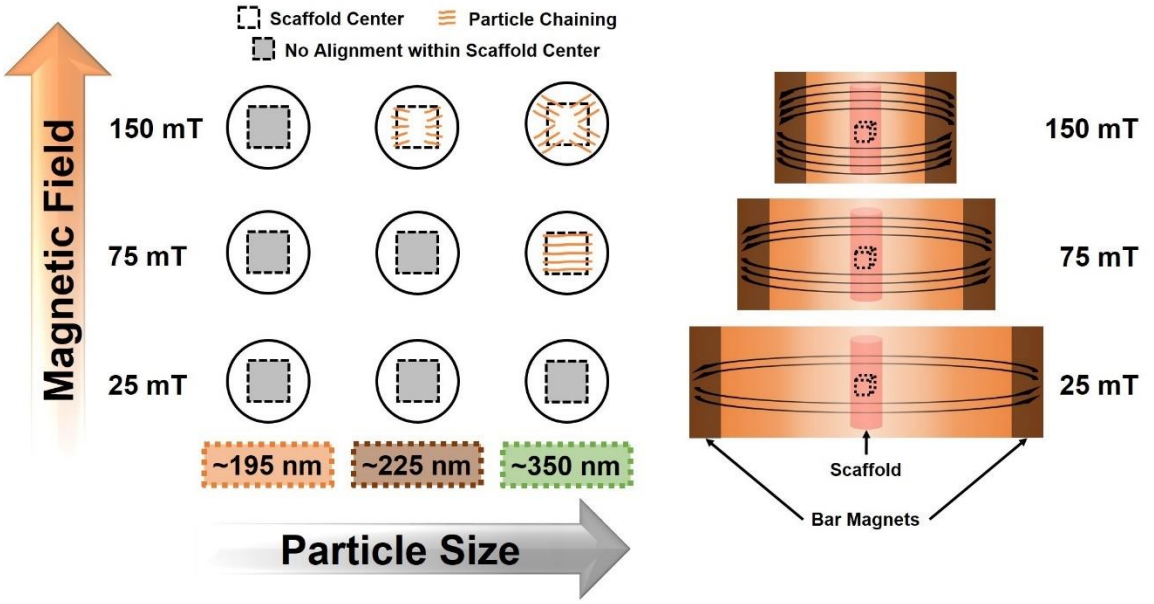

Figure 3.18: Lamellar wall alignment within the scaffold center as a function of magnetic field strength and magnetized particle size. The schematic indicates the extent of particle chaining (orange line) leading to lamellar wall alignment in the scaffold center (dotted box) for each magnetized alumina particle size at varying magnetic field strength. Lower magnetic field strength produced no lamellar wall alignment within the scaffold center for smaller particles (dotted gray box). A greater degree of particle chaining for larger particles led to more lamellar wall alignment, although a stronger magnetic field caused that alignment to be angled near the magnet poles instead of along the horizontal axis within the scaffold center.

3.2.6 Conclusions

Freeze casting was carried out for the first time with varying surface magnetized alumina (Al_2O_3) particle sizes (195, 225 and 350 nm) and magnetic fields (0, 75 and 150 mT) applied transverse to the ice growth direction. This new method provides an avenue for examination of physical processes that affected particle aggregation leading to lamellar wall alignment in sintered porous scaffolds. Particle size measurement by the dynamic light scattering (DLS) technique combined with magnetometer data indicated larger magnetized particles had greater interaction energy that could lead to more lamellar wall alignment. Scanning electron microscopy characterization of the sintered scaffold center indicated the

most horizontal lamellar wall alignment for 350 nm particles at 75 mT, while both compressive Young's modulus (≈ 100%) and strength (≈ 20%) also increased in the magnetic field direction. Scaffolds made of larger particles produced more horizontal lamellar wall alignment at weaker magnetic field strength with thicker lamellar walls that increased Young's modulus and strength. Previous magnetic freeze casting work that used a heterogeneous slurry of magnetite particles mixed with oxide ceramic particles to align lamellar walls and mineral bridges can be extended with this work to include any surface magnetized materials.

3.3 Magnetic Freeze Casting with Magnetized Alumina Particles and Platelets

3.3.1 Introduction

Ordered assembly of isotropic and anisotropic ceramic morphologies into macrostructures with enhanced electrical, piezoelectric and mechanical properties is a significant materials science challenge. Alignment of crystallographic orientation along a preferred axis can be initiated by hot forging [109, 110], strong magnetic field [43-51, 111, 112], electrophoretic deposition [113, 114] and various forms of casting (tape, gel, slip and centrifugal) [115-125]. Carisey, et al. [126, 127] were first to produce monolithic alumina with improved strength and resistance to crack propagation using a tape casting method that controlled the texture of 5-10 wt% alumina platelet seeds within a matrix of alumina particles and organic binders. Shear forces from the straight edge of the sweeping doctor blade oriented the platelets in a preferred alignment before templated grain growth (TGG) occurred during sintering to improve the mechanical properties. When used within polymer composites, alumina platelets can also be aligned to resemble strengthened, bioinspired

nacre-like brick-and-mortar microstructures by tape casting [128] or low magnetic field [129] following surface magnetization [5].

Macroporous ceramics (porosity > 50%) are useful for applications able to withstand a wide range of extreme environments, both thermal and chemical [130]. Rapid advancements in development of polymer-derived ceramic materials have enabled designs with complex porosity and shapes via manufacturing methods such as soft lithography micromolding [131], stereolithography and self-propagating photopolymer waveguide technology [132]. Potential uses for these structural ceramics with ordered porosity include size selective catalysis and ceramic sandwich panels for aerospace vehicles. Ceramic water filters [133], made with natural materials (clay, water, sawdust, flour, etc.) using 19th century manufacturing methods, have micron sized pores to capture bacteria associated with water borne diseases [134]. Impregnation of the pores with colloidal silver was shown to further deactivate and remove up to 100% of applied bacteria in a controlled study [135], although the randomly oriented porosity often makes the filters susceptible to breakage during transportation or use. Nanoporous anodic aluminum oxide (AAO) [136] has similar biofiltration applications [137], however, the thin ceramic membranes are not considered robust materials.

Porous ceramic scaffolds strengthened by uniaxial aligned pores can be fabricated by a physical process known as freeze casting [14, 64, 65, 69]. As shown in Figure 3.19a, a slurry consisting of a solid phase (e.g., ceramic particles) and freezing agent (e.g., water) uses ice crystal growth to separate particles into lamellae aligned along the freezing direction (z-axis) and oriented randomly along transverse directions (x, y-axes). The frozen block is freeze dried and sintered to strengthen the scaffold structure through densification.

A temperature gradient applied to the freezing stage [81-84] along the *y*-axis can induce long range transverse lamellae alignment that enhances scaffold mechanical properties. Both alumina particles [78-80, 138] and platelets [67, 68, 139] have been used for freeze casting without a magnetic field. Freeze casting with particle and platelet mixtures incorporated intralamella and interlamella platelets to stiffen and strengthen scaffolds along the *z*-axis [96, 140]. For temperature gradient freeze casting, an alumina particle and platelet mixture, plus a small amount of silica-calcia as liquid phase interface, contributed to TGG [81]. Significantly enhanced scaffold mechanical properties were obtained for slurries with a ≈ 9:1 particle to platelet ratio [82, 96], while peak stress values occurred at a higher particle to platelet ratio (19:1) before dissipating when component disparity became too great (39:1) [140].

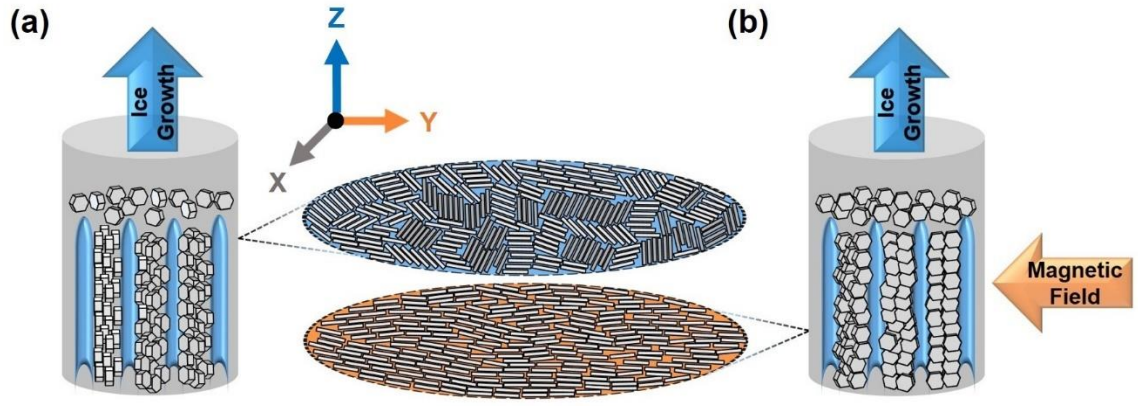

Figure 3.19: Schematics for platelets undergoing freeze casting (left, blue oval) and with an applied magnetic field (right, orange oval). (a) Volumetric expansion of ice within a confined mold aligns alumina platelets by shear along the ice growth direction (z-axis). (b) An applied magnetic field aligns magnetized platelets prior to ice solidification along an additional transverse direction (y-axis).

A transverse static (along the *y*-axis) or rotating (about the *z*-axis) magnetic field applied to slurries of ceramic particles mixed with ferromagnetic magnetite during freeze casting can lead to enhanced lamellae alignment [1, 3, 4]. For a slurry mixture of paramagnetic titania and ferromagnetic magnetite subjected to a static field (≈ 120 mT),

interparticle interactions resulted in lamellae alignment and mechanically enhanced scaffolds along the *y*-axis [1]. Superparamagnetic magnetite (≈ 10 nm), by itself [91] undergoes chain formation in water only when magnetic interaction energy for a sufficient volume fraction exceeds thermal energy [92, 94]. Similarly, a transverse magnetic field applied during freeze casting to a slurry of surface magnetized alumina can lead to aggregation within aligned lamellae along the *y*-axis (Figure 3.19b). Larger surface magnetized alumina particles (≈ 350 nm) demonstrated more lamellae alignment during magnetic freeze casting than did smaller alumina (≈ 195, 225 nm) and scaffolds had twice the stiffness along the *y*-axis (≈ 75 mT) compared with no magnetic field [141].

This work investigates the use of magnetic freeze casting to construct multi-axis stiffened porous scaffolds with surface magnetized alumina particles and platelets. A wide range of alumina particle to platelet ratios (0:1, 1:3, 1:1, 3:1, 7:1, 1:0) was used to explore how dissimilar morphologies can aggregate in a mechanically synergistic manner during freeze casting with a transverse applied magnetic field along the *y*-axis. Superparamagnetic magnetite nanoparticles adsorbed onto larger alumina imparts magnetization at the nanoscale, which facilitates control over assembly at the microscale. Examination of spider silk, nacre and bone reveals that the microstructure and hierarchical architecture of these natural materials are responsible for the extraordinary mechanical properties [60, 142]. Fabrication of bioinspired structural materials by magnetic freeze casting can further correlate with well-established engineering designs observed in light-frame construction of houses made with wood studs and sheathing. Structural materials of the future may yet incorporate a combination of successful design strategies observed among natural wonders as well as the byproducts of manmade civilization that exist all around us.

3.3.2 Materials and Methods

3.3.2.1 Particle and Platelet Surface Magnetization

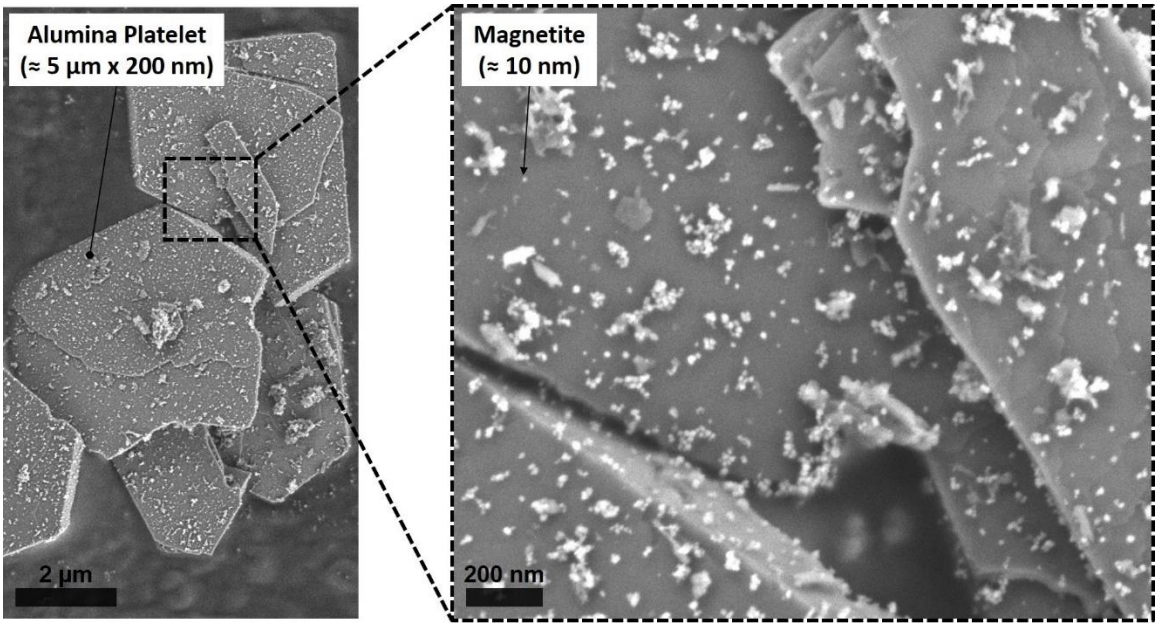

Figure 3.20: Scanning electron micrographs of magnetized alumina platelets (≈ 5 µm diameter, ≈ 200 nm thickness) show magnetite nanoparticles (≈ 10 nm) adhered on the surface.

α-Alumina particles (≈ 350 nm measured by dynamic light scattering technique (DLS) [97-99, 141, 143-146]; CR6, Baikowski, Malakoff, TX, USA) and platelets (≈ 5 µm diameter, ≈ 200 nm thickness estimated by supplier; YFA5025, Serath, Kinsei Matec Co., Ltd., Osaka, Japan) with bulk density of 3960 kg/m^3 [96] were surface magnetized following a previously described protocol [141]. Selected particle and platelet sizes had larger measured magnetic moments relative to smaller particles (≈ 195, 225 nm) and platelets (≈ 600 nm diameter, ≈ 60 nm thickness; ≈ 2 µm diameter, 40 nm thickness) considered in preliminary work not included here. 2.5 g of alumina particles or platelets were stirred in 75 mL distilled water. Dropwise addition of 100 µL anionic ferrofluid (EMG-705, Ferrotec, Bedford, NH, USA), diluted in 5 mL distilled water, to the stirring slurry changed the white alumina particles or platelets to a light brown color. The

surrounding solution became clear after stirring for 12 hours. Surface magnetized alumina (platelets in Figure 3.20, particles in Figure 3.7c) was then rinsed with distilled water, vacuum filtered and dried for 12 hours at 100˚C before magnetic freeze casting.

3.3.2.2 Magnetic Materials Characterization

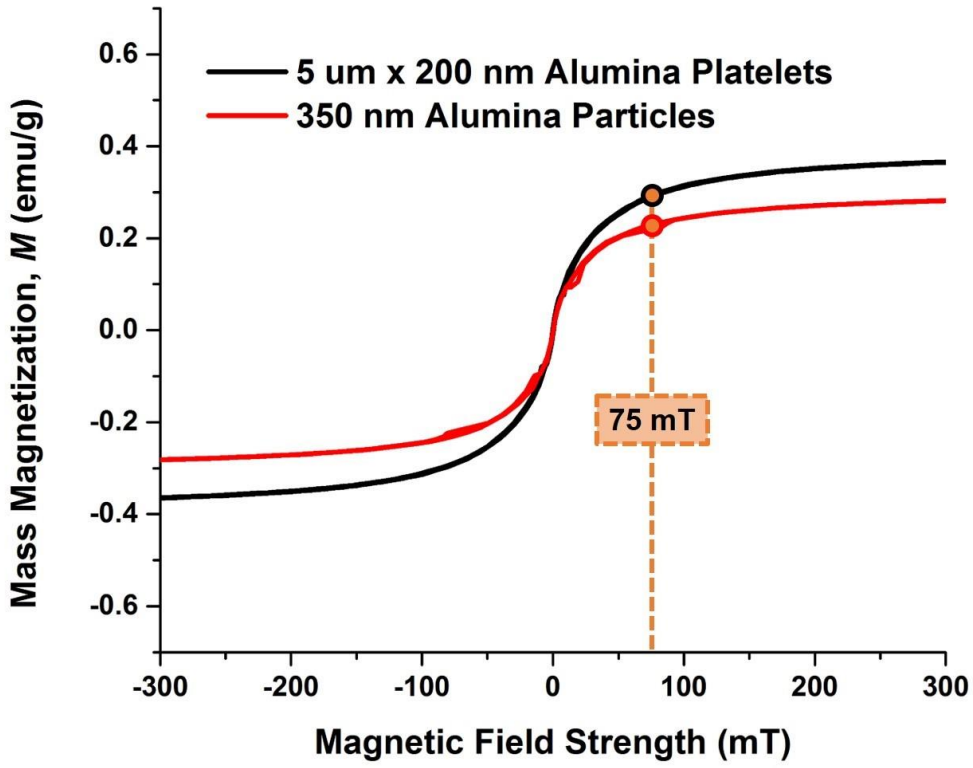

Figure 3.21: Comparison of mass magnetization, M, values determined with Eqn. 4 using magnetometer measurements for surface magnetized alumina particles (red) and platelets (black) subjected to a sweeping magnetic field, H (units converted to mT). Values for M at the applied magnetic field strength (75 mT) during magnetic freeze casting are indicated.

Magnetized alumina particles or platelets (≈ 15-30 mg) were characterized with a vibrating sample magnetometer (VSM, VersaLab, Quantum Design International, San Diego, CA, USA). Mass magnetization (*M*, emu/g) in response to a sweeping magnetic field (0-300 mT, Figure 3.21), as well as magnetic moment (*m*, Am2) calculated from

measured particle volume (v) by DLS (particles) or supplier estimated volume (platelets) were determined using Eqns. 4 and 5. The methodology for calculating the number of magnetite nanoparticles per alumina particle or platelet, as well as the corresponding magnetization value of an individual magnetized particle or platelet is detailed (Table 3.2).

3.3.2.3 Magnetized Slurry Preparation

Slurries of magnetized alumina particles, platelets or combined particles and platelets (10 vol%, particle to platelet ratios of 0:1, 1:3, 1:1, 3:1, 7:1, 1:0) were prepared (by weight alumina) with organic binders, 1 wt% polyvinyl alcohol (100,000 g/mol molecular weight (MW), Alfa Aesar, Ward Hill, MA, USA) and 1 wt% polyethylene glycol (PEG, 10,000 g/mol MW, Alfa Aesar, Ward Hill, MA, USA), and 1 wt% anionic dispersant (Darvan 811, R. T. Vanderbilt Company, Inc., Norwalk, CT, USA). Alumina grinding media was added and the slurry was ball milled for 24 hours.

3.3.2.4 Magnetic Freeze Casting

A vise grip (Panavise, Reno, NV) with ≈ 420 mT bar magnets (N52 grade, K&J Magnetics, Inc. Pipersville, PA, USA) attached to either end was placed 7 cm apart along the transverse y-axis using a previously described setup [141]. Magnetic field strength at the midpoint between the bar magnets surrounding the polyvinyl chloride (PVC) mold containing the slurry was measured with a Gauss meter to be ≈ 75 mT. Freeze casting with a magnetized alumina slurry was conducted either with a magnetic field (≈ 75 mT) along the *y*-axis or with no magnetic field. A grooved edge filed on the inside wall of the PVC mold was aligned with the bar magnets to provide a visual indicator for the applied magnetic field along the *y*-axis in sintered samples.

Table 3.2: Calculation methodology for determining the number of magnetite nanoparticles per alumina particle or platelet and its corresponding magnetization value.

(*A*)	Mass (g) of an individual alumina particle or platelet calculated with volume (cm^3) from DLS measured average particle size (350 nm diameter with assumed spherical shape) or supplier provided platelet dimensions (5 μm diameter, 200 nm thickness with assumed cylindrical shape) and α-alumina density (3.96 g/cm^3) $Individual\ Alumina\ Particle\ or\ Platelet\ Mass\ (g) = Volume\ (cm^3) \times Density\ (\frac{g}{cm^3})$
(*B*)	$Bulk\ Alumina\ Particle\ or\ Platelet\ Mass\ per\ Magnetization\ Batch = 2.5\ g$
(*C*)	$Number\ of\ Alumina\ Particles\ or\ Platelets\ per\ 2.5\ g\ Magnetization\ Batch = \frac{2.5\ g}{(A)\ value}$
(*D*)	Mass (g) of an individual magnetite particle calculated with volume (cm^3) from supplier provided particle size (10 nm with assumed spherical shape) and magnetite density (5.15 g/cm^3) $Individual\ Magnetite\ Particle\ Mass\ (g) = Volume\ (cm^3) \times Density\ (\frac{g}{cm^3})$
(*E*)	$Ferrofluid\ Volume\ (cm^3)\ to\ Magnetize\ 2.5\ g\ Alumina = 0.1\ cm^3$
(*F*)	Volume (cm^3) of magnetite in ferrofluid (0.1 cm^3) used to magnetize a bulk alumina particle or platelet batch (2.5 g) based on supplier provided information (1-4 vol% magnetite in ferrofluid, assume upper limit amount of 4 vol% magnetite) $Magnetite\ Volume\ (cm^3)\ in\ 4\ vol\%\ Ferrofluid\ (0.1\ cm^3) = 0.04 \times 0.1\ cm^3 = 0.004\ cm^3$
(*G*)	$Magnetite\ Mass\ (g)\ in\ 4\ vol\%\ Ferrofluid\ (0.1\ cm^3) = 0.004\ cm^3 \times Density\ (\frac{g}{cm^3})$
(*H*)	$Number\ of\ Magnetite\ Particles\ per\ Surface\ Magnetization\ Batch = \frac{(G)\ value}{(D)\ value}$
(*I*)	$Number\ of\ Magnetite\ Particles\ per\ Alumina\ Particle\ or\ Platelet = \frac{(H)\ value}{(C)\ value}$
(*J*)	$Individual\ Alumina\ Particle\ or\ Platelet\ with\ Adsorbed\ Magnetite\ Mass\ (g) = [(A)\ value] + \{[(D)\ value] \times [(I)\ value]\}$
(*K*)	$Mass\ Magnetization\ of\ Magnetized\ Alumina\ Particles\ or\ Platelets\ \left(\frac{emu}{g}\right) = 0.220\ \left(\frac{emu}{g}\right)\ for\ Alumina\ Particles\ and\ 0.290\ \left(\frac{emu}{g}\right)\ for\ Alumina\ Platelets\ at\ 75\ mT$
(*L*)	$Magnetization\ of\ Individual\ Magnetized\ Alumina\ Particle\ or\ Platelet\ (emu) = [(J)\ value] \times [(K)\ value]\ at\ 75\ mT$

After ball milling, the magnetized alumina slurry was degassed for 15 minutes by vacuum before 5 mL was poured into a PVC mold and centered underneath the magnetic field apparatus. Freezing occurred from the bottom upward using a previously described freeze casting device [1] and freezing front velocity (FFV) was estimated as the total frozen scaffold height (≈ 45 mm) divided by the total freezing time (≈ 1,800 s) to get FFV ≈ 25 μm/s [96, 138, 140]. Frozen samples were lyophilized with a bench-top freeze dryer (Labconco, Kansas City, MO, USA) at -50 °C and 3.5 x 10^{-6} Pa for 48 hours to sublime ice

crystals and leave behind fragile ‘green body’ scaffolds made up of alumina particles, platelets or both that were held together by polymer binders. Samples were sintered in an open air furnace for 3 hours at 1500°C with heating and cooling rates of 2°C/min following a previously reported procedure [1].

3.3.2.5 Mechanical Characterization

Six scaffolds were prepared for each condition with alumina particle to platelet ratio (0:1, 1:3, 1:1, 3:1, 7:1, 1:0) and magnetic field strength (0, 75 mT) as variables. Compression testing of the scaffolds was performed on a 3342 Instron materials testing machine (Instron, Norwood, MA) with a 500 N static load cell at a constant crosshead velocity of 0.005 mm/s following previous procedures [1, 4, 75, 76, 141]. Three samples (≈ 5 mm^3 cubes) cut from each scaffold center, where uniform porosity was evident, were compressed in the transverse (*x*-axis), magnetic field (*y*-axis) and ice growth (*z*-axis) directions for each particle to platelet ratio condition (1:3, 1:1, 3:1, 7:1), while two samples were compressed in the *y*-axis and *z*-axis for the all particles (1:0) and all platelets (0:1) conditions. Ultimate compressive strength and Young’s modulus were determined from the maximum stress and linear slope of the stress–strain curves, respectively.

3.3.2.6 Scanning Electron Microscopy Characterization

Two of the six sintered scaffolds for each condition were sectioned at midpoint height, mounted to a stage and coated with colloidal graphite along the bottom and side walls. Iridium was sputter coated (EMITech K575X, Quorum Technologies Ltd., West Sussex, UK) for 15 s at 85 mA onto the top. Scanning electron microscopy (SEM) micrographs at 10 kV (spot size 3 nm) from a Philips XL30 field emission environmental scanning electron microscope (FEI-XL30, FEI Company, Hillsboro, OR) were stitched

together along overlapping edges to assess long range lamellar wall alignment in the scaffold center. Lamellar wall regions were shaded different colors to indicate horizontal alignment (light blue, 22.5° offset from the *y*-axis), angled alignment (yellow, 22.5° to 67.5° offset from the *y*-axis) and no alignment (red, 67.5° to 90° offset from the *y*-axis). ImageJ software (National Institutes of Health, Bethesda, MD, USA) was used to quantify lamellar wall horizontal alignment, for the overlapped SEM micrographs area (6000 µm x 2700 µm) at 100x magnification within the scaffold center region used for mechanical testing, by dividing the light blue shaded scaffold area by the total scaffold area.

Scaffold morphology was further characterized using ImageJ to analyze 500x magnification micrographs from the center region of each condition. The number of bridges between lamellar walls per unit area (bridge density, ρ_b) and the average wavelength (λ) from measurements (N = 40) of adjacent lamellae top surfaces were input into Eqn. 6 to obtain a dimensionless parameter (m_s) for describing scaffold morphology as either lamellar ($m_s > 5$), dendritic ($1 < m_s < 5$) or isotropic ($m_s < 1$) [147] (Figure 3.22).

$$m_s = (1/\rho_b)/(\lambda^2) \quad (6)$$

3.3.3 Magnetic Response of Magnetized Alumina Particles and Platelets

Magnetized alumina particles and platelets subjected to a sweeping magnetic field, *H*, and plotted versus *M* (Eqn. 4, Figure 3.21) had an absence of hysteresis and magnetization at $H = 0$ on the *M*-*H* curve. This result confirmed the magnetized particles and platelets "responded" to a sweeping magnetic field in a superparamagnetic manner (Figure 3.11) with less susceptibility (maximum slope) and saturation (maximum *M* value) than superparamagnetic magnetite nanoparticles alone [100], but with similar magnetic properties as composites with superparamagnetic magnetite cores [101]. DLS

measurement after ball milling indicated ≈ 350 nm average alumina particle size [141], while supplier estimates for alumina platelets (≈ 5 µm diameter, ≈ 200 nm thickness) were used due to size complexity for measurement of non-spherical platelet shapes [148, 149]. At 75 mT, calculated magnetic moment, *m*, (Eqn. 5) for platelets was more than 200x greater than for particles due in large part to the platelets having ≈ 175x greater volume.

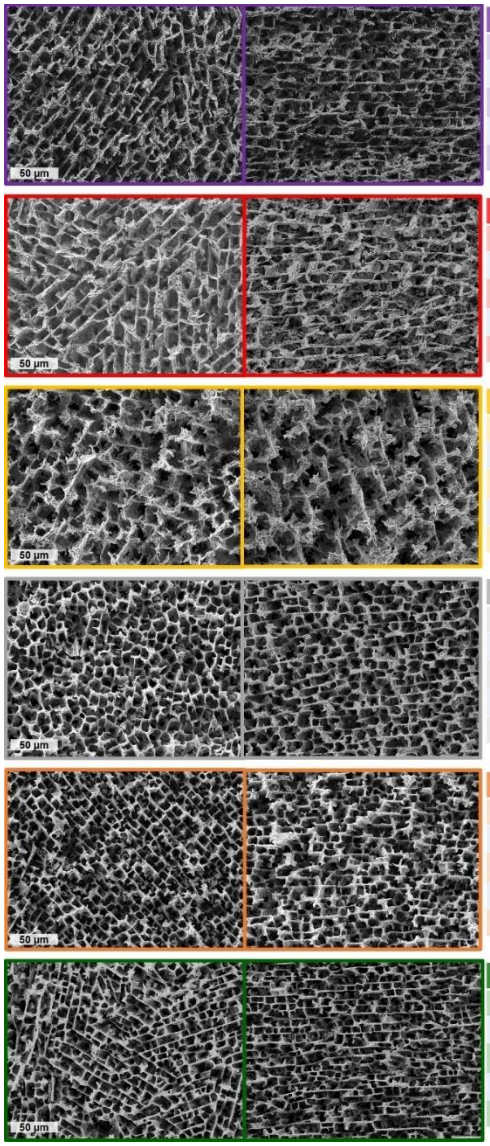

100% Platelets	0 mT	75 mT
Bridge #	225	275
Area (µm²)	46180	45993
ρ_b (Bridge #/Area)	4.87×10^{-3}	5.98×10^{-3}
λ (µm)	10.36	10.56
m	1.91	1.50

75% Platelets	0 mT	75 mT
Bridge #	185	210
Area (µm²)	46064	46041
ρ_b (Bridge #/Area)	4.02×10^{-3}	4.56×10^{-3}
λ (µm)	10.94	10.01
m	2.08	2.18

50% Platelets	0 mT	75 mT
Bridge #	N/A	N/A
Area (µm²)		
ρ_b (Bridge #/Area)		
λ (µm)		
m		

25% Platelets	0 mT	75 mT
Bridge #	360	310
Area (µm²)	46158	46346
ρ_b (Bridge #/Area)	7.80×10^{-3}	6.69×10^{-3}
λ (µm)	9.23	9.94
m	1.51	1.51

12.5% Platelets	0 mT	75 mT
Bridge #	400	362
Area (µm²)	45971	46230
ρ_b (Bridge #/Area)	8.70×10^{-3}	7.83×10^{-3}
λ (µm)	8.12	9.29
m	1.74	1.48

0% Platelets	0 mT	75 mT
Bridge #	332	403
Area (µm²)	46252	46301
ρ_b (Bridge #/Area)	7.18×10^{-3}	8.70×10^{-3}
λ (µm)	8.87	8.04
m	1.77	1.78

Figure 3.22: Quantification of lamella bridge number, bridge density (ρ_b) and wavelength (λ) for calculation of the morphological parameter (m_s) with addition of platelets (100, 75, 50, 25, 12.5 and 0%) and application of magnetic field (0, 75 mT).

Since α-alumina particles and platelets with equal weight (2.5 g) and density (3.96 g/cm^3) were magnetized with an equal volume of ferrofluid (0.1 mL), the amount of surface adsorbed magnetite per alumina particle or platelet was estimated based on assumptions for spherical magnetite nanoparticle size (≈ 10 nm) and fraction in ferrofluid (4 vol%), as detailed in Table 3.2. Overall, each alumina particle and platelet had ≈ 270 and ≈ 47,500 adsorbed magnetite nanoparticles, respectively. Values of *M* at 75 mT multiplied by the mass of an individual particle or platelet with adsorbed magnetite yielded 1.97 x 10^{-14} and 4.54 x 10^{-12} emu magnetization values for surface magnetized particles and platelets, respectively. Magnetization per platelet was ≈ 230x greater than per particle due to the larger platelet size and aspect ratio (≈ 25). Although Faraudo, et al. [94] described chain assembly for only spherical superparamagnetic magnetite nanoparticles or composite particles with superparamagnetic cores, aggregation of magnetized particles and platelets in water should also occur at a sufficient magnetic field strength and volume fraction when the magnetic interaction energy exceeds the thermal energy. Larger platelets have a much greater magnetic moment than smaller particles based on calculations from VSM data, so magnetic freeze casting with platelets should lead to more aggregation for enhanced lamellar wall alignment.

3.3.4 Lamellar Wall Alignment

1D chain formation of magnetite nanoclusters subjected to an applied magnetic field at room temperature in aqueous solution has been described [102]. During magnetic freeze casting, magnetized alumina particles (≈ 350 nm) aggregated into ≈ 20% aligned lamellar walls along the *y*-axis at 75 mT (Figure 3.16a) for 3-4 minutes before ice nucleation occurred within the slurry [141]. Magnetic freeze cast scaffolds made up of only

larger magnetized alumina platelets, which have more than 200x greater magnetic moment per platelet than per particle, displayed more lamellar wall alignment than particle only scaffolds [141] along the *y*-axis (Figure 3.23). As expected, magnetized alumina platelets at 0 mT displayed no lamellar wall alignment, whereas alignment was evident along the *y*-axis in the scaffold center at 75 mT (Figure 3.23a). Examination of a wider view (≈ 2500 µm x ≈ 2000 µm), with colorized regions to indicate lamellar wall orientation, confirmed ≈ 98% alignment of magnetized platelets along the *y*-axis at 75 mT (Figure 3.23b).

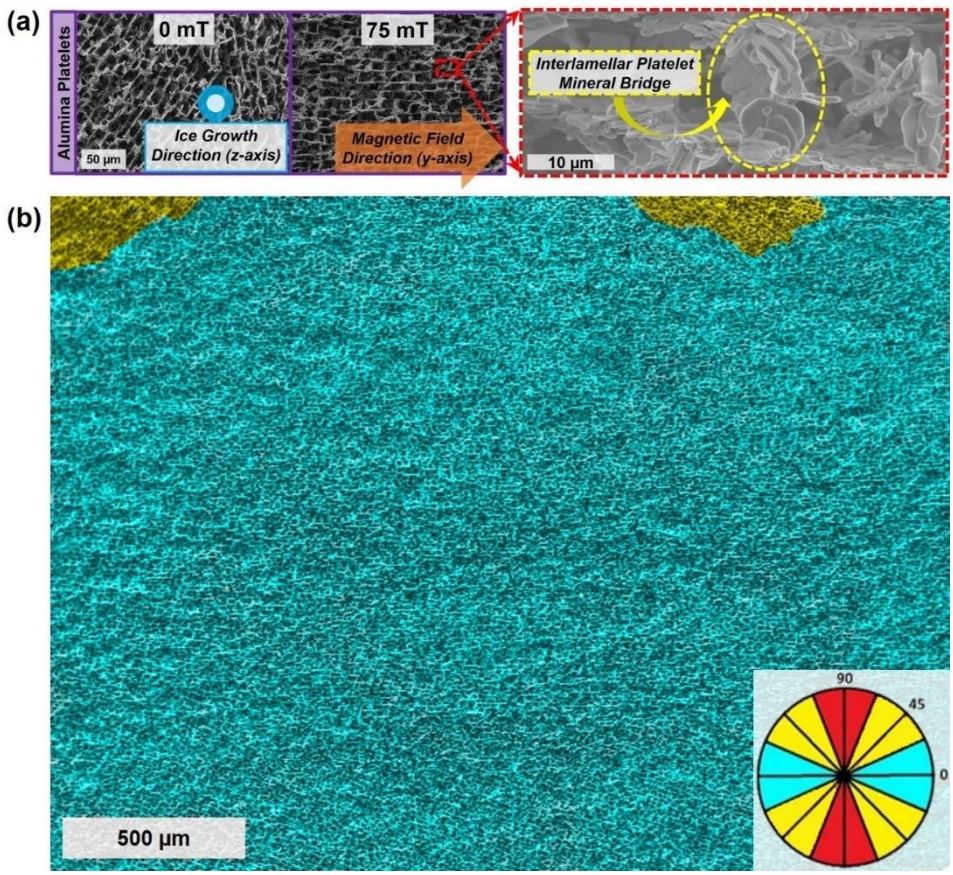

Figure 3.23: Scanning electron micrographs from scaffold center regions with and without an applied magnetic field. (a) Lamellar walls for magnetized alumina platelets (≈ 5 µm diameter, ≈ 200 nm thickness) orient randomly at 0 mT, whereas macroscopic alignment in the *y*-axis occurs within the scaffold center at 75 mT. An interlamellar platelet mineral bridge (yellow dashed circle) indicates a non-orthogonal interface with the lamellar walls. (b) Lamellar wall orientation from the scaffold center at 50x magnification (≈ 2500 µm x ≈ 2000 µm) had ≈ 98% alignment (light blue) in the *y*-axis.

Ghosh, et al. [96, 140] did similar freeze casting experiments with slurry mixtures of alumina particles and platelets at FFV ≈ 25 μm/s, but they did not surface magnetize the ceramics nor use a magnetic field to generate lamellar wall alignment of the components along the *y*-axis. They determined that 9:1 and 19:1 alumina particle (≈ 900 nm) to platelet (≈ 8 μm diameter, ≈ 400 nm thickness) slurry ratios were best for orienting intralamella and interlamella platelets in a mechanically advantageous manner along the *z*-axis in freeze cast scaffolds. Scaffolds made primarily of alumina platelets had significantly lower strength in the z-axis since slurries with more platelets in direct contact to each other had considerably less particle packing fraction and densification than ones with larger alumina particle to platelet ratios [140]. Uniaxial compression testing was conducted only in the *z*-axis, with no mention of testing or expectation of mechanical strengthening in the *y*-axis. Freeze casting with non-magnetized alumina particle and platelet slurries and no applied magnetic field most likely produced randomly oriented lamellar walls in the *y*-axis.

Since applied magnetic field strength (75 mT) induced aligned aggregation along the *y*-axis for magnetized alumina particles [141] and platelets (Figure 3.24), slurries with varying particle to platelet ratios (1:3, 1:1, 3:1, 7:1) were freeze cast at FFV ≈ 25 μm/s and compared. SEM micrographs for each platelet and particle condition showed how magnetized particles and platelets were arranged within lamellae of the sintered porous scaffolds at 0 and 75 mT (Figure 3.24). Interestingly at 75 mT, only the equivalent particle to platelet ratio (1:1) condition produced no lamellar wall alignment, whereas imbalanced particle to platelet ratios (1:3, 3:1, 7:1) each displayed long range lamellar wall alignment in the *y*-axis. This result indicates that a particle or platelet majority within the slurry must have guided aggregation into chains that formed aligned lamellar walls. The 7:1 particle to

platelet condition had the most uniform arrangement of mineral bridges that connected adjacent lamellae. Platelets with much larger size, aspect ratio and magnetic moment than smaller particles are hypothesized to align with the magnetic field and serve as a template for surrounding particle aggregation before ice nucleation occurred. More intralamellar platelets were observed along the *y*-axis within lamellar walls than interlamellar platelets oriented in the *x*-axis within mineral bridges (Figure 3.24).

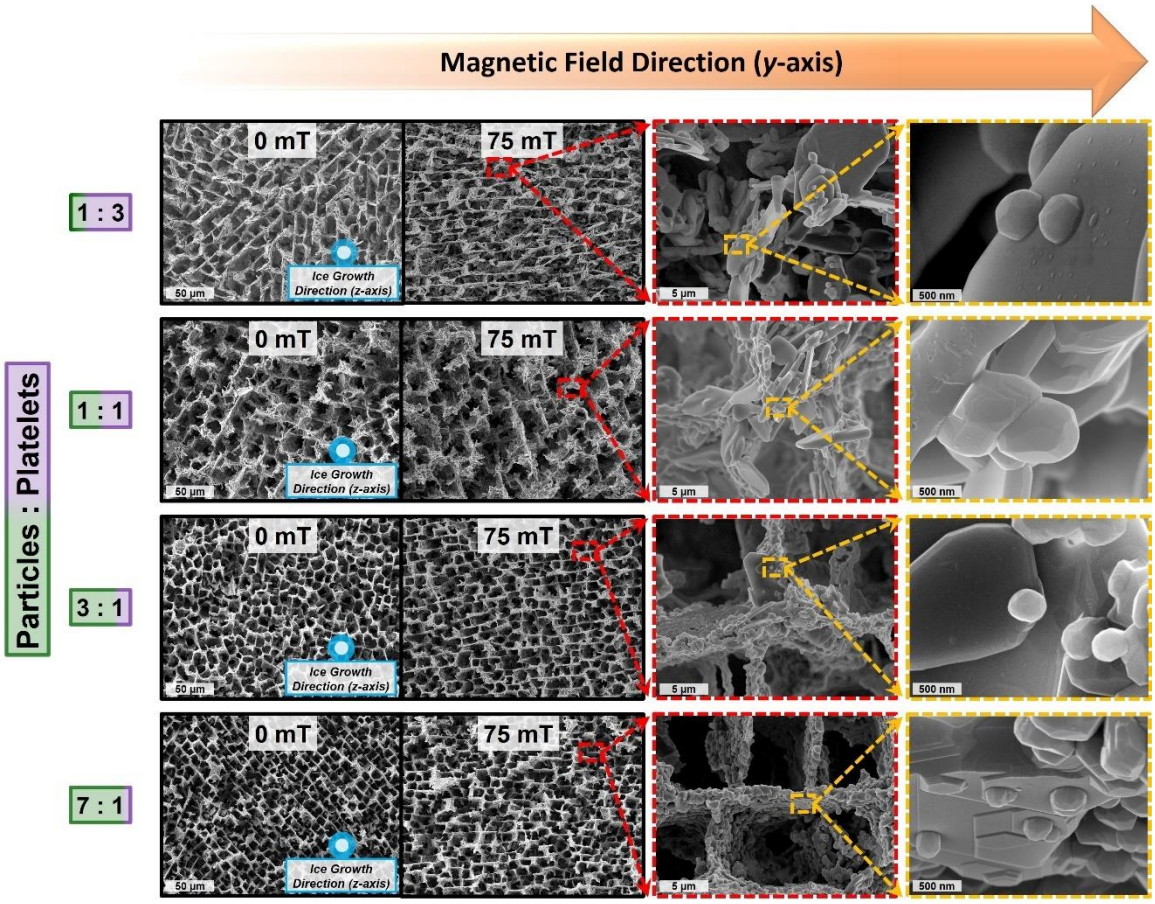

Figure 3.24: Scanning electron micrographs of scaffold center regions made from varying ratios of magnetized alumina particles (green) and platelets (purple) freeze cast at 0 or 75 mT. A heterogeneous mixture results in aligned lamellar walls when an imbalance of particles to platelets exists. Lamellar walls were disordered for an equivalent (by weight) particle and platelet slurry at 75 mT, while the most uniform alignment occurred at the same magnetic field strength with a 7:1 particle to platelet ratio.

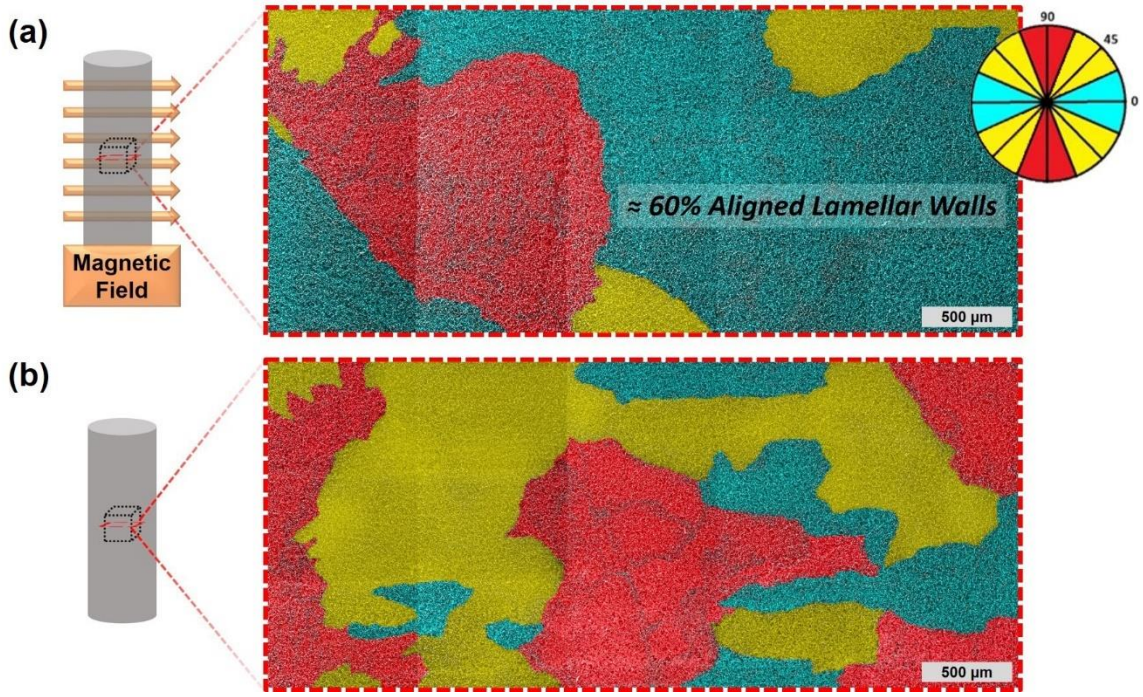

Figure 3.25: Long range lamellar wall alignment in the transverse direction (y-axis) was evident for freeze cast scaffolds at 75 mT, but not at 0 mT. (a) A 6000 µm x 2700 µm scanning electron micrograph from the scaffold center at 100x magnification was stitched together from a 7:1 particle to platelet scaffold freeze cast at 75 mT. Analysis of lamellar wall orientation with ImageJ software indicated ≈ 60% alignment (light blue). (b) Long range lamellar wall alignment was not evident in the scaffold center for a 7:1 particle to platelet scaffold freeze cast at 0 mT.

Image analysis of stitched together SEM micrographs (6000 µm x 2700 µm) from the center of a 7:1 particle to platelet scaffold indicated ≈ 60% lamellar wall alignment at 75 mT in the *y*-axis (Figure 3.25). Comparison with lamellar wall alignment in homogeneous slurries of magnetized particles (≈ 20%) [141] and platelets (≈ 98%) in Figure 3.23 indicated that a minority of platelets with much larger size and magnetic moment than a majority of particles must have helped magnetic interaction energy sufficiently exceed thermal energy to increase aggregation within *y*-axis aligned lamellar walls. Faraudo, et al. [91, 92, 94] used Langevin Dynamic (LD) simulations to predict kinetics for average superparamagnetic colloid chain length as a function of time. As predicted by LD simulations, exposure of a magnetized slurry to a magnetic field beyond

the currently implemented time of 3-4 minutes prior to ice nucleation should lead to increased chain formation with more lamellar wall alignment in the *y*-axis. Alternative freeze casting methods that use a temperature gradient [81-84] can generate lamellar wall alignment in only one transverse axis, whereas an applied magnetic field can aggregate magnetized materials along multiple axes applied during freezing for fabrication of more complex porous scaffolds.

3.3.5 Mechanical Properties

Table 3.3: Particle and platelet slurry parameters and freeze casting processing conditions for Ghosh, et al. [96, 140] versus this work.

	Ghosh, et al. [96, 140]	**Frank, et al. (this work)**
Scaffold Length (cm)	≈ 4.5	≈ 4.5
Freezing Front Velocity (FFV, µm/s)	≈ 25	≈ 25
Particle Size (nm)	≈ 900	≈ 350
Platelet Size [Diameter (µm) x Thickness (nm)]	≈ 8 x 400	≈ 5 x 200
Solid Loading (vol%)	15	10
Organic Binder (wt% of solids)	5	2
Dispersant (wt% of solids)	0.5	1
Sintering Temperature (°C)	1550	1500
Sintering Time (Hours)	4	3
Relative Density Range (%)	17-22	11-18

Mechanical properties of freeze cast alumina particle and platelet scaffolds were dependent on slurry parameters and processing conditions, which differed from Ghosh, et al. [96, 140] (Table 3.3). These differences contributed to a lower range of ρ_r values for this work with lower Young's modulus (*E*, MPa) and ultimate compressive strength (UCS, MPa) values in the *z*-axis (Table 3.4). However, the main objective for this work was to mechanically stiffen scaffolds in the *y*-axis by magnetic freeze casting with magnetized alumina particles and platelets aggregated within aligned lamellar walls. Previous magnetic freeze casting work demonstrated that aligned lamellar walls made up of ≈ 350 nm magnetized alumina particles led to mechanically stiffened scaffolds in the *y*-axis at 75 mT [141]. Magnetic freeze casting with varying ratio slurries of magnetized alumina particles

and platelets at 75 mT enabled further comparison of mechanical property differences in *x*, *y* and *z*-axes (Figure 3.26a).

Table 3.4: Relative density (RD, ρ_r), Young's modulus (E) and ultimate compressive strength (UCS) for alumina scaffolds made with different platelet to particle ratios and freeze cast with or without a static magnetic field (0, 75 mT). Sintered density (ρ^*) was determined from measured mass, measured volume dimensions (≈ 5 mm^3 cubes) and α-alumina bulk density ($\rho_s = 3.96$ g/cm^3) [96]. Compression occurred along the transverse (x-axis), magnetic field (y-axis) and ice growth (z-axis) directions. Sample size for each condition: N = 6. All data reported are mean ± standard error (standard deviation / √N).

		Particles : Platelets Ratio (by weight)					
	mT	**1:0**	**7:1**	**3:1**	**1:1**	**1:3**	**0:1**
RD (%)	0	17.5 ± 0.2	15.4 ± 0.1	11.4 ± 0.4	12.4 ± 0.2	13.0 ± 0.6	12.2 ± 0.4
$\rho_r = \rho^*/\rho_s$	75	17.9 ± 0.2	15.3 ± 0.4	12.8 ± 0.4	12.9 ± 0.2	14.3 ± 0.6	12.6 ± 0.1
***E*, MPa, *x*-axis**	0	N/A	77.4 ± 17.8	21.6 ± 8.0	16.0 ± 3.0	42.6 ± 12.2	N/A
	75	N/A	69.0 ± 19.6	33.0 ± 5.4	18.0 ± 3.3	35.8 ± 10.3	N/A
***E*, MPa, *y*-axis**	0	43.6 ± 8.0	45.0 ± 7.4	22.9 ± 1.7	17.9 ± 3.7	29.0 ± 8.0	41.7 ± 6.0
	75	87.5 ± 11.4	100.2 ± 14.6	56.2 ± 7.7	14.8 ± 2.9	58.2 ± 11.4	46.7 ± 12.3
***E*, MPa, *z*-axis**	0	184.2 ± 18.4	139.0 ± 9.9	117.3 ± 6.8	24.5 ± 5.5	70.5 ± 24.0	65.1 ± 14.8
	75	201.4 ± 10.8	121.2 ± 8.0	113.7 ± 19.5	43.9 ± 6.5	115.4 ± 28.4	68.7 ± 13.6
UCS, MPa, *x*-axis	0	N/A	2.52 ± 0.37	1.26 ± 0.28	0.74 ± 0.13	1.28 ± 0.31	N/A
	75	N/A	2.85 ± 0.43	1.82 ± 0.14	0.72 ± 0.13	1.62 ± 0.16	N/A
UCS, MPa, *y*-axis	0	2.43 ± 0.20	2.43 ± 0.30	1.38 ± 0.32	0.81 ± 0.12	2.06 ± 0.54	1.72 ± 0.23
	75	2.75 ± 0.15	3.34 ± 0.32	2.24 ± 0.08	0.81 ± 0.11	3.39 ± 0.41	1.96 ± 0.07
UCS, MPa, *z*-axis	0	19.16 ± 0.57	8.82 ± 1.60	6.95 ± 0.51	1.49 ± 0.20	7.18 ± 1.81	4.69 ± 0.55
	75	18.04 ± 0.70	9.51 ± 1.28	6.31 ± 0.29	2.32 ± 0.22	8.39 ± 1.72	4.34 ± 0.39

Although all conditions were prepared with the same freeze casting parameters, slurries with a higher particle to platelet ratio (7:1, 1:0) generally had larger ρ_r values than ones with a lower particle to platelet ratio (0:1, 1:3, 1:1, 3:1) as shown in Table 3.4. Larger ρ_r resulted in slightly larger *E* and UCS for both *z* and *y*-axes, thus specific modulus, E_r (E / ρ_r), and specific strength, UCS_r (UCS / ρ_r), values were used to account for variability between particle to platelet ratio conditions (Figure 3.26). The range of m_s values determined for each particle to platelet ratio condition ($1.4 < m_s < 2.2$) indicated dendritic

($1 < m_s < 5$), not lamellar ($m_s > 1$) or isotropic ($m_s < 1$) structures formed (Figure 3.22). There were no mechanical property trends evident for compression in the *x*-axis (Figure 3.26b). An applied magnetic field (75 mT) noticeably contributed to E_r enhancement in the *y*-axis (Figure 3.26c). Interestingly, conditions with more particles than platelets (1:0, 7:1, 3:1) had higher ρ_b values, which most likely contributed to E_r enhancement in the *z*-axis (Figure 3.26d). Further examination of each particle to platelet ratio condition revealed that an applied magnetic field did not affect E_r in the *z*-axis. However, E_r in the *z*-axis was enhanced slightly for whichever sample set (0 or 75 mT) had higher ρ_b values (Figure 3.22).

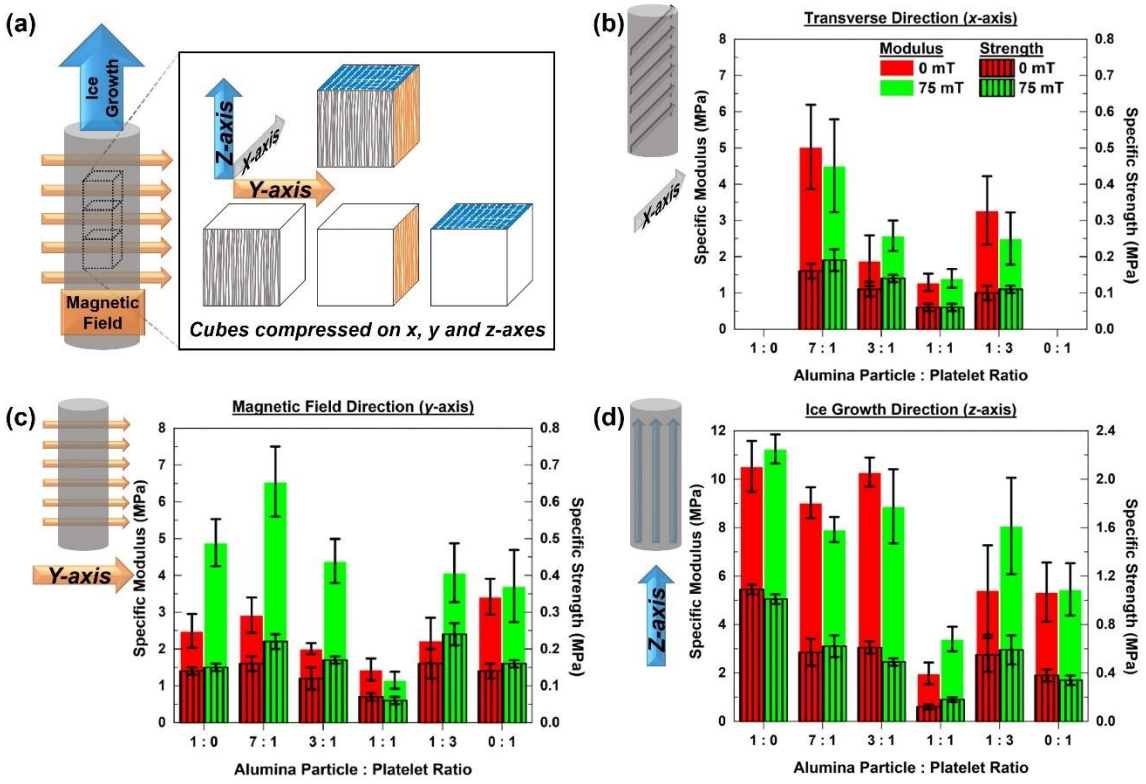

Figure 3.26: Comparison of relative density normalized compressive mechanical properties for scaffolds freeze cast at 0 or 75 mT with varying ratios of magnetized alumina particles and platelets (1:0, 7:1, 3:1, 1:1, 1:3, 0:1). (a) Individual cubes from the scaffold center are compressed in the transverse (*x*-axis, gray cube face), magnetic field (*y*-axis, orange cube face) and ice growth (*z*-axis, blue cube face) directions. Specific Young's Modulus (E_r) and ultimate compressive strength (UCS_r) values are obtained from dividing measured values (Table 3.4) by average relative density (ρ_r) for each condition in the (b) transverse (*x*-axis), (c) magnetic field (*y*-axis) (c) and ice growth (*z*-axis) directions. Data points are the mean of $N = 6$ measurements with error bars representing ± standard error (standard deviation / $\sqrt{N}$).

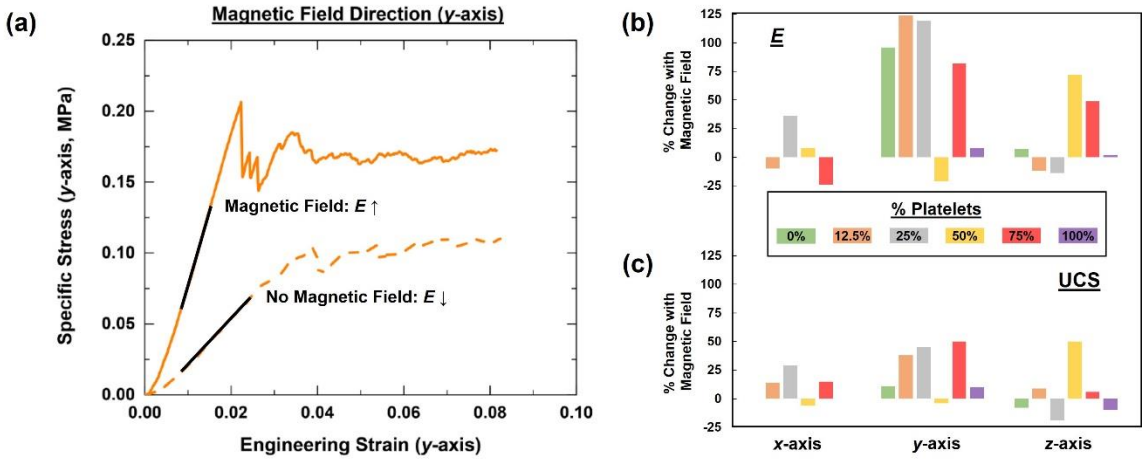

Figure 3.27: Applied magnetic field (75 mT) versus no magnetic field (0 mT) expressed as percent change in relative density normalized compressive mechanical properties for particle and platelet mixtures. (a) Representative specific stress-strain curves for 7:1 magnetized alumina particle to platelet (12.5% platelets) scaffolds freeze cast at 75 mT (solid orange line) and 0 mT (dashed orange line) indicate mechanical enhancement due to synergistic aggregation of particles and platelets. Percent change values at 75 mT versus 0 mT for (b) specific Young's Modulus (E_r) and (c) ultimate compressive strength (UCS_r) are shown in the transverse (x-axis), magnetic field (y-axis) and ice growth (z-axis) directions.

Representative stress-strain curves for 7:1 particle to platelet conditions in the *y*-axis at 0 and 75 mT are indicated in Figure 3.27a. E_r was enhanced by ≈ 125% at 75 mT compared with 0 mT (Figure 3.27b), while UCS_r in comparison was enhanced by ≈ 35% (Figure 3.27c). This result indicated magnetic field induced aggregation of particles and platelets led to synergistic mechanical stiffening up until brittle failure occurred. These 80-90% porous ceramic scaffolds must have had some lamellar walls and bridges that broke within the "elastic" regime measured as E_r up until overall failure measured as UCS_r occurred in the interconnected porous samples. Measured values for E_r in porous scaffolds, more so than UCS_r values, were more consistent and thus a better indicator of mechanical enhancement from lamellar wall alignment due to the magnetic field in the *y*-axis. Particle majority scaffolds (0, 12.5 and 25% platelets) generally had better mechanical properties than platelet majority ones (75, 100% platelets) in the *y*-axis (Figure 3.27b,c) due to a greater proportion of interface contact between spherical, rather than high aspect ratio

planar, surfaces. For the 7:1 particle to platelet condition, a small number of platelet "seeds" (12.5% platelets), with a much higher magnetic moment, may have aligned first along the magnetic field direction before the majority remainder of particles aggregated around the platelets to demonstrate a type of TGG effect. The best E_r results in the *y*-axis were found for 7:1 particle to platelet ratio scaffolds, so any higher proportion of platelet "seeds" with more lamellar wall alignment was likely offset by less interface contact between the high aspect ratio planar platelets.

For all other conditions, except the 1:1 particle to platelet ratio, E_r was also enhanced in the *y*-axis at 75 mT versus 0 mT (Figure 3.27b). The 1:1 particle to platelet ratio scaffolds had disordered lamellar walls at 75 mT in the *y*-axis (Figure 3.24) and the expectation for no mechanical property improvement was confirmed. However, the 0:1 particle to platelet condition made up of highly ordered platelets within aligned lamellar walls at 75 mT in the *y*-axis (Figure 3.23) had only ≈ 10% enhancement of E_r compared with 0 mT (Figure 3.27b). Magnetized platelet aggregation at 75 mT accounted for extensive intralamellar platelet ordering along the *y*-axis, but interlamellar platelets within mineral bridges connected between parallel lamellae were not as well ordered along the *x*-axis (Figure 3.23b). Non-orthogonal interfaces between intralamellar and interlamellar platelets, as well as lower packing fraction and densification for platelet predominant slurries [140], led to minimal enhancement of E_r values despite long range lamellar wall alignment evident in the *y*-axis (Figure 3.27b).

Figure 3.26d shows how E_r and UCS_r values in the *z*-axis exceeded those in the *y*-axis (Figure 3.26c) due to ice templated formation of lamellar walls aligned along the ice growth direction. Compression along the *z*-axis can generally cause crack formation and

growth due to local lamellar wall buckling [73, 75]. Previous work [141] showed how magnetic freeze casting with ≈ 350 nm alumina particles and a greater magnetic field strength (150 mT) produced broad aligned lamellar wall regions, similar to larger "grains," which facilitated a greater amount of compressive load distribution more evenly along the *z*-axis compared with smaller "grains" formed at a weaker magnetic field strength (75 mT). However, the orientation of those "grains" was angled more from the *y*-axis along magnetic field lines which emanated from the closer positioned bar magnet poles at 150 mT versus 75 mT. Less mechanical stiffening occurred in the *y*-axis at 150 mT compared with 75 mT because less "grains" made up of aligned lamellar walls were oriented along the *y*-axis [141]. For this work, E_r and UCS_r at 75 mT were not significantly enhanced compared with 0 mT in the *z*-axis (Figure 3.27b,c), but the desired objective for more lamellar wall alignment along the *y*-axis in the scaffold center at 75 mT was met and this resulted in significantly enhanced E_r in the *y*-axis (Figure 3.27b).

Comparison with particle and platelet freeze casting results from Ghosh, et al. [96, 140] began with consideration for the different slurry parameters and freeze casting conditions (Table 3.3). Among many differences, their use of larger particles (900 nm vs. 350 nm), larger platelets (8 μm x 400 nm vs. 5 μm x 200 nm) and a higher solid loading amount (15 vol% vs. 10 vol%) resulted in SEM micrographs of scaffold cross-sections with much less mineral bridging between lamellar walls. At a comparable freeze front velocity (FFV ≈ 25 μm/s), Ghosh, et al. [140] had $3 < m_s < 6$ values for particle and platelet mixture conditions which were consistent with their observed lamellar and slightly dendritic structures. At a similar FFV ≈ 25 μm/s, the $1.4 < m_s < 2.2$ values from this work were consistent with much more dendritic morphology (Figure 3.22). Overall, assessment

for how increased platelet percentage affected mechanical properties in the *z*-axis must account for the big disparities evident in m_s values between this work and Ghosh, et al. [140], which were the result of differences in freeze casting parameters as well as sintering conditions (1550 °C for 4 hours vs. 1500 °C for 3 hours).

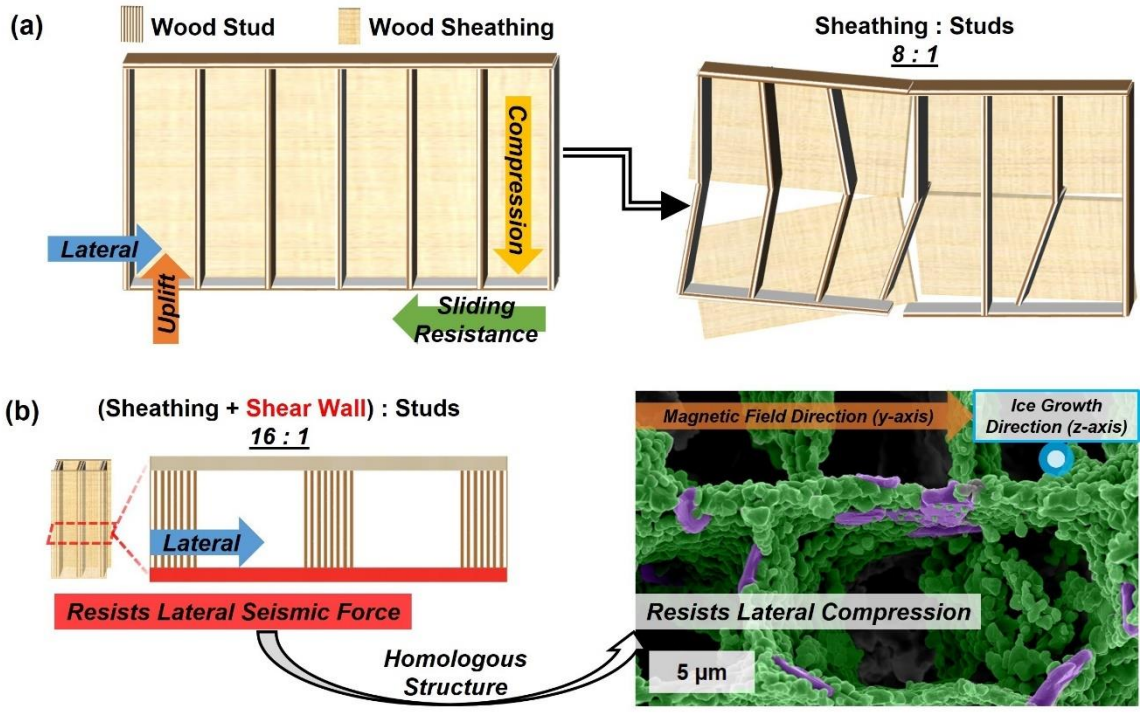

Figure 3.28: Schematic of an exterior wall from a light-frame construction house made with wood sheathing and studs compared with a scaffold portion made of alumina particles and platelets. (a) A residential exterior wall has plywood sheathing fastened to wood studs spaced equidistant center-to-center distance apart from each other for an 8:1 width ratio of sheathing to studs. A house can slide, rack or overturn off its foundation due to seismic forces that cause exterior wall failure. (b) An exterior wall retrofit with a shear wall has a 16:1 width ratio of sheathing to studs that provides enhanced lateral seismic force resistance. Intralamellar and interlamellar magnetized alumina platelets (purple) and particles (green) aggregate synergistically during freeze casting at 75 mT. A 7:1 ratio of particles to platelets produced enhanced stiffness in the magnetic field direction. Magnetic freeze cast porous scaffolds are homologous to shear wall reinforced exterior walls in light-frame wood houses by structure (studs and sheathing = mineral bridges and lamellar walls, respectively) and resistance to lateral force.

Multi-axis aligned porosity in 7:1 particle to platelet ratio scaffolds occurred due to microstructural arrangement of alumina particle and platelet morphologies by ice crystal growth and an applied magnetic field. A natural macrostructural analog with multi-axis aligned porosity is trabecular bone found in long bones close to joints and within vertebrae

[150], although the dimensions are an order of magnitude greater than for these scaffolds (hundreds versus tens of microns). At the microstructural level, trabecular bone is a composite that consists of nanoscale carbonated calcium phosphate platelets (dahllite, average length and width 50 x 25 nm) organized within a mineralized collagen matrix into a hierarchical structure with high strength and toughness [60, 61]. Anatomist Georg Hermann von Meyer and engineer Karl Culmann proposed a "trajectorial hypothesis", further refined by Julius Wolff and Wilhelm Roux, that trabecular bone porosity follows the trajectories of principal stresses and that bone has the ability to adapt to mechanical stimulus through a "quantitative self-regulating mechanism" [151].

Inorganic magnetic freeze cast structures cannot mimic the adaptive multi-functionality of organic trabecular bone, but 7:1 particle to platelet ratio scaffolds at the microstructural level do bear a resemblance to light-frame wood construction that accounts for ≈ 99% of housing in California [152]. Conventional walls made with wood studs and drywall cannot withstand multi-axial stresses associated with simultaneous lateral and uplift forces from earthquakes. Shear walls, typically consisting of plywood or gypsum sheathing fastened on either side of wood studs in exterior walls, are the primary lateral seismic force-resisting components in light-frame wood residential construction [152-155]. Homologous lamellar wall (sheathing) and mineral bridge (studs) microstructures evident in 7:1 particle to platelet ratio scaffolds can be compared with an 8:1 (Figure 3.28a) or 16:1 (Figure 3.28b) width ratio of sheathing to studs in standard or shear wall reinforced residential exterior walls, respectively. Heterogeneous particle and platelet morphologies, made of homogeneous alumina and arranged in a mechanically synergistic manner along the *y*-axis by magnetic freeze casting, can be sintered to make continuous, nearly

orthogonal, interfaces between lamellar walls and mineral bridges. Freeze casting that incorporates bioinspiration from ice and trabecular bone can also be reimagined through an alternate prism for manmade structures.

3.3.6 Conclusions

Magnetic freeze casting was carried out with surface magnetized alumina particles (≈ 350 nm) and platelets (≈ 5 μm diameter, ≈ 200 nm thickness) at varying particle to platelet ratios (0:1, 1:3, 1:1, 3:1, 7:1, 1:0) and magnetic field strength (0, 75 mT). Aggregation of particles and platelets into chains at 75 mT that led to lamellar wall alignment in the *y*-axis was dependent on size, aspect ratio and a preponderance of either particles or platelets within the slurry system. Magnetometer data indicated larger magnetized platelets had greater interaction energy than smaller particles and ≈ 98% lamellar wall alignment in the *y*-axis was confirmed in homogeneous platelet scaffolds with scanning electron microscopy (SEM). Scaffold center regions from heterogeneous mixtures of particles and platelets (1:3, 1:1, 3:1, 7:1) were examined with SEM and lamellar wall alignment in the *y*-axis was observed in all, except for the 1:1 particle to platelet ratio condition. Microstructural ordering between dissimilar particles and platelets as well as long range lamellar wall alignment (≈ 60%) in the *y*-axis were most evident in 7:1 particle to platelet scaffolds. Young's modulus (≈ 225%) and strength (≈ 40%) were both enhanced in the *y*-axis for 7:1 particle to platelet scaffolds. Previous magnetic freeze casting work with different sized magnetized alumina particles and magnetic field strengths was further expounded upon using varying ratios of magnetized particles and platelets freeze cast at an optimal magnetic field strength (75 mT). Microstructural resemblance of

7:1 particle to platelet scaffolds to light-frame wood construction with shear wall sheathing and studs can extend inspiration sources beyond the bioinspired.

3.4 Magnetic Freeze Casting with Magnetized Hydroxyapatite Particles

3.4.1 Introduction

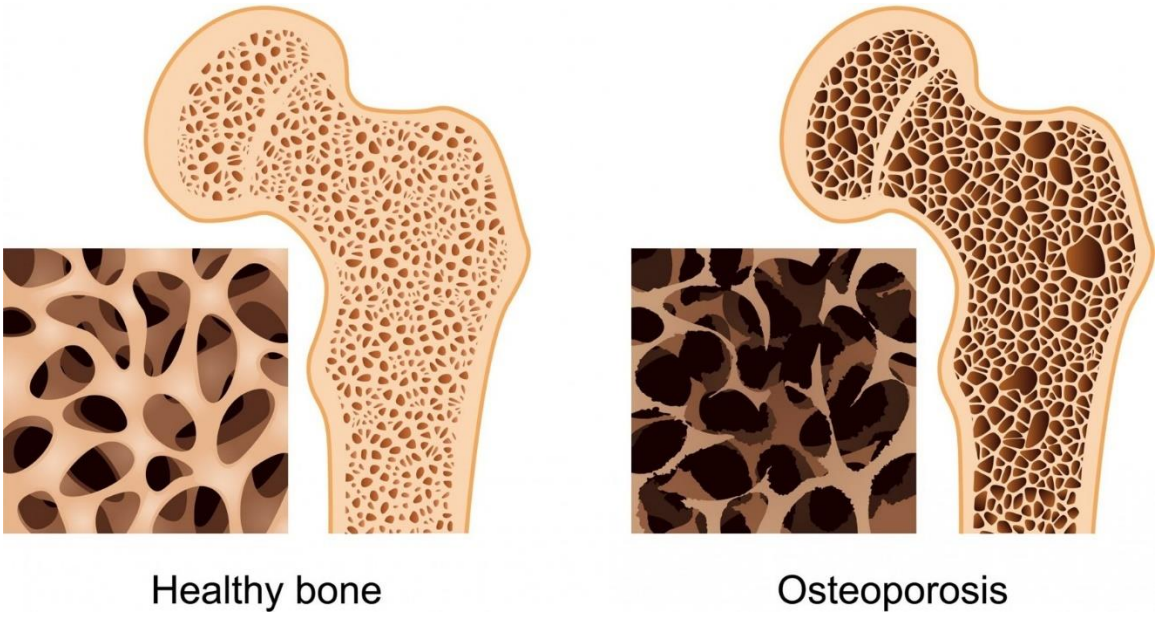

Figure 3.29: Osteoporosis erodes the spongy interior of bone, which causes bone brittleness, especially in the growing elderly population. A cross-section of the upper portion of the femur bone is shown. Images taken from [157].

Osteoporosis in the spongy layer of bones can occur when bone mass erodes, not enough new bone mass is made, or both adverse outcomes result simultaneously (Figure 3.29). Osteoclasts, bone cells that absorb bone tissue, typically work in zero-sum harmony with osteoblasts, bone cells that secrete matrix for bone tissue formation, to maintain sufficient bone mass density. Currently, the National Osteoporosis Foundation (NOF) estimates osteoporosis and low bone mass to be prevalent in nearly 44 million men and women aged 50 and older, which represents 55% of all individuals in that age group within the United States [156]. The total number of affected Americans aged 50 and older is expected to climb to more than 61 million by 2020, although greater awareness about

lifestyle, diet and potential treatment options may curb that growing trend slightly [156]. Women, more so than men, make up 80% of nearly 14 million Americans who currently have osteoporosis [156].

Table 3.5: T-scores within -1 standard deviation (SD) of the mean of healthy 30-year old adults are considered normal or healthy, between -1 and -2.5 indicate low bone mass and lower than -2.5 indicate osteoporosis onset. The greater the T-score negative number, the more severe the degree of osteoporosis [158].

World Health Organization (WHO) Definitions Based on Bone Mineral Density (BMD) Levels	
Level	***BMD T-Score Comparison to Young Adult Mean***
Normal	within -1 SD
Low Bone Mass	between -1 and -2.5 SD
Osteoporosis	below -2.5 SD
Severe Osteoporosis	below -2.5 SD and previous osteoporotic fractures

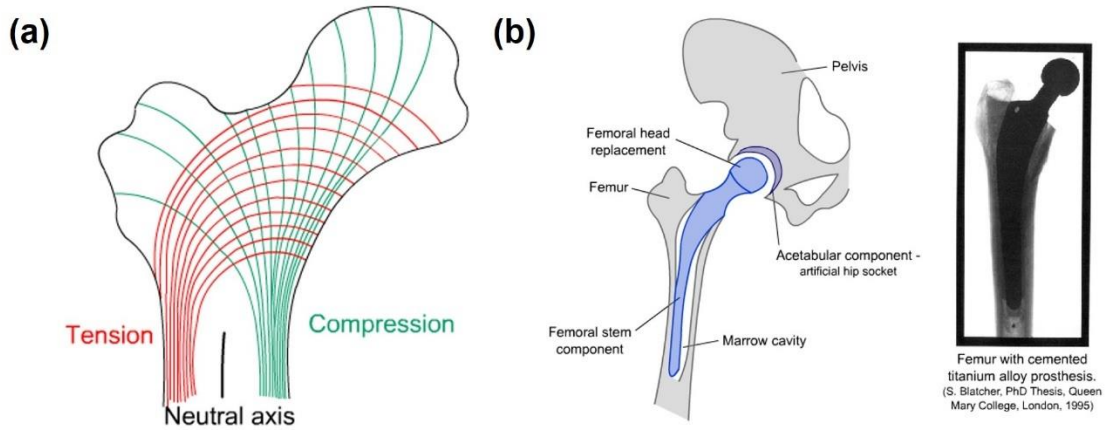

Figure 3.30: The computed lines of constant tensile (red) and compressive (green) stresses are indicated after analysis of transverse femur bone cross-sections (a). A diagram and radiograph of a femoral implant used for a total hip replacement (b). Images taken from [159].

Low bone mass or osteoporosis can be diagnosed with a bone mineral density (BMD) test. The most widely known one is called a central dual-energy x-ray absorptiometry (central DXA) test, which is typically used to measure BMD in potential problem areas such as the hip and spine [158]. Central DXA test output for a patient comes in the form of a "T-score" that is representative of standard deviations (SDs) away from the BMD for the mean of healthy 30-year old adults (Table 3.5) [158]. The upper portion of the femur bone (Figure 3.29) includes the exterior cortical layer and two systems of trabeculae (tensile, compressive) within the interior spongy, cancellous layer. The bending

moment experienced by the femur bone accounts for how the tensile and compressive trabeculae arrange along curved paths from the outer sides of the bone shaft to intersect at right angles (Figure 3.30a). Trabeculae aligned along tensile stress lines are generally thinner than compressive ones with variation based on magnitude of stresses at various points [159].

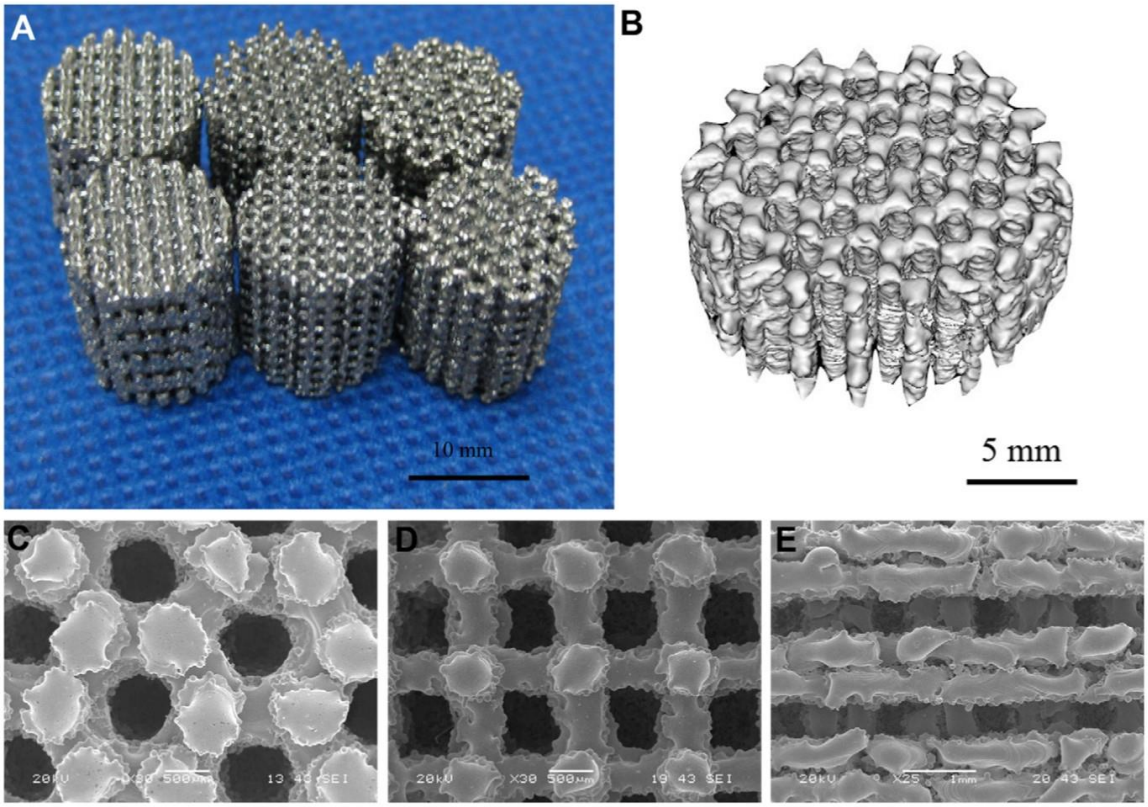

Figure 3.31: Honeycomb-like porous Ti-6Al-4V implants can be designed with commercial computer-aided design (CAD) software and made by an electron beam melting (EBM) process. Image taken from [160].

Bone is a composite made up of hydroxyapatite (HA, chemical formula $Ca_{10}(PO_4)_6(OH)_2$), collagen fibers, water and other substances (proteins and inorganic salts). An osteoporotic bone implant (Figure 3.30b) must resemble the complex mechanical properties of bone to avoid subsequent onset of stress shielding and bone remodeling that can occur post-implantation. Bone is a responsive and adaptive material that necessitates a

stress of 25-40 MPa for ossification by osteoblasts and resorption by osteoclasts to maintain a mutually antagonistic balance with consistent BMD levels [159]. Cancellous bone has much more surface area and can deteriorate four times as quickly as cortical bone due to stress shielding since ossification and resorption occurs constantly on its surface. Thus, extensive bone remodeling can result whenever a metal implant much stiffer than bone bears more of the body load.

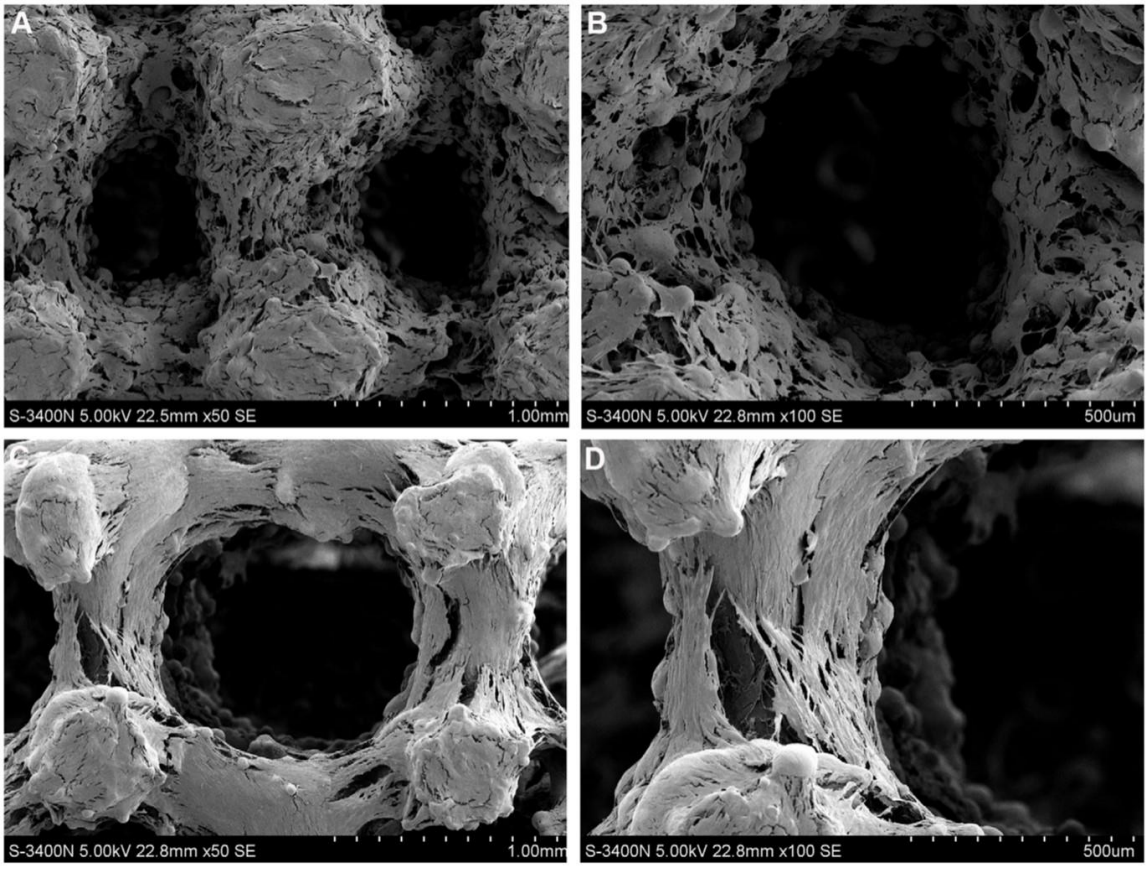

Figure 3.32: Osteoblasts on porous Ti-6Al-4V implants after 14 days of culture. Image taken from [160].

Ti-6Al-4V, a titanium alloy with 6% aluminum and 4% vanadium by weight, is typically used for bone implants rather than commercial purity (cp) titanium for several reasons, including cost, increased toughness, improved fatigue resistance and treatment during sintering to control porosity [159]. A Ti-6Al-4V implant with 40% porosity has

similar mechanical properties as cortical bone, but there are huge differences compared with the cancellous bone where the femoral stem component is fixated with polymer bone cement within the bone shaft [159]. Additional Ti-6Al-4V implant porosity can be designed with commercial computer-aided design (CAD) software using a selective electron beam melting (EBM) process (Figure 3.31). Alkali-heat treatment plus a soak in simulated body fluids (SBF) solution made a biomimetic coating for osteoblast adhesion (Figure 3.32).

Despite that bone is a composite primarily made up of mineral (HA) and biopolymer (collagen), HA is too brittle and polymers are too susceptible to creep and fatigue to be considered suitable materials individually for bone implants. The nanocomposite nature of HA and collagen bears responsibility for the excellent multi-axis mechanical properties evident in bone [161]. The end goal is for there to be just one surgery without any follow-up procedures that may be required due to adverse effects from bone remodeling. It would be especially helpful for elderly patients undergoing osteoporotic bone procedures to use a resorbable multi-axis strengthened composite implant made of porous HA and a structural polymer that can support new osteoblast ingrowth. Magnetic freeze casting [1-4, 141, 162] presents a bottom-up assembly method that is much less cost prohibitive than the previously described top-down fabrication method for making porous bone implants [160].

Most recently, extrinsic control of lamellar wall alignment in porous ceramic scaffolds was achieved at an appropriate magnetic field strength using surface magnetized alumina particles of different sizes [141] or particle and platelet mixtures of varying ratios [162]. The density difference between dissimilar ceramic materials, α-alumina (≈ 4 g/cm^3) and HA (≈ 3.15 g/cm^3), was accounted for to get the same average number of

superparamagnetic magnetite nanoparticles (≈ 10 nm) per ceramic particle. The calculation methodology for determining the average number of superparamagnetic magnetite nanoparticles per HA particle is shown in Table 3.6. The same ferrofluid amount (100 uL) was used to surface magnetize different weighed amounts of ceramic particles (e.g. 2.5 g alumina, 1.97 g HA) based on a density proportional ratio that was applied across different experimental studies.

For example, using the density proportional ratio for dissimilar density materials with the same particle size and volume resulted in the same average number of superparamagnetic magnetite nanoparticles per particle. This methodology was especially useful for comparing measured magnetic moments of surface magnetized particles since the moment values were then based entirely upon particle size, which itself was measured directly by the dynamic light scattering (DLS) method. A direct empirical relationship was observed between large surface magnetized particle size and large magnetic moment, which helped guide experimental design for the applied magnetic field strength needed to align HA particles (≈ 2 μm) much larger than the previously used largest alumina particles (≈ 350 nm) [141].

3.4.2 Materials and Methods

3.4.2.1 Particle Surface Magnetization

HA (≈ 2 μm particles measured by dynamic light scattering technique (DLS) [97-99, 141, 143-146]; Trans Tech, Adamstown, MD, USA) with bulk density of 3150 kg/m^3 was surface magnetized following a previously described protocol [141]. 1.97 g of HA (ratio for ≈ 3.15 g/cm^3 material density was equal to 2.5 g of alumina for ≈ 4 g/cm^3 material density) was stirred in 75 mL distilled water. Dropwise addition of 100 μL anionic

ferrofluid (EMG-605, Ferrotec, Bedford, NH, USA), diluted in 5 mL distilled water, to the stirring slurry changed the white HA to a light brown color (Figure 3.33a). The surrounding solution became clear after stirring for 12 hours. Surface magnetized HA was then rinsed with distilled water, vacuum filtered and dried for 12 hours at 100˚C before being used for magnetic freeze casting (Figure 3.33b).

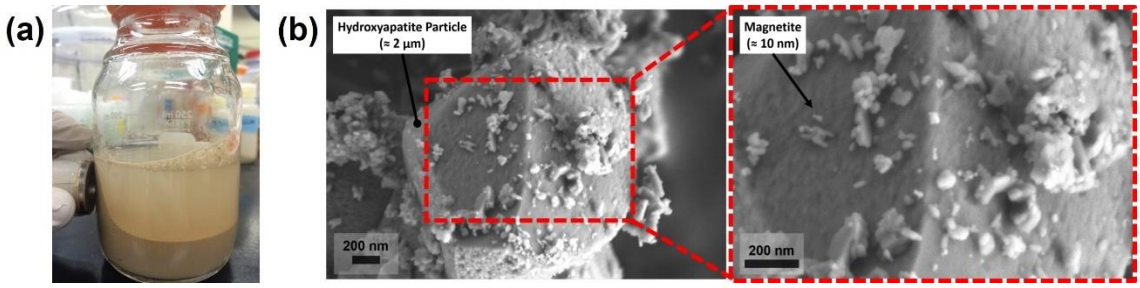

Figure 3.33: A bulk solution of surface magnetized HA is shown to be magnetically responsive to a nearby ring magnet (a). Superparamagnetic magnetite nanoparticles (≈ 10 nm) in ferrofluid coated with cationic charged surfactant electrostatically stuck to the oppositely charged HA particle (≈ 2 µm) surface (b).

3.4.2.2 Magnetic Materials Characterization

Magnetized HA (≈ 15-30 mg) was characterized with a vibrating sample magnetometer (VSM, VersaLab, Quantum Design International, San Diego, CA, USA). Mass magnetization (*M*, emu/g) in response to a sweeping magnetic field (0-300 mT, Figure 3.34), as well as magnetic moment (*m*, Am^2) calculated from measured particle volume (*v*) by DLS (particles) were determined using Eqns. 4 and 5. The methodology for calculating number of magnetite nanoparticles per HA particle, as well as corresponding magnetization value for an individual magnetized HA particle, is detailed in Table 3.6.

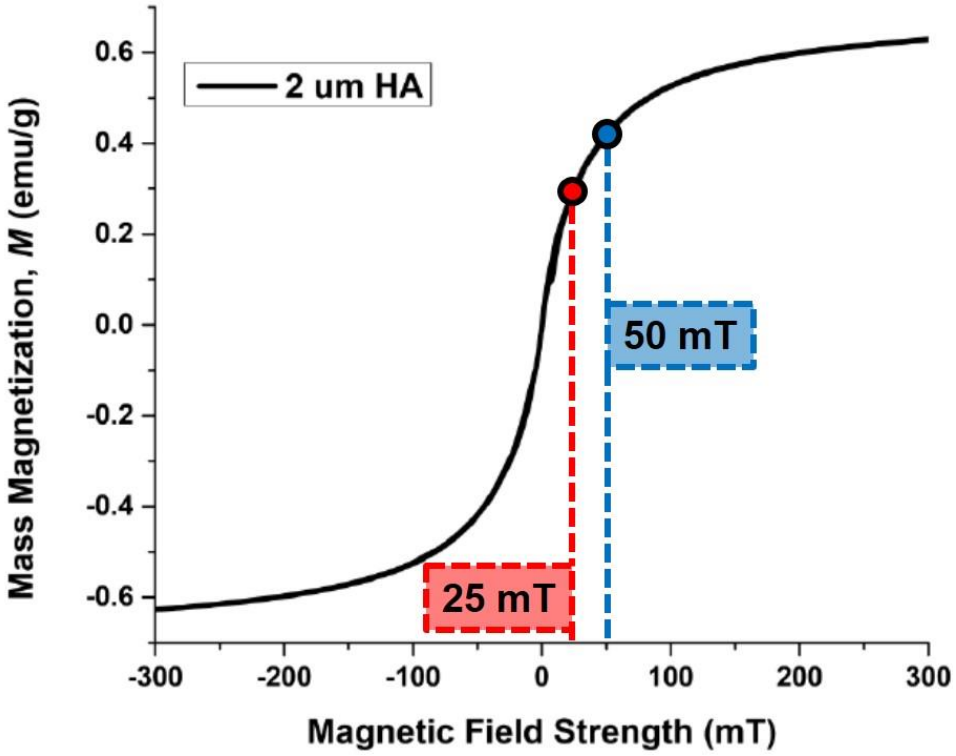

Figure 3.34: Mass magnetization, M, values determined with Eqn. 4 using magnetometer measurements for surface magnetized HA (black) subjected to a sweeping magnetic field, H (units converted to mT). Values for M at the applied magnetic field strengths (25, 50 mT) during magnetic freeze casting are indicated.

3.4.2.3 Magnetized Slurry Preparation

Slurries of magnetized HA particles (10 and 20 vol%) were prepared (by weight HA) with organic binders, 1 wt% polyvinyl alcohol (100,000 g/mol molecular weight (MW), Alfa Aesar, Ward Hill, MA, USA) and 1 wt% polyethylene glycol (PEG, 10,000 g/mol MW, Alfa Aesar, Ward Hill, MA, USA), and 1 wt% anionic dispersant (Darvan 811, R. T. Vanderbilt Company, Inc., Norwalk, CT, USA). Alumina grinding media was added and the slurry was ball milled for 24 hours.

3.4.2.4 Magnetic Freeze Casting

A vise grip (Panavise, Reno, NV) with ≈ 420 mT bar magnets (N52 grade, K&J Magnetics, Inc. Pipersville, PA, USA) attached to either end was placed 8 or 10 cm apart along the transverse *y*-axis using a previously described setup [141]. Magnetic field

strength at the midpoint between the bar magnets surrounding the polyvinyl chloride (PVC) mold containing the slurry was measured with a Gauss meter to be ≈ 50 or ≈ 25 mT for 8 or 10 cm magnet gaps, respectively. Freeze casting with a magnetized HA slurry was conducted either with a magnetic field (≈ 50 or ≈ 25 mT) along the *y*-axis or with no magnetic field. A grooved edge filed on the inside wall of the PVC mold was aligned with the bar magnets to provide a visual indicator for the applied magnetic field along the *y*-axis in sintered samples.

Table 3.6: Calculation methodology for determining the number of magnetite nanoparticles per HA particle and its corresponding magnetization value.

(*A*)	Mass (g) of an individual HA particle calculated with volume (cm^3) from DLS measured average particle size (≈ 2 μm diameter with assumed spherical shape) and HA density (≈ 3.15 g/cm^3) $Individual\ HA\ Particle\ Mass\ (g) = Volume\ (cm^3) \times Density\ (\frac{g}{cm^3})$
(*B*)	$Bulk\ HA\ Particle\ Mass\ per\ Magnetization\ Batch = 1.97\ g$
(*C*)	$Number\ of\ HA\ Particles\ per\ 1.97\ g\ Magnetization\ Batch = \frac{1.97\ g}{(A)\ value}$
(*D*)	Mass (g) of an individual magnetite particle calculated with volume (cm^3) from supplier provided particle size (10 nm with assumed spherical shape) and magnetite density (5.15 g/cm^3) $Individual\ Magnetite\ Particle\ Mass\ (g) = Volume\ (cm^3) \times Density\ (\frac{g}{cm^3})$
(*E*)	$Ferrofluid\ Volume\ (cm^3)\ to\ Magnetize\ 1.97\ g\ HA = 0.1\ cm^3$
(*F*)	Volume (cm^3) of magnetite in ferrofluid (0.1 cm^3) used to magnetize a bulk HA particle batch (1.97 g) based on supplier provided information (1-4 vol% magnetite in ferrofluid, assume upper limit amount of 4 vol% magnetite) $Magnetite\ Volume\ (cm^3)\ in\ 4\ vol\%\ Ferrofluid\ (0.1\ cm^3) = 0.04 \times 0.1\ cm^3 = 0.004\ cm^3$
(*G*)	$Magnetite\ Mass\ (g)\ in\ 4\ vol\%\ Ferrofluid\ (0.1\ cm^3) = 0.004\ cm^3 \times Density\ (\frac{g}{cm^3})$
(*H*)	$Number\ of\ Magnetite\ Particles\ per\ Surface\ Magnetization\ Batch = \frac{(G)\ value}{(D)\ value}$
(*I*)	$Number\ of\ Magnetite\ Particles\ per\ HA\ Particle = \frac{(H)\ value}{(C)\ value}$
(*J*)	$Individual\ HA\ Particle\ with\ Adsorbed\ Magnetite\ Mass\ (g) = [(A)\ value] + \{[(D)\ value] \times [(I)\ value]\}$
(*K*)	$Mass\ Magnetization\ of\ Magnetized\ HA\ Particles\ \left(\frac{emu}{g}\right) = 0.293\ \left(\frac{emu}{g}\right)\ for\ HA\ Particles\ at\ 25\ mT\ and\ 0.415\ \left(\frac{emu}{g}\right)\ for\ HA\ Particles\ at\ 50\ mT$
(*L*)	$Magnetization\ of\ Individual\ Magnetized\ HA\ Particle\ (emu) = [(J)\ value] \times [(K)\ value]\ at\ 25\ mT\ and\ [(J)\ value] \times [(K)\ value]\ at\ 50\ mT$

After ball milling, the magnetized HA slurry was degassed for 15 minutes by vacuum before 5 mL was poured into a PVC mold and centered underneath the magnetic field apparatus. Freezing occurred from the bottom upward using a previously described freeze casting device [1] and freezing front velocity (FFV) was estimated as the total frozen scaffold height (≈ 45 mm) divided by the total freezing time (≈ 1,800 s) to get FFV ≈ 25 μm/s [96, 138, 140, 162]. Frozen samples were lyophilized with a bench-top freeze dryer (Labconco, Kansas City, MO, USA) at -50 °C and 3.5 x 10^{-6} Pa for 48 hours to sublime ice crystals and leave behind fragile 'green body' scaffolds made up of HA particles that were held together by polymer binders. Samples were sintered in an open air furnace for 3 hours at 1300°C with heating and cooling rates of 2°C/min following a previously reported procedure [1].

3.4.2.5 Mechanical Characterization

Six scaffolds each were prepared for 10 and 20 vol% HA slurries magnetic freeze cast at 50 and 25 mT magnetic field strength. Compression testing of the scaffolds was performed on a 3342 Instron materials testing machine (Instron, Norwood, MA) with a 500 N static load cell at a constant crosshead velocity of 0.005 mm/s following previous procedures [1, 4, 75, 76, 141, 162]. Three samples (≈ 5 mm^3 cubes) cut from each scaffold center, where uniform porosity was evident, were compressed in the transverse (*x*-axis), magnetic field (*y*-axis) and ice growth (*z*-axis) directions for each condition. Ultimate compressive strength and Young's modulus were determined from the maximum stress and linear slope of the stress–strain curves, respectively.

3.4.2.6 Scanning Electron Microscopy Characterization

Two of the six sintered scaffolds for each condition were sectioned at midpoint height, mounted to a stage and coated with colloidal graphite along the bottom and side walls. Iridium was sputter coated (EMITech K575X, Quorum Technologies Ltd., West Sussex, UK) for 15 s at 85 mA onto the top. Scanning electron microscopy (SEM) micrographs at 10 kV (spot size 3 nm) from a Philips XL30 field emission environmental scanning electron microscope (FEI-XL30, FEI Company, Hillsboro, OR) were stitched together along overlapping edges to assess long range lamellar wall alignment in the scaffold center. Lamellar wall regions were shaded different colors to indicate horizontal alignment (light blue, 22.5° offset from the y-axis), angled alignment (yellow, 22.5° to 67.5° offset from the y-axis) and no alignment (red, 67.5° to 90° offset from the y-axis). ImageJ software (National Institutes of Health, Bethesda, MD, USA) was used to quantify lamellar wall horizontal alignment, for the overlapped SEM micrographs area (6000 μm x 2700 μm) at 100x magnification within the scaffold center region used for mechanical testing, by dividing the light blue shaded scaffold area by the total scaffold area.

3.4.3 Magnetic Response of Magnetized Hydroxyapatite Particles

Magnetized HA particles subjected to a sweeping magnetic field, H, and plotted versus M (Eqn. 4, Figure 3.34) had an absence of hysteresis and magnetization at H = 0 on the M-H curve. This result confirmed the magnetized HA particles "responded" to a sweeping magnetic field in a superparamagnetic manner with less susceptibility (maximum slope) and saturation (maximum M value) than superparamagnetic magnetite nanoparticles alone [100], but with similar magnetic properties as composites with superparamagnetic magnetite cores [101]. DLS measurement after ball milling indicated ≈ 2 μm average HA particle size.

HA particles (1.97 g mass, ≈ 3.15 g/cm^3 density) were surface magnetized with the same amount of ferrofluid (0.1 mL) as was previously used for alumina particles (2.5 g mass, ≈ 4 g/cm^3 density), although the ferrofluid used for HA was cationic rather than anionic for alumina. The amount of surface adsorbed magnetite per HA particle was estimated based on assumptions for spherical magnetite nanoparticle size (≈ 10 nm) and fraction in ferrofluid (4 vol%), as detailed in Table 3.6. Overall, each HA particle had ≈ 77,850 adsorbed magnetite nanoparticles. Values of M at 25 and 50 mT multiplied by the mass of an individual HA particle with adsorbed magnetite yielded 5.93 x 10^{-12} and 8.42 x 10^{-12} emu magnetization values for surface magnetized HA particles at 25 and 50 mT, respectively.

3.4.4 Lamellar Wall Alignment

During magnetic freeze casting, 10 vol% magnetized HA particles aggregated into ≈ 60% aligned lamellar walls along the y-axis at 25 mT (Figure 3.35) for 3-4 minutes before ice nucleation occurred within the slurry. Magnetized HA subjected to ≈ 25 mT was predicted to aggregate into chains ($N^* > 1$) for ≈ 97.1% and ≈ 97.6% of 10 and 20 vol% slurries, respectively, based on particle sizes incorporated from DLS measurement. Magnetization of individual magnetized HA particles at 25 mT (5.93 x 10^{-12} emu) was more than 300x greater than that of individual magnetized ≈ 350 nm alumina particles at 75 mT (1.97 x 10^{-14} emu). Comparison of these individual particle magnetization values helps explain why much more lamellar wall alignment was observed for HA particle scaffolds at 25 mT (≈ 60%, Figure 3.35) than for ≈ 350 nm alumina scaffolds at 75 mT (≈ 20%, Figure 3.16a) along the *y*-axis [141]. As expected, there was no lamellar wall alignment of

magnetized HA particles at 0 mT, whereas long range alignment was definitely evident along the *y*-axis in the scaffold center at 25 mT (Figure 3.35).

Figure 3.35: Long range lamellar wall alignment in the transverse direction (*y*-axis) was evident for HA particle scaffolds freeze cast at 25 mT. (a) A 6000 µm x 2700 µm scanning electron micrograph from the scaffold center at 100x magnification was stitched together from an HA particle scaffold freeze cast at 25 mT. Analysis of lamellar wall orientation with ImageJ software indicated ≈ 60% alignment (light blue).

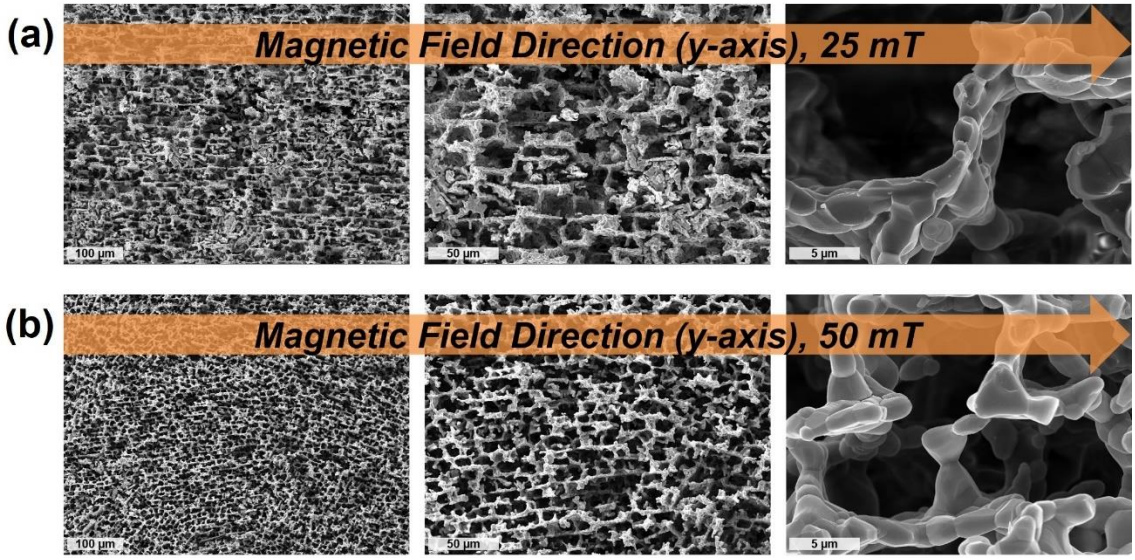

Figure 3.36: Lamellar wall alignment along the magnetic field direction (*y*-axis) was evident in 10 vol% HA particle scaffolds at both 25 mT (a) and 50 mT (b) magnetic field strength conditions.

Surface magnetized HA particles with large size and magnetic moment had a magnetic interaction energy that exceeded thermal energy to increase aggregation within *y*-axis aligned lamellar walls at both 25 and 50 mT magnetic field strength (Figure 3.36). Interestingly, the amount of long range lamellar wall alignment observed in a scaffold

cross-section of HA particles at 25 mT (≈ 60%) also matched the approximate observed amount of lamellar wall alignment in the 7:1 alumina particle to platelet condition at 75 mT (≈ 60%) with the greatest stiffness enhancement along the *y*-axis from past work [162]. Langevin Dynamic (LD) simulations used by Faraudo, et al. [91, 92, 94] predicted kinetics for average superparamagnetic colloid chain length as a function of time, although the systems used for theoretical prediction were much simpler than magnetic freeze casting slurries made up of varying sized surface magnetized particles and other components (dissolved polymers and dispersant). Exposure of a surface magnetized slurry, whether HA particles at 25 mT or a 7:1 alumina particle to platelet mixture at 75 mT, to a sufficient magnetic field strength gradient for some time beyond the currently implemented 3-4 minutes prior to ice nucleation should lead to increased chain formation in solution and then subsequently even more lamellar wall alignment observed in the porous scaffold along the *y*-axis.

3.4.5 Mechanical Properties

Freeze cast scaffold porosity from slurries of 10 and 20 vol% HA was consistent across all samples at ≈ 83-85% and ≈ 68-70%, respectively (Table 3.7), so direct comparison of mechanical properties could be made between scaffold cubes compressed along transverse (*x*-axis), magnetic field (*y*-axis) and ice growth (*z*-axis) directions at different magnetic field strengths (0, 25, 50 mT), as shown in Figure 3.37. Young's modulus (*E*) and ultimate compressive strength (UCS) were generally larger along the *y*-axis due to increased particle aggregation and more lamellar wall alignment from an applied magnetic field, which was significantly apparent for less porous 20 vol% HA scaffolds at 25 mT (Figure 3.37d).

Table 3.7: Porosity (%), Young's modulus (E) and ultimate compressive strength (UCS) for surface magnetized hydroxyapatite (HA) scaffolds freeze cast with or without a static magnetic field (0, 25, 50 mT). Compression occurred along the transverse (x-axis), magnetic field (y-axis) and ice growth (z-axis) directions. Sample size for each condition: N = 6. All data reported are mean ± standard error (standard deviation / √N).

	mT	**10 vol%**	**20 vol%**
Porosity (%)	0	83.64 ± 1.31	68.91 ± 2.16
	25	83.03 ± 0.92	69.50 ± 1.86
	50	84.34 ± 0.85	69.28 ± 2.94
***E*, MPa, *x*-axis**	0	5.17 ± 1.93	125.93 ± 23.47
	25	7.20 ± 1.27	81.03 ± 17.32
	50	5.17 ± 1.20	65.82 ± 18.55
***E*, MPa, *y*-axis**	0	15.43 ± 3.38	85.48 ± 6.48
	25	16.64 ± 0.77	138.93 ± 18.17
	50	24.21 ± 5.15	92.10 ± 7.60
***E*, MPa, *z*-axis**	0	27.03 ± 9.98	171.67 ± 26.16
	25	69.72 ± 26.99	126.61 ± 17.24
	50	50.27 ± 15.26	168.58 ± 26.33
UCS, MPa, *x*-axis	0	0.34 ± 0.10	3.80 ± 0.77
	25	0.42 ± 0.09	2.79 ± 0.58
	50	0.38 ± 0.06	3.31 ± 1.21
UCS, MPa, *y*-axis	0	0.57 ± 0.12	4.08 ± 1.01
	25	0.67 ± 0.03	5.85 ± 0.76
	50	0.69 ± 0.08	4.47 ± 0.57
UCS, MPa, *z*-axis	0	2.03 ± 0.73	17.54 ± 1.95
	25	2.84 ± 0.16	17.20 ± 2.58
	50	2.87 ± 0.27	15.35 ± 2.84

For previous magnetic freeze casting work [141], 10 vol% slurries of alumina particles with ≈ 80-85% porosity were sufficiently robust porous scaffolds to be able to extract meaningful compression measurement data to compare mechanical properties, specifically *E* along the *y*-axis, between different magnetic field strength conditions. However, 10 vol% HA slurries that produced similar ≈ 80-85% porous scaffolds were much more brittle than alumina scaffolds, which made meaningful conclusions from mechanical compression data harder to determine along the magnetic field direction. Thus, an additional 20 vol% HA slurry condition was added to this study to have less porous scaffolds that would not undergo brittle failure as quickly, such that the effects of additional lamellar wall alignment could be observed in the enhancement of *E* along the magnetic field direction. The 20 vol% HA slurry condition was predicted to significantly enhance

lamellar wall alignment compared with 10 vol% due to a substantial increase in ϕ_o, the volume fraction (vol%) of the slurry, used for calculation of the aggregation parameter (N*) from Eqn. 3.

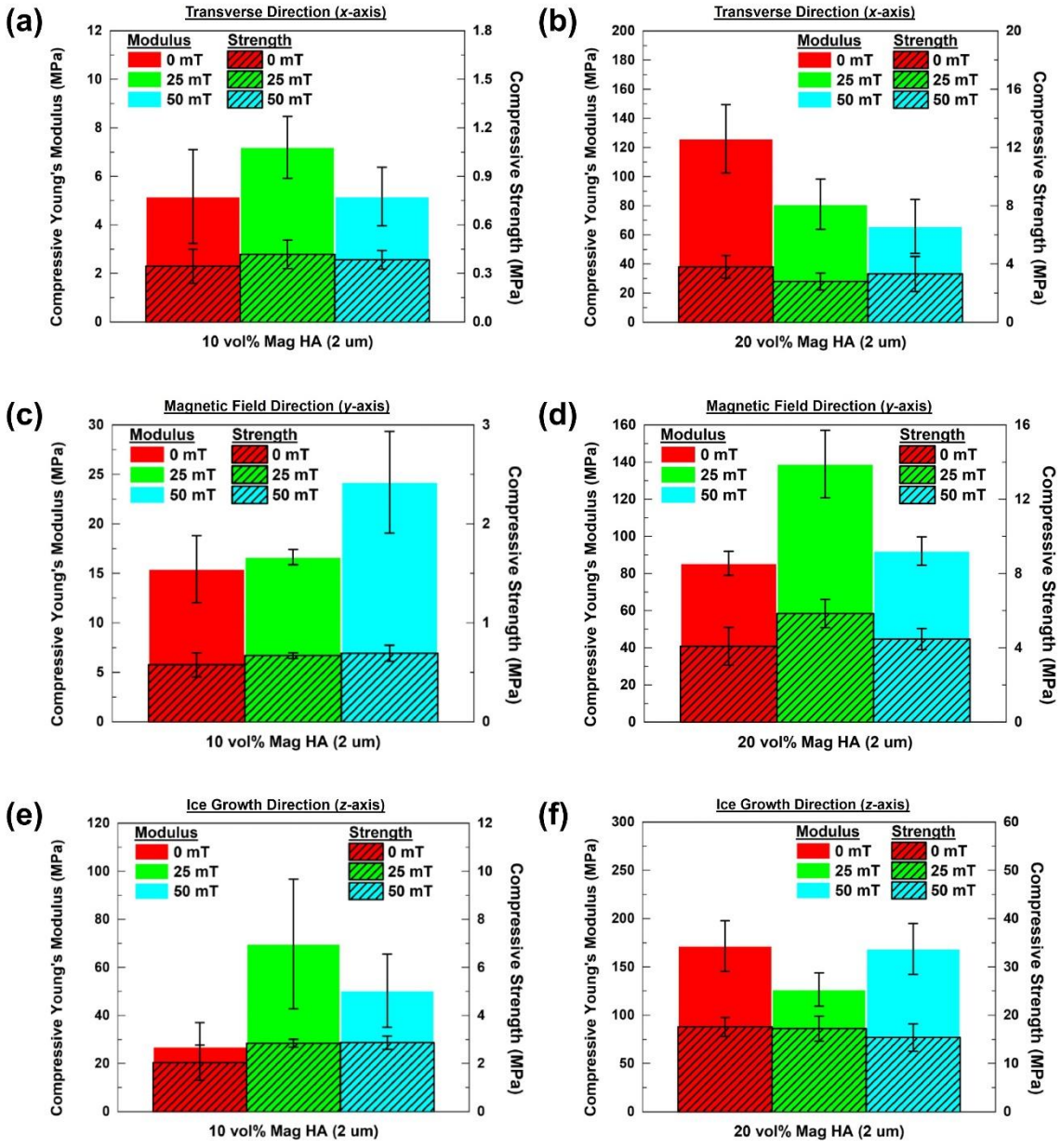

Figure 3.37: Comparison of compressive mechanical properties along the transverse (x-axis), magnetic field (y-axis) and ice growth (z-axis) directions for 10 and 20 vol% surface magnetized hydroxyapatite (HA) scaffolds freeze cast with or without a static magnetic field (0, 25, 50 mT). Young's modulus (E) and ultimate compressive strength (UCS) values are indicated for (a, c, e) 10 vol% and (b, d, f) 20 vol% conditions along x, y and z-axes. Data points are the mean of N = 6 measurements with error bars representing ± standard error (standard deviation / √N).

Mechanical properties in the transverse (Figure 3.37a,b) and ice growth (Figure 3.37e,f) directions provided less clear trends due to increased magnetic field strength. It was not clear what effect increased lamellar wall alignment in the magnetic field direction had, if any, on *E* and UCS. In general, both *E* and UCS increased in the magnetic field direction for 10 and 20 vol% slurry conditions. Taking a step back to examine the bigger picture, the full story can become more clear. Large HA particles with sufficiently large magnetic moment at low magnetic field strength (Figure 3.34) can readily aggregate at 25 mT to form highly aligned lamellar walls (Figure 3.35, Figure 3.36a) in the scaffold center that cause enhanced *E* in the magnetic field direction (Figure 3.37d).

A slightly greater magnetic field at 50 mT seemed to be too strong since mechanical properties of cubes extracted from the scaffold center were weaker than those at 25 mT. We speculate that the reason this result occurred was because the 50 mT condition aggregated more particles closer to the scaffold edges where the magnetic field gradient was stronger near the magnet poles (Figure 3.38). The difference between 25 and 50 mT may seem subtle, but we observed a similar relationship from past magnetic freeze casting work where mechanical properties for ≈ 350 nm alumina particles were worse at 150 mT compared with at 75 mT in the magnetic field direction (*y*-axis) [141]. Magnetic freeze casting experimental design to obtain lamellar wall alignment with enhanced mechanical properties in the scaffold center begins, but does not end, with slurries that have $N^* > 1$ (Eqns. 2, 3) at particular magnetic field strengths. Our magnetic freeze casting experiments with magnetized alumina and HA show that slurries made up of larger particles have greater magnetic moment sufficient for particle aggregation and lamellar wall alignment. For larger particle slurries with $N^* > 1$, the magnetic field strength amount that can produce

mass magnetization (M) values ≈ 0.25 - 0.3 emu/g (from VSM measurements) can lead to lamellar wall alignment with enhanced mechanical properties in the center, rather than the edges, of magnetic freeze cast scaffolds.

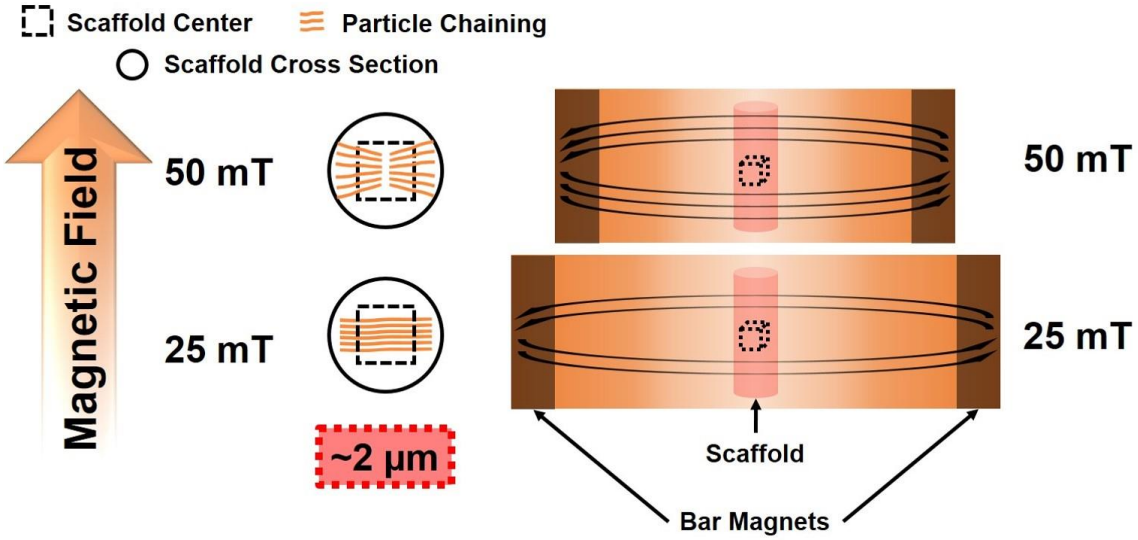

Figure 3.38: Lamellar wall alignment within the surface magnetize hydroxyapatite (HA) scaffold center as a function of magnetic field strength. The schematic indicates the extent of particle chaining (orange line) leading to lamellar wall alignment in the scaffold center (dotted box) for HA particles at varying magnetic field strength. Measured values input into Eqns. 2 and 3 led to predictions that 25 and 50 mT would induce chain aggregation and lamellar wall alignment along the magnetic field direction (y-axis). A stronger magnetic field (50 mT) closer to the magnet poles led to more angled alignment along magnetic field lines instead of more along the y-axis within the scaffold center.

The impact of these experimental results has tremendous potential for guiding future magnetic freeze casting experimental design to make porous scaffolds with multi-axis enhanced mechanical properties. As was noted previously for magnetic freeze casting with different sized alumina particles [141], the extent of interaction energy between magnetized particles needed to induce lamellar wall alignment depends on particle size, thermodynamic variables (temperature, volume fraction) that affect aggregation and time evolution for chain formation before ice nucleation during freeze casting [89, 90, 92]. Careful attention should be paid to the proper applied magnetic field strength since it must be just low enough to induce aggregation and produce lamellar wall alignment with

enhanced mechanical properties in the scaffold center. Differences between measured *M* values for magnetized HA at 25 mT (0.29 emu/g) and 50 mT (0.42 emu/g) may help explain why mechanical properties from the scaffold center were worse at 50 mT than at 25 mT. Perhaps more particle aggregation occurred along slightly curved magnetic field lines at 50 mT than along more linear field lines at 25 mT in the *y*-axis (Figure 3.38).

3.4.6 Conclusions

Magnetic freeze casting with a sufficiently low magnetic field (25 mT) applied to an aqueous slurry of surface magnetized hydroxyapatite (HA) particles can make bioinspired porous scaffolds strengthened specifically in the magnetic field direction (*y*-axis). Degradation of interior spongy bone due to erosion of the mineral phase can lead to bone brittleness over time. Preventative surgery to reinforce bone with a commercially pure or titanium alloy implant leads to stress shielding which requires follow-up surgeries due to bone remodeling and insufficient osteoblast integration. Spongy bone implants must more closely resemble bone as a biodegradable and biocompatible composite with mineral and biopolymer phases. The research work described herein addressed the multi-axis strengthening of the mineral phase through an experimental design that incorporates measurable material independent parameters. Generally, larger surface magnetized HA particles that undergo magnetic freeze casting at a sufficiently low magnetic field strength can produce lamellar wall alignment in the scaffold center, rather than the edges, with uniformly enhanced mechanical properties in the magnetic field direction (*y*-axis). Further work to fortify the polymer phase of the overall bone implant composite will be explained in the subsequent section.

3.5 Exterior and Interior Hydroxyapatite Scaffold Strengthening Mechanisms

3.5.1 Introduction

Porcupine quills (Figure 3.39) are lightweight, keratinous biological materials that have a cortex sheath wrapped around a closed-cell foam [163]. The quills can withstand large compression and flexure loads primarily due to the cortex layer (Figure 3.40) [164]. Freeze casting that uses directional freezing of water to generate strengthened porous scaffolds along the ice growth direction (*z*-axis) has an associated anisotropy issue whereby mechanical properties are much weaker along transverse directions. The overall structure resembles a brittle piece of chalk and presents a challenge that must be addressed to be able to make implants that can more closely resemble the actual structure of spongy bone.

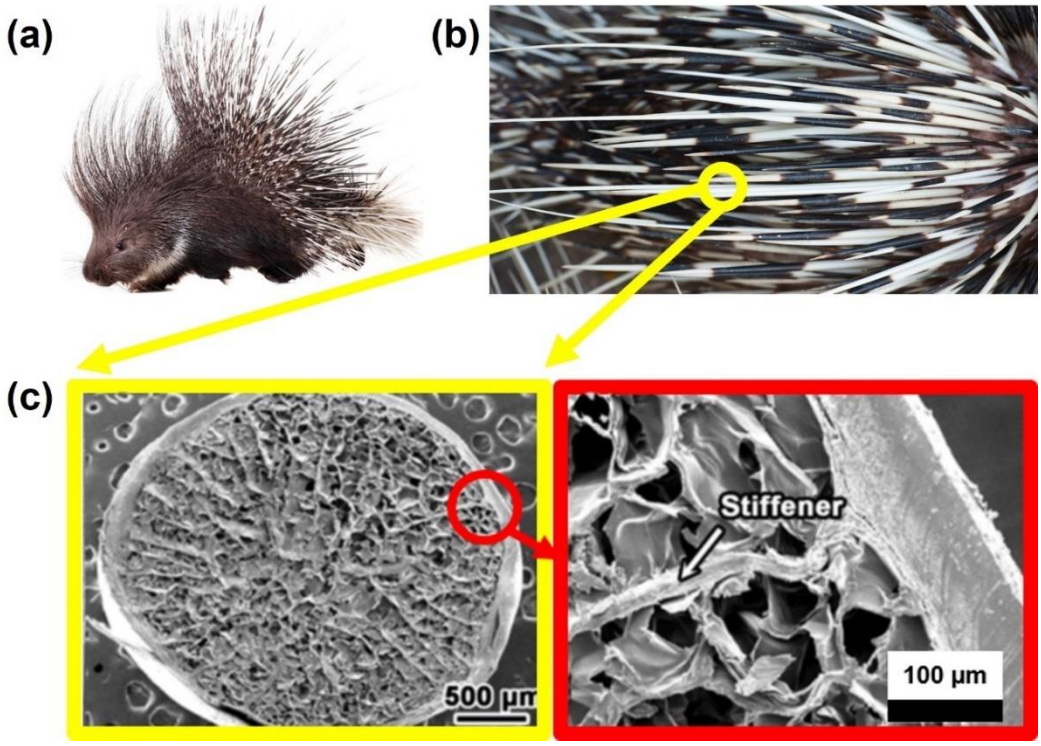

Figure 3.39: A porcupine (a) has quills (b) seen in SEM cross-sections for the species *Hystrix* (c) that consist of a keratinous closed-cell foam structure surrounded by a cortex layer. Images adapted from [163, 165].

Bioinspiration drawn from the cortex wrapped porcupine quill structure can be applied towards making an exterior strengthened composite suitable for future spongy bone

implants. Biocompatible, biodegradable thermoplastic polylactic acid (PLA) (Figure 3.41) made of renewable corn starch or sugar cane is commercially available as a shrink wrap film (≈ 50 μm) for various packaged products. PLA shrink wrapped as a label around a polyethylene terephthalate (PET) bottle resembles a porcupine quill cortex. The porcupine quill cortex has been shown to prevent buckling from applied axial compression force in the longitudinal direction [163, 164] and it most likely helps resist radial compression in natural systems as well. The Brazilian Test method is a radial scaffold compression method that can be used to measure splitting tensile strength along the transverse direction.

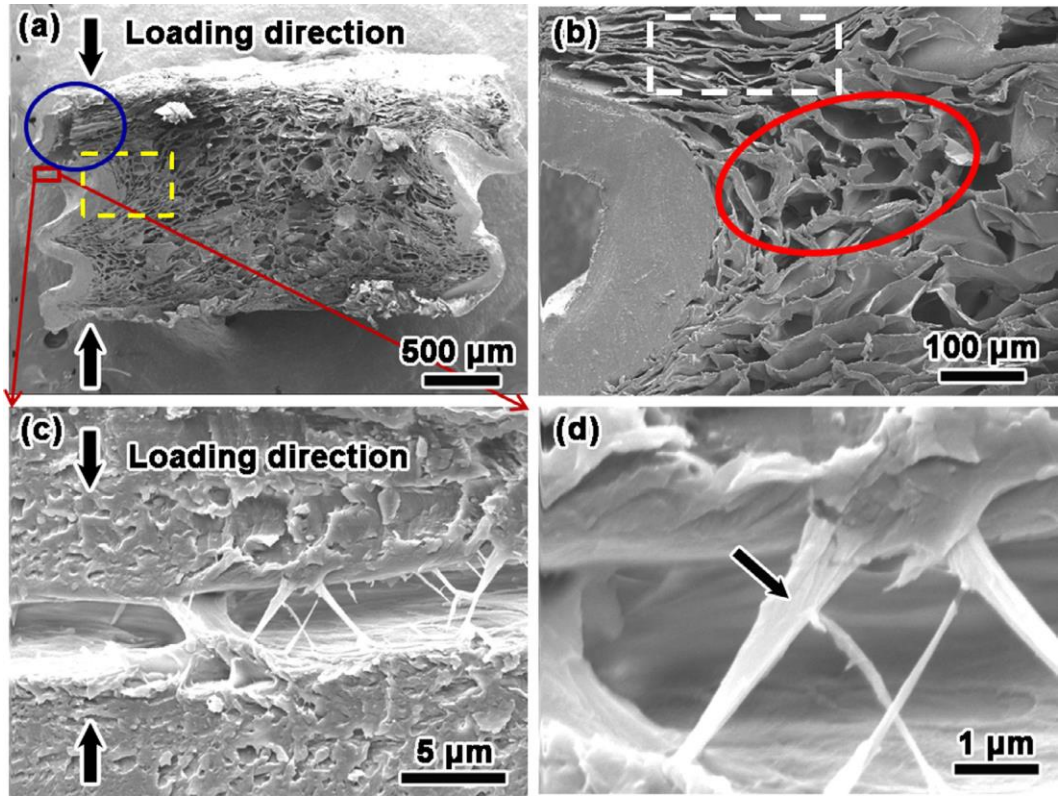

Figure 3.40: SEM micrographs of an axially compressed *Hystrix* quill cross-section morphology with deformed foam and pulled fibers close to the buckling cortex. Image taken from [164].

Keratin wrapped foam in porcupine quills is both lightweight and unusually strong. Compressive strain after onset of local buckling, but before final collapse failure reached between ≈ 70 and ≈ 90% [164]. PLA wrapped porous scaffolds can make for stronger

spongy bone implants, especially radially along axes transverse to the *z*-axis where the anisotropic porous scaffold structure is weakest. An additional dual network hydrogel infiltrated within the pores can provide for interior strengthening of a spongy bone implant composite. Both exterior and interior strengthening methods can be used for the polymer phase in combination with extrinsic methods such as magnetic freeze casting to align the mineral phase. Hydrogel mixtures with > 90 wt% water content can become hundreds of times stronger through dual networks of ionic and covalent crosslinked components.

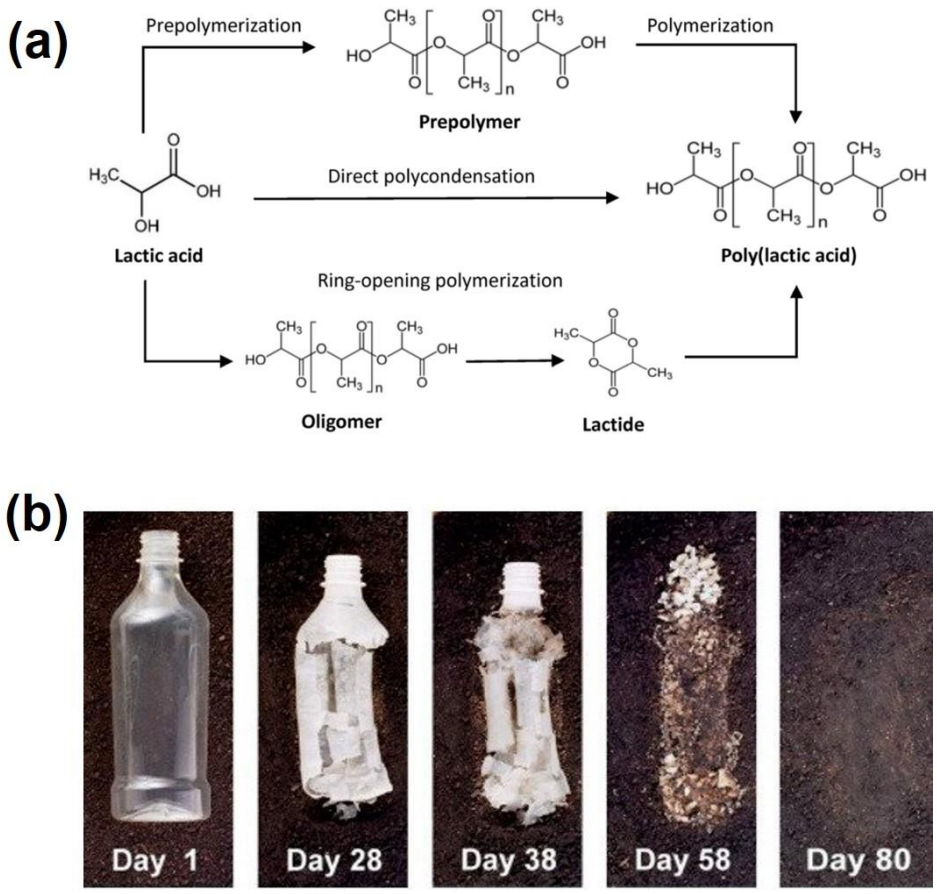

Figure 3.41: PLA synthetic pathway (a) and complete biodegradation of a bottle. Images adapted from [166].

Dual network hydrogels were first demonstrated by Gong, et al. [167] to have incredible synergistic mechanical properties compared with a single network hydrogel in

response to a high compression force (Figure 3.42a). Fracture stress for a single network hydrogel was 0.4 MPa, whereas the double network hydrogel had a fracture stress value of 17.2 MPa. Sun, et al. [168] developed highly stretchable and tough dual network hydrogels, made of polyacrylamide and alginate, that could be stretched to > 20 times the original length without rupture. Stress and stretch at rupture values were 156 kPa and 23 kPa, respectively, and the dual network hydrogel resisted rupture even when pre-notched (Figure 3.42b) to resemble the way collagen fibers align to resist tearing in skin [169].

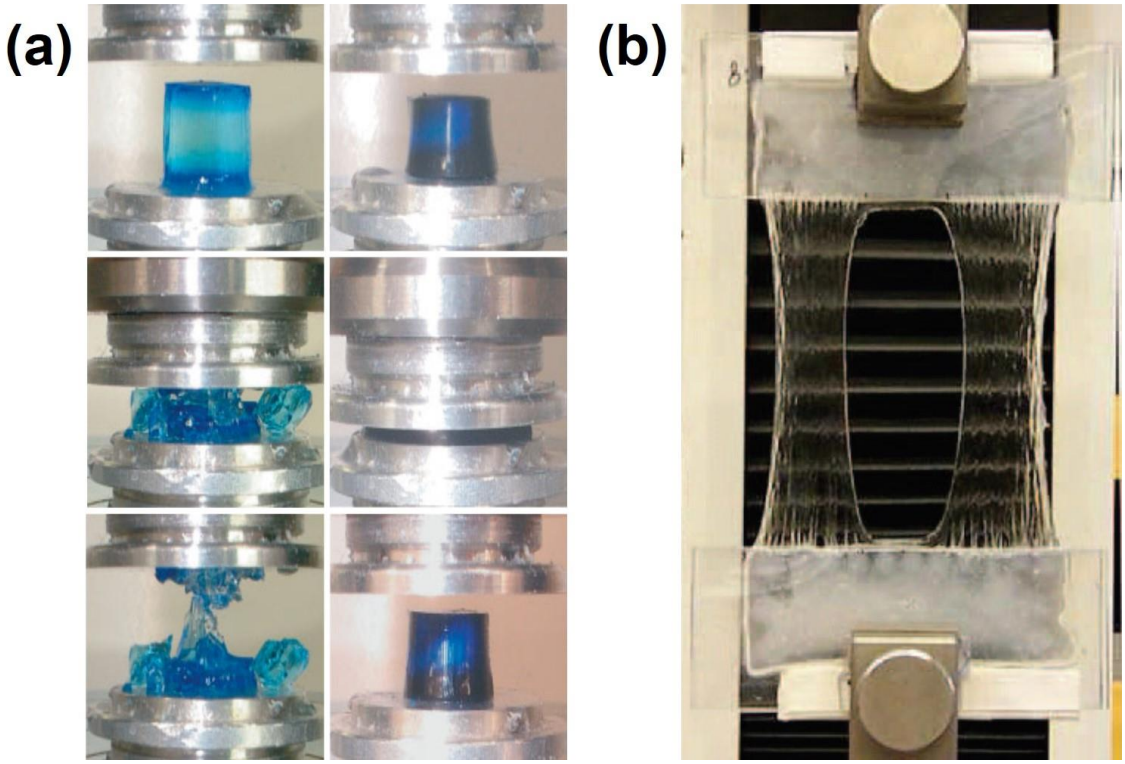

Figure 3.42: For compression force (a), a single network hydrogel (left) and dual network hydrogel (right) have fracture stress of 0.4 MPa and 17.2 MPa, respectively. For tensile force (b), even a pre-notched dual network hydrogel resisted rupture in a manner that resembled collagen fiber alignment for tear resistance in skin. Images taken from [167, 168].

The dual network hydrogel used by Sun, et al. [168] consisted of a mixture of covalent crosslinked polyacrylamide and ionic crosslinked alginate in a ratio which synergistically enhanced mechanical properties (Figure 3.43). Both covalent and ionic

parts of the hybrid hydrogel can be crosslinked at different preparation steps without adversely affecting each other. The toughening mechanism is due to polyacrylamide chains that bridge the crack and stabilize deformation in the background while chemical interactions between the hydrogel networks transfer the load over a large plastic zone near the crack tip. Ionic crosslinks between alginate chains break by unzipping to provide inelastic deformation over the large plastic zone that effectively blunts the crack tip edge.

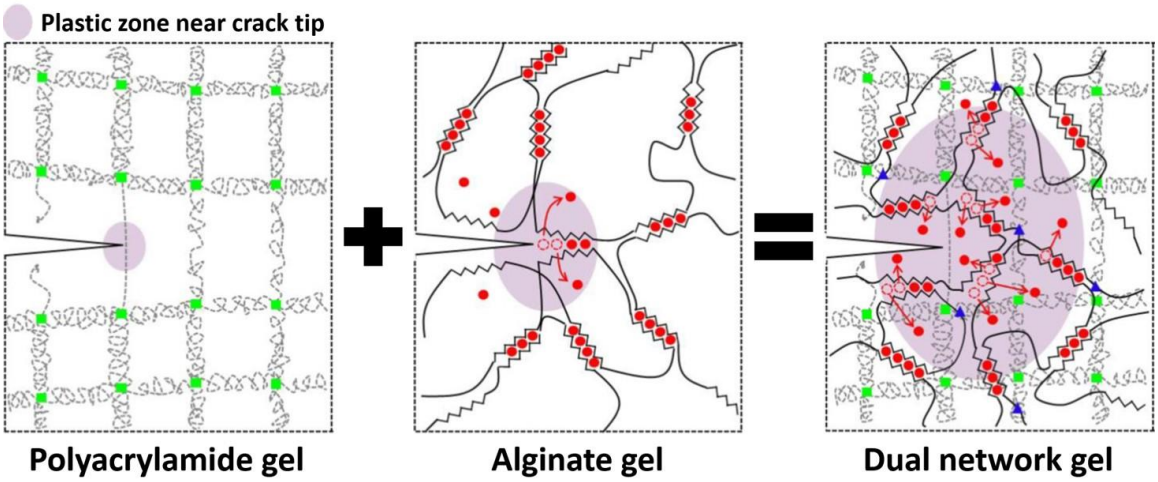

Figure 3.43: As a crack propagates through either individual covalent (polyacrylamide) or ionic (alginate) crosslinked hydrogels, the tensile forces involve either brittle covalent bond breaking or gradual ionic bond unzipping mechanisms, respectively. Combination of the two hydrogels in the right proportions makes for a synergistic effect whereby ionic unzipping expands the plastic zone to blunt the crack tip and fortify the covalent linked backbone framework. Images adapted from [168].

A spongy bone implant could use a dual network hydrogel, biocompatible for new osteoblast ingrowth, that is infiltrated within HA scaffold pores to interior strengthen and toughen the overall composite. However, polyacrylamide [168] is problematic for an actual spongy bone implant due to acute toxicity associated with any unreacted acrylamide monomer leftover within the dual network hydrogel. Polyacrylamide can be replaced with biocompatible polyethylene glycol diacrylate (PEGDA), which has been FDA approved for many biomedical applications (Figure 3.44). Calcium used to crosslink alginate within

the infiltrated dual network hydrogel could also integrate with HA scaffold walls to make a composite resembling interconnected mineral and biopolymer phases in bone. Calcium acetate is an excellent phosphate binder that could be wicked up into the scaffold pores by capillary force as a solution and become a "seed" bound to phosphate in HA scaffold walls. Later infiltration of the PEGDA and alginate dual network hydrogel could then use the seeded calcium in the HA scaffold walls to crosslink alginate within the dual network hydrogel and make a tough, interconnected mineral and polymer phase composite.

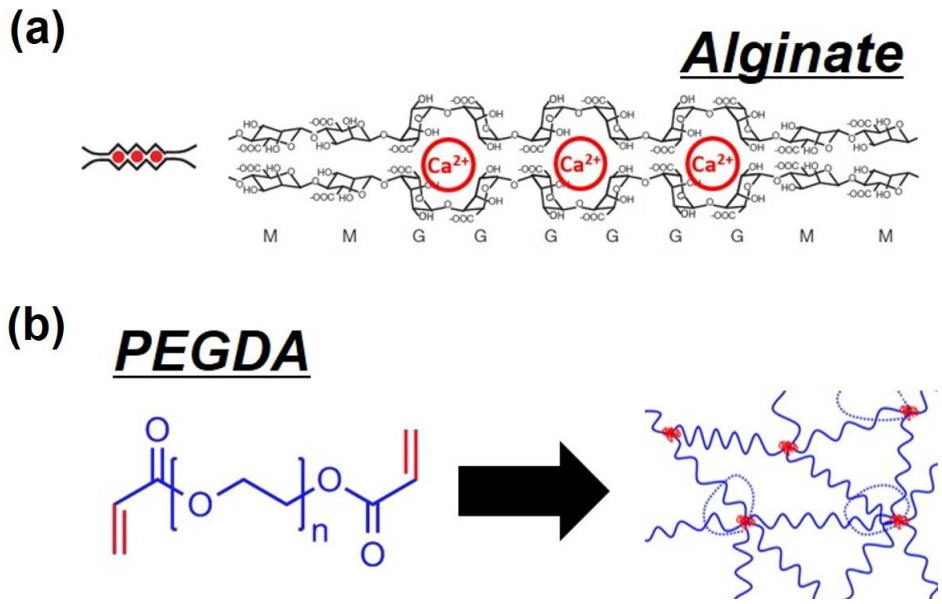

Figure 3.44: Ionic crosslinked alginate with calcium ions (a) and covalent crosslinked polyethylene glycol diacrylate (PEGDA) that can make up the components of a biocompatible dual network hydrogel.

3.5.2 Materials and Methods

The step-by-step process for shrink wrapping a HA scaffold with PLA film is shown in Figure 3.45, outlined in more detail in Appendix A.3 and described here in brief. Top and bottom ends (≈ 5 mm) of a freeze cast scaffold are cut off, the leftover cylinder weighed and its dimensions (diameter, length) measured with calipers. Material

density (ρ), measured mass (m), radius (r) and length (L) are used to calculate porosity with Eqns. 7 and 8:

$$\rho_{actual} = m/\pi r^2 L \quad (7)$$

$$porosity = 1 - (\rho_{actual}/\rho) \quad (8)$$

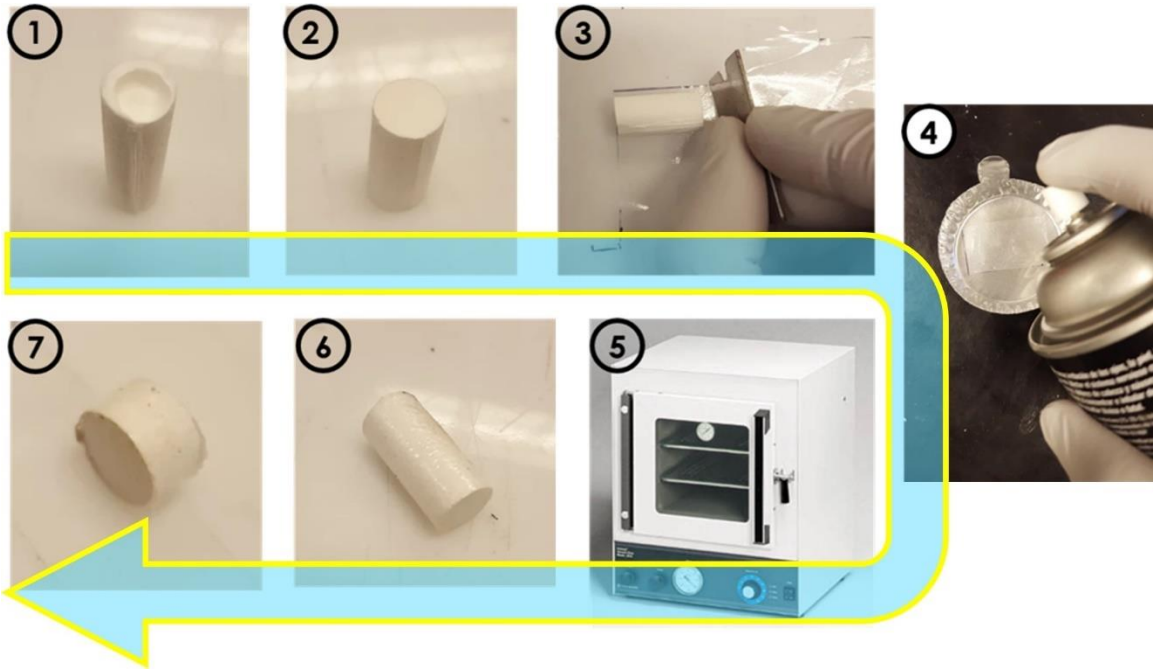

Figure 3.45: Method for preparation of porcupine quill bioinspired PLA shrink wrapped porous scaffolds.

Polylactic acid (PLA) thermopolymer film (≈ 50 µm thickness, R*PLA, Plastic Suppliers, Columbus, OH) is cut to approximately match the cylindrical dimensions for wrapping fully around the cut scaffold with an additional lip (≈ 5 mm) added to the width and to the height to wrap the cylinder completely. The cut PLA film is sprayed with an aerosol adhesive (3M™ Repositionable 75 Spray Adhesive) and wrapped around the scaffold before being placed inside a drying oven at 50 °C for ≈ 5 minutes to shrink wrap.

The Brazilian mechanical test (ASTM protocol D3967−08) is used to radially compress wrapped porous scaffolds. The thickness-to-diameter ratio (t/D) specimen range is ≈ 0.7-0.75, which is within the ASTM recommended 0.2-0.75 range. A 3342

Instron materials testing machine (Instron, Norwood, MA) with a 500 N static load cell and crosshead velocity of 0.005 mm/s is used to radially compress wrapped samples. Critical tensile strength (σ_t) is determined from measured maximum load (P), thickness (L) and diameter (D) parameters with Eqn. 9:

$$\sigma_t = 2P/\pi LD \tag{9}$$

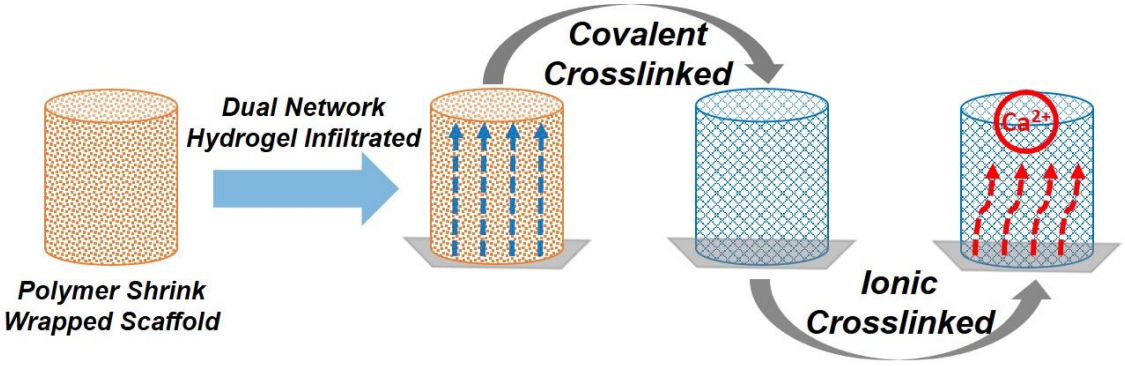

Figure 3.46: Schematic for fabrication of an exterior and interior strengthened spongy bone implant composite made of biocompatible components that can be resorbable within the body and potentially obviate the need for follow up adjustment surgical procedures that are commonplace for a titanium alloy implant.

The infiltration protocol for either PLA wrapped or non-wrapped HA scaffolds with a dual network hydrogel made up of polyethylene glycol diacrylate (PEGDA) and alginate components is shown in Figure 3.46, outlined in more detail in Appendix A.4 and described here in brief. A 2 wt% alginate solution is prepared with 2 g of sodium alginate added slowly to a stirring ≈ 75 °C solution of 100 mL distilled water. After alginate is completely dissolved, the 2 wt% solution is cooled down and stored in the fridge to avoid bacterial growth. A 1 M calcium acetate solution is made with 15.817 g of calcium acetate added to a stirring solution of 100 mL distilled water. After calcium acetate is completely dissolved, the 1 M solution is stored for later use.

PLA wrapped or non-wrapped HA scaffold pieces are cut, weighed and measured to have a thickness-to-diameter ratio (t/D) ratio ≈ 0.7-0.75, as described for the PLA wrapped scaffold protocol. HA scaffolds are seeded with calcium acetate by dipping the bottom end briefly into 1 M calcium acetate solution to wick solution up to the top by capillary force. The scaffold top appears wet and shiny after being "seeded" and the outer surface is pat dry to remove remnant calcium acetate that can form a crystalline crust after being placed inside a drying oven at ≈ 75 °C for 30 minutes.

Two 10 mL syringes are connected by a luer lock and the plunger on one side is removed to add 7 mL of 2 wt% alginate solution inside the syringe chamber. The plunger is placed back in and then the other plunger is removed to add 1 mL of 575 MW PEGDA. A 4% aqueous solution of ammonium persulfate (APS) is prepared with 500 μL added along with 50 μL of tetramethylethylenediamine (TEMED) inside the syringe chamber before the plunger is placed back in. The 8 mL hybrid hydrogel (1:8 alginate to PEGDA mass ratio), plus APS and TEMED added to covalent crosslink PEGDA, is enough to infiltrate five HA scaffolds prepared for Brazilian testing. The viscous components are mixed slowly without introducing bubbles by alternately pressing syringe plunger ends.

The mixed hybrid hydrogel is degassed in a bell vacuum at very low vacuum for 15 minutes and then calcium seeded HA scaffolds are infiltrated with the hybrid hydrogel at very low vacuum for 4 hours. PEGDA is crosslinked in the infiltrated HA scaffolds over several hours due to the previously added APS and TEMED. Alginate is fully crosslinked by submerging the infiltrated HA scaffolds into 1 M calcium acetate solution for 18 hours. The infiltrated and fully crosslinked HA scaffolds are pat dry and weighed

to determine the total added weight for all the infiltrated contents before doing Brazilian mechanical testing.

3.5.3 Mechanical Properties

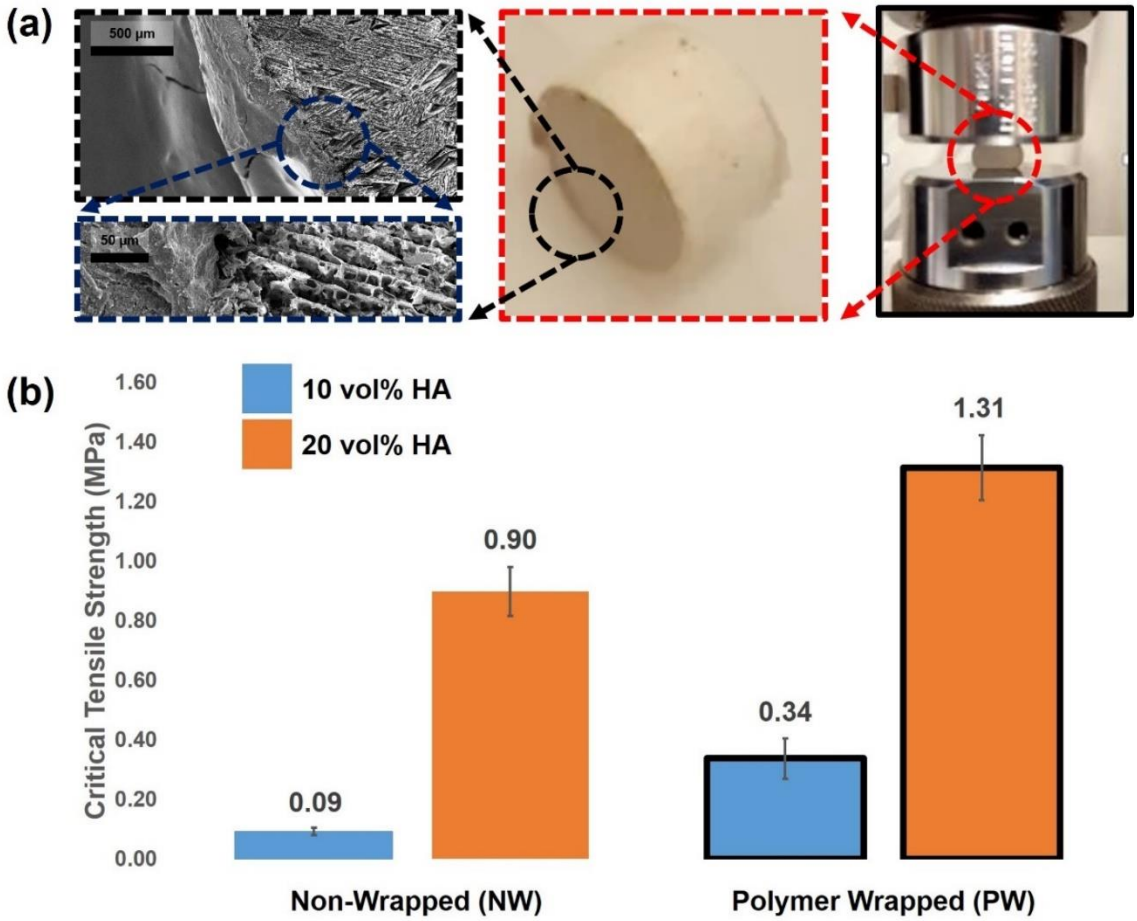

Figure 3.47: PLA wrapped (PW) scaffolds resemble a porcupine quill in SEM micrograph cross-section (a) and demonstrate enhanced strengthening versus non-wrapped (NW) scaffolds in the weak transverse axis (b).

Exterior and interior strengthened HA scaffolds were not prepared with the magnetic freeze casting methods described in Section 3.4 to isolate polymer strengthening effects (PLA shrink wrap, dual network hydrogel) as individually observable variables. PLA wrapped scaffolds resembled a porcupine quill cross-section (Figure 3.39c) and had mechanically different properties compared with typically brittle HA scaffolds subjected

to radial compression force (Figure 3.47a). The Brazilian test method used to obtain critical tensile strength values indicated that highly porous 10 vol% HA scaffolds (≈ 80-85%) shrink wrapped with PLA film were enhanced ≈ 300% while less porous 20 vol% HA scaffolds (≈ 65-70%) were enhanced ≈ 50% (Figure 3.47b). Preliminary work on the hydrogel infiltration protocol has shown promising results for calcium seeded and fully crosslinked alginate as a single network hydrogel (Figure 3.48). Further work is ongoing and a full complement of results from Brazilian testing with dual network hydrogel infiltrated PLA wrapped and non-wrapped HA scaffolds should establish clear mechanical benefits from these described exterior and interior strengthening methods.

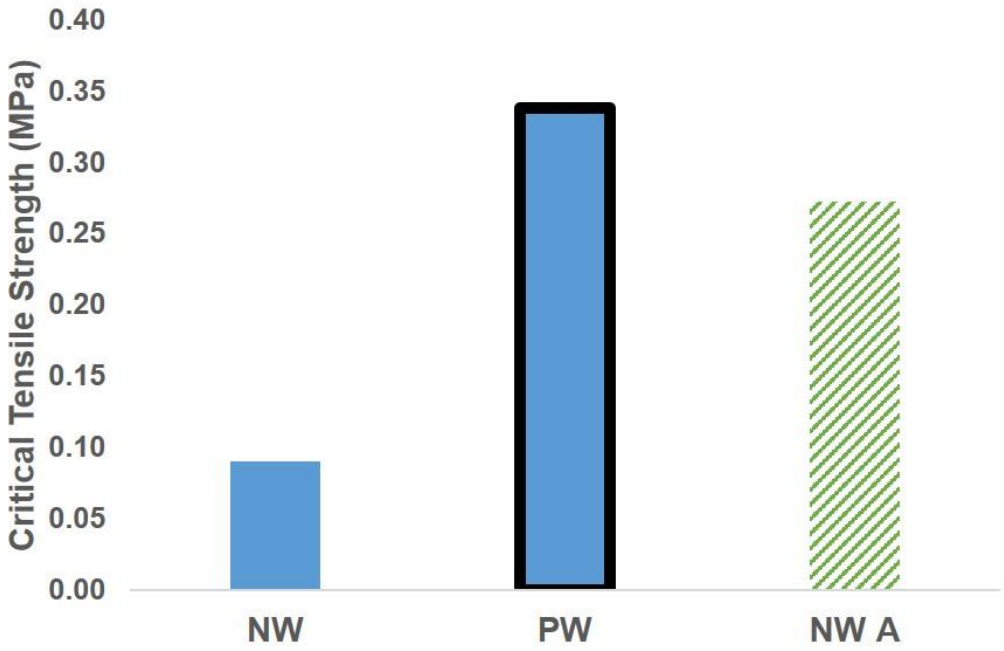

Figure 3.48: Average critical tensile strength values for non-wrapped (NW) and PLA wrapped (PW) 10 vol% HA porous scaffolds (≈ 80-85%) are compared with preliminary results for non-wrapped 10 vol% HA scaffolds infiltrated only with calcium seeded and fully crosslinked alginate single hydrogel (NW A). The NW scaffolds were enhanced ≈ 200% with infiltrated and crosslinked alginate that does not yet include additional strengthening measures from PLA wrap or crosslinked PEGDA.

The methods described herein for making exterior and interior polymer strengthened HA scaffold composites could be used for fabrication of mechanically tough

implants that resemble spongy bone mechanical properties in compression and tension. The biocompatible dual network hydrogel matrix environment within the scaffold pores could potentially promote new osteoblast ingrowth, although cell culturing and animal implant studies must be conducted to confirm any positive outcomes. This methodology for seeding porous scaffolds with components (e.g. calcium acetate) that are useful for interface connection between mineral and later infiltrated polymer layers provides a new strategy for incorporating more materials design features in freeze cast scaffolds. This could potentially enable load bearing resorbable spongy bone implants that can replace osteoporotic bone without causing stress shielding or bone remodeling like a titanium alloy.

3.5.4 Conclusions

Overall, the methodologies described herein provide a materials design strategic framework for fabricating tough spongy bone composites made of biocompatible materials that can perform well enough to potentially replace load bearing titanium alloy implants. Capillary force that wicks up "seed" components for interface connection to later infiltrated polymer can lead to new possibilities for functionalizing freeze cast scaffolds beyond spongy bone implant applications. Multi-usage and function for material components in a bioinspired experimental design can lead closer to the way natural mineral and biopolymer materials have multiple functions which complement each other within a total structure.

Chapter 3, in part, is published as "Stiff, porous scaffolds from magnetized alumina particles aligned by magnetic freeze casting" Materials Science and Engineering: C, 77, 484-492, 2017. This work was coauthored by S. E. Naleway, T. Haroush, C-H Liu, S. H. Siu, J. Ng, I. Torres, A. Ismail, K. Karandikar, M. M. Porter, O. A. Graeve and J. M. McKittrick. The dissertation author is the first author of this work.

Chapter 3, in part, is accepted as “Synergistic structures from magnetic freeze casting with surface magnetized alumina particles and platelets” Journal of the Mechanical Behavior of Biomedical Materials, Published Online, 2017. This work was coauthored by S. H. Siu, K. Karandikar, C-H Liu, S. E. Naleway, M. M. Porter, O. A. Graeve and J. McKittrick. The dissertation author is the first author of this work.

Chapter 3, in part, is in progress as “Biodegradable Spongy Bone Implants: Strength Through Bioinspiration,” 2017. This work will be coauthored by A. Ismail, C. Ayala, L. Guibert, K. Karandikar, C-H Liu, S. H. Siu, J. Mok, J. Ng, O. A. Graeve and J. McKittrick. The dissertation author will be the first author of this work.

CHAPTER 4: CONCLUSIONS AND FUTURE RESEARCH WORK

4.1 Bioinspiration: How Everything Ties Together

The path towards bioinspiration is not always clear and certainly not linear. The protocol described in Chapter 2 for the bioinspired Aristotle's lantern sediment sampler began with the biology and observation of pink sea urchins in nature. The next step was characterization of the biological components using non-invasive methods such as micro-CT to examine the Aristotle's lantern structure as well as extracting and embedding the teeth in epoxy to examine the microstructural components with SEM. The following step was an iterative bioinspired design for a sediment sampler that could go beyond biomimicry to perform functionally better than the natural structure from which its underlying mechanism was derived. This result was not the end of the story, however, since implementation of the final bioexploration step was possible through application of finite element engineering analysis methods that could help explain the purpose of the keel structure for reinforcement of the tooth grinding tip. Connections to be made from bioinspiration back to biology necessitates wading into unfamiliar territory by embarking on a bioexploration step.

Bioinspiration from spongy bone began with an observation that porous scaffolds made by ice templating (typically identified as freeze casting, as will be done here) resembles porosity in the cancellous layer of bone. But, freeze casting by itself produces porosity alignment in only a single ice growth axis and the overall mechanical properties of the structure are poor in any axis transverse to the ice growth axis. Magnetic freeze casting began with the premise that lamellar wall alignment in the transverse axis was

possible when mixing weakly paramagnetic materials together with ferromagnetic magnetite nanoparticles [1]. The alignment and strengthening effect observed in initial magnetic freeze casting work was isolated to slurry mixtures which depended on a significantly increased proportion of ferromagnetic materials to align along lamellar walls with weakly paramagnetic titania [1] or along mineral bridges perpendicular to diamagnetic zirconia [4].

The magnetic freeze casting work described herein addressed limitations from past magnetic freeze casting work that was specific to mixtures with weakly paramagnetic materials or strongly ferromagnetic ones. Surface magnetization of any particle type in water was first demonstrated using a surface chemistry electrostatic adsorption principles. The toolbox of potential structural materials that could be used for further magnetic freeze casting work was then opened completely. The next levels of complexity to address experimentally were understanding the magnetic freeze casting system beyond empirical observation alone so that porous scaffolds with enhanced mechanical properties could be tailored for specific structural applications such as multi-axis strengthened bone implants.

The first step towards that end goal was using theoretical equations to predict how different particle sizes affect chain formation and aggregation to make aligned lamellar walls during magnetic freeze casting. The extent of alignment was determined through scaffold cross-section characterization with SEM and through mechanical compression of cubes along different transverse, magnetic field and ice growth directions. The first result confirmed that all other things being the same, larger surface magnetized particles subjected to an appropriately weak applied magnetic field gradient could align lamellar walls in the scaffold center.

The next step built upon this knowledge abut particle size and applied it to varying morphology, specifically large high aspect ratio platelets made of the same alumina material. Interestingly, ratios of particle and platelet morphology had a huge impact on aggregation of components within the slurry during magnetic freeze casting that led to overall lamellar wall alignment. An equal ratio of dissimilar morphology materials in fact cancelled alignment dominance out for both. There was also a relationship to be extended to templated grain growth (TGG) systems whereby a small proportion of high aspect ratio platelets is sufficient to guide grain growth for making textured ceramic materials.

Finally, the last experimental step to take was to bring magnetic freeze casting back to its initial purpose for guiding development of bioinspired bone implants. Besides the multi-axis strengthening of the mineral phase enabled by magnetic freeze casting, the true end goal was development of an experimental design which could enable fabrication of a toughened composite that resembles spongy bone. The threshold to be reached would be a composite structure that could mimic the unique mechanical properties of bone while also promoting new osteoblast ingrowth to enable the implant to be resorbable.

Magnetic freeze casting with surface magnetized HA, along with scaffold PLA shrink wrapping and infiltration of a tough dual network hydrogel that binds the internal lamellar walls of the porous scaffold, could potentially address these fundamental needs for new spongy bone implants. Future research and development will need to focus on making magnetic freeze cast scaffolds with mechanical properties that are much more predictable and functional for potential use as biomedical implants within multi-phase clinical trials that require highly rigorous control over consistent design and fabrication specifications [69].

4.2 Future Research Work: Ceramic Water Filtration

Sir Henry Doulton invented the modern ceramic water filter in 1827 and was later commissioned by Queen Victoria to produce one for her personal use in 1835 [170]. Ceramic water filters became popular for preventing and treating contaminated water during the 1840s (Figure 4.1a). Research by Louis Pasteur during the 1850s validated that bacteria were isolated and trapped due to size selection factors associated with the ceramic porosity. Generally, bacteria, protozoa, and microbial cysts can be removed by ceramic water filters, although viruses are small enough to pass through the pores to the clean side of the filter. Adsorption of colloidal silver particles within ceramic filter pores can provide additional anti-microbial effect, while activated carbon enclosed within a ceramic filter cartridge can reduce organic and metallic contaminants (Figure 4.1b). Major issues with ceramic water filtration stem from development of hairline cracks in the brittle, porous ceramic that can lead to cross-contamination or the clean water side of the ceramic filter coming into contact with dirty water, hands, cleaning cloths, etc. [170].

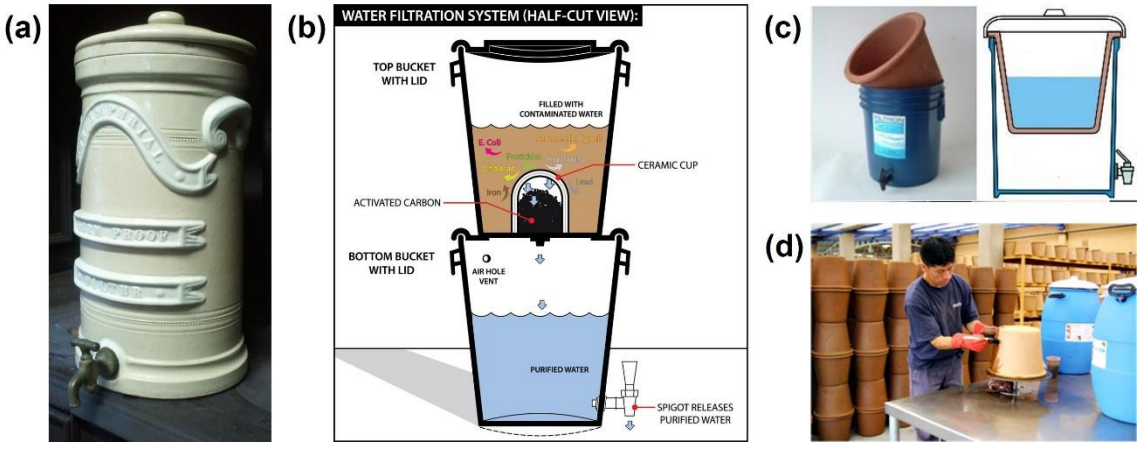

Figure 4.1: An example of a Victorian era ceramic water filter (a), a ceramic water filtration unit that uses a replaceable activated carbon core (b) and a ceramic pot water filtration unit developed through Potters for Peace (c) that has an option for added anti-microbial functionality when colloidal silver is painted on the outside (d). Images taken from [170-172].

Briefly mentioned in Section 3.3, ceramic water filtration devices have been promoted lately for sustainable production and use in rural or economically disadvantaged environments throughout the world. This recent trend began in 1981 when Fernando Mazariegos invented a new ceramic pot water filter technology at the Central American Research Institute in Guatemala City [170]. One of his students was an American, Ron Rivera, who went on to start Potters for Peace, a non-profit organization that helps developing communities around the world make ceramic pot water filters (Figure 4.1c) for themselves. An additional colloidal silver layer functionality (Figure 4.1d) can also be added to ensure production of cheap and high quality potable water.

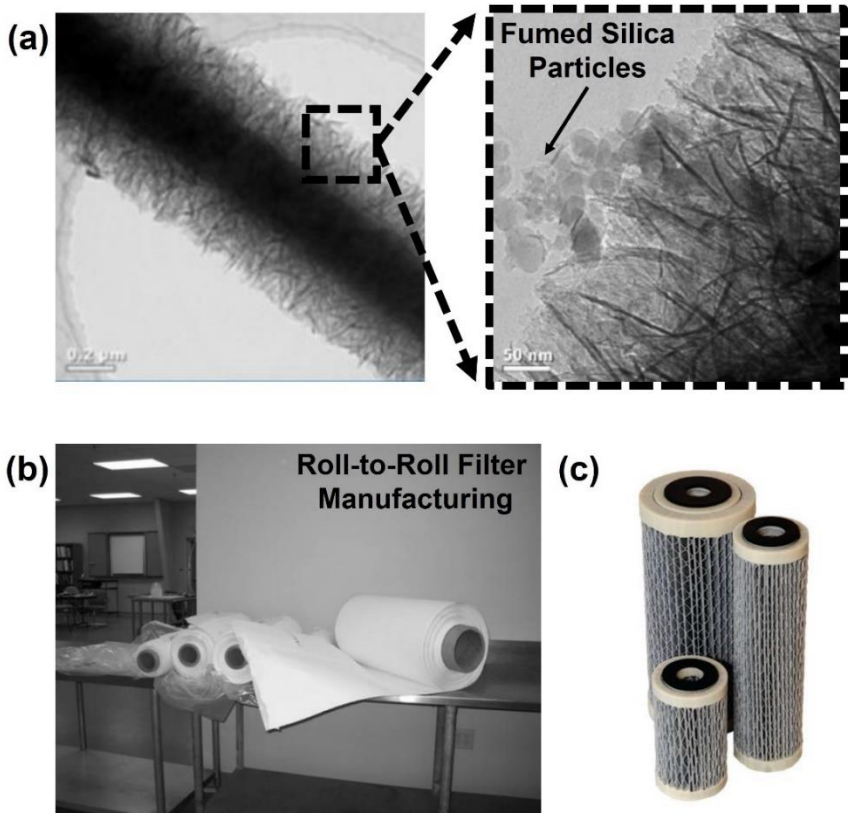

Figure 4.2: NanoCeram technology has glass fibers functionalized with electropositive alumina nanowires that can attract small virus-like particles similar in size to fumed silica (a). Roll-to-roll manufacturing (b) allowed for scale up to make commercially available water filtration units (c). Images taken from [173-175].

Argonide is a Florida based company which developed a ceramic water filtration membrane technology called NanoCeram. Developed in collaboration with NASA, the high throughput water filtration unit has been used by astronauts onboard the International Space Station (ISS). NanoCeram technology uses glass fibers functionalized with high surface area alumina nanowires (Figure 4.2a) that are dispersed in a non-woven membrane with micron scale porosity (Figure 4.2b). The large pore size allows for high fluid throughput, while the electropositive alumina nanowires have large surface area to attract negatively charged bacteria and other contaminants in units with multiple membrane layers (Figure 4.2c).

As mentioned in Section 3.5, HA porous scaffolds can be used as a framework to wick up a "seed" layer (e.g. calcium acetate) that binds to interior scaffold walls (e.g. phosphate in HA) and can further crosslink other infiltrated components (e.g. alginate in a dual network hydrogel) to make uniquely multifunctional composites for complex applications (e.g. spongy bone implants). In a similar way, alumina freeze cast scaffolds can wick up a first "seed" layer of dispersed alumina nanowires, get sintered again to have electropositive nanowire studded interior scaffold walls and then wick up a second "seed" layer of colloidal silver nanoparticles to adsorb onto the alumina nanowires for an enhanced anti-microbial effect (Figure 4.3). In comparison with NanoCeram, this type of alumina filtration scaffold has a few advantages, such as micron scale porosity with electropositive alumina nanowires that have more overall surface area throughout the cylindrical scaffold compared with a membrane and its potential use with high pressure fluid filtration applications (e.g. environmental remediation of wastewater) since fluid flow porosity is aligned in the ice growth direction (*z*-axis) with excellent mechanical properties.

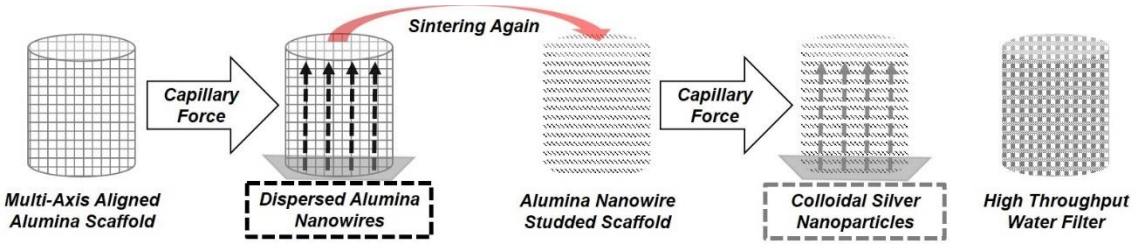

Figure 4.3: Schematic diagram for using alumina porous scaffolds as a framework to wick up "seed" components such as alumina nanowires and colloidal silver nanoparticles to impart added ceramic water filtration functionality within alumina porous scaffolds.

This functionalized alumina scaffold could be attached as part of a spigot onto ceramic pot water filters made by Potters for Peace. This application would provide an additional layer of protection from potential cross-contamination due to hairline fractures in the main ceramic pot water filter unit or contamination of the spigot itself. The functionalized alumina scaffold with colloid silver could even be taken out and heated to temperature above bacteria and microbe survival to easily sterilize the unit between uses. This could potentially provide a solution that Potters for Peace could promote as an add on filtration feature to account for potential contamination in either the ceramic pot water filter or the spigot.

4.3 Future Research Work: Magnetic Colors Bioinspired by Cuttlefish

The chromatophore organ in cephalopods (Figure 4.4a) has a complicated structure which alternates between retraction-relaxation and expansion-contraction states to generate the appearance of wave-like mobile color movement throughout the surface of the animal body (Figure 4.4b). Chromatophores can display very different pattern appearances with pigments that reflect longer waves of the visible electromagnetic spectrum to end up with colors such as yellow, orange, brown and red (Figure 4.4c). Many color changing processes are not yet fully understood, especially in the case of highly complex patterning of color and texture in cephalopods such as cuttlefish.

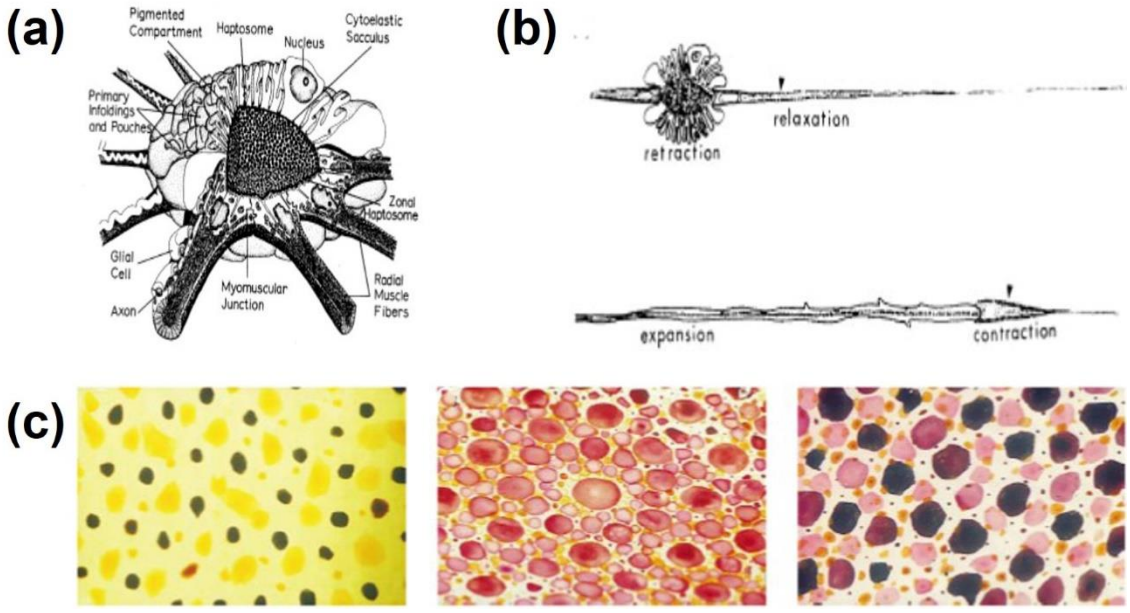

Figure 4.4: A schematic of a squid chromatophore based on observations from electron microscopy (a), vertical section through a retracted and expanded chromatophore that shows a radial muscle in relaxed and contracted states. Images taken from [176].

The same method used to surface magnetize alumina and HA particles can be applied to magnetize mineral based pigments used by artists for making paints. The mineral (e.g. calcite) has dye molecules covalently attached to it that give the appearance of color. A small amount of superparamagnetic magnetite can magnetize the pigment noticeably affecting the color appearance. The mobile striping pattern along the body of the flamboyant cuttlefish (Figure 4.5a) is especially striking among cephalopods and provides an excellent bioinspired animal model for development of magnetic colors. Various pigments were surface magnetized and a SEM micrograph shows a closer look for one of them at the functionalized mineral surface (Figure 4.5b). A potential application could be to encapsulate a mixture of magnetic pigment (e.g. red) and non-magnetic pigment (e.g. yellow) that appears as a mixed color in a thin film (Figure 4.5c), which could then sweep reversibly between color component parts within a magnetic color changing wall panel.

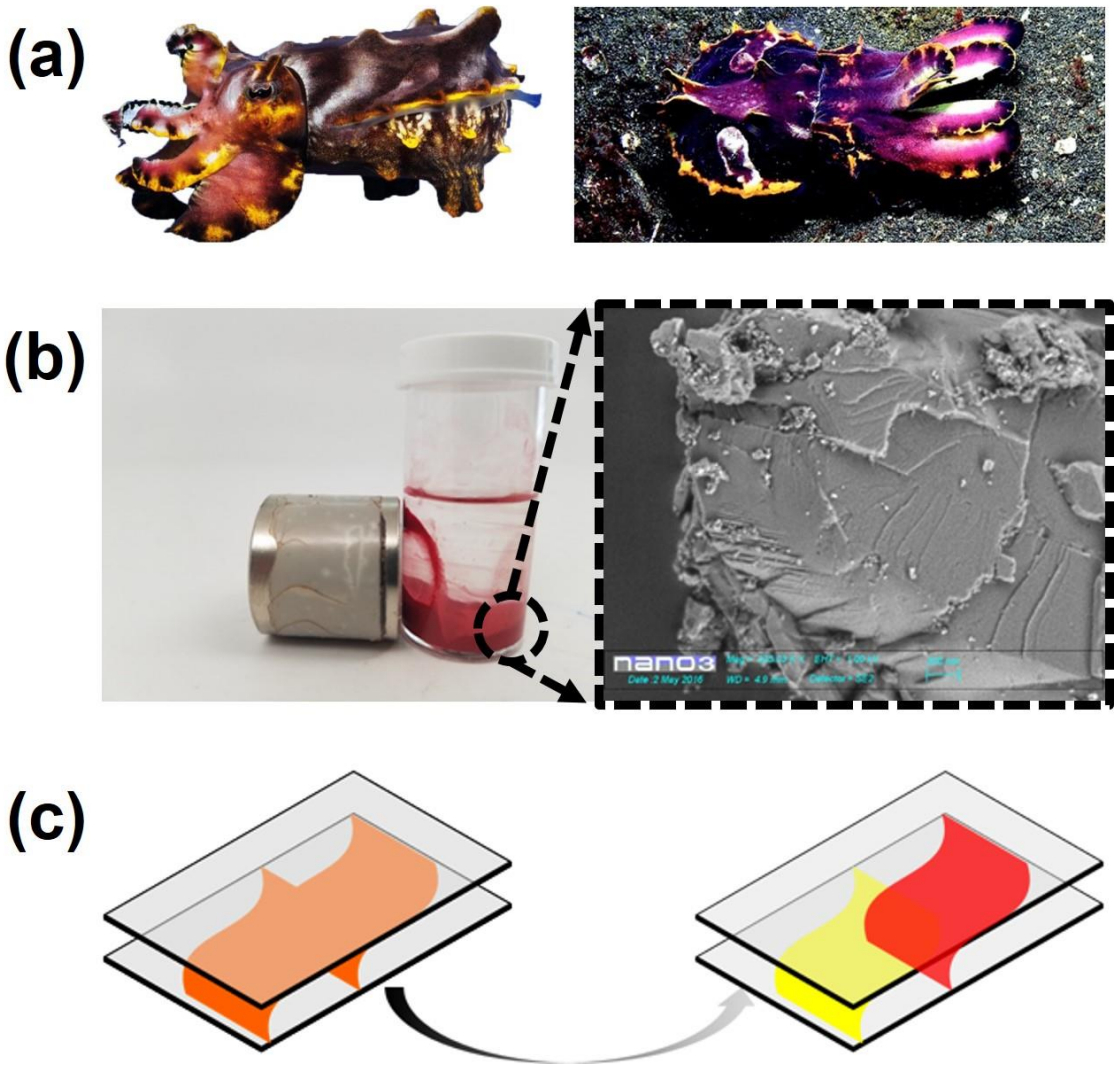

Figure 4.5: The unique appearance of a flamboyant cuttlefish (a) which bioinspired surface magnetization of mineral based pigments to make magnetic colors (b) that may be used within an encapsulated thin film for magnetic color changing wall panels. Images taken from [177, 178].

Beyond color changing demonstrations (Figure 4.6a), surface magnetized materials also can have texture changing applications bioinspired by flamboyant cuttlefish. Magnetized silica in water can aggregate into a gel from an applied magnetic field (Figure 4.6b). Additionally, silica can be colorized purple with a small amount of basic dye (e.g. crystal violet) before being surface magnetized with superparamagnetic magnetite nanoparticles (Figure 4.6c). Use of colorized and magnetized silica particles mixed together with non-colorized and non-magnetized silica could provide both color and texture

changing functionality that is bioinspired by the more complex color and texture changing natural mechanism demonstrated in flamboyant cuttlefish.

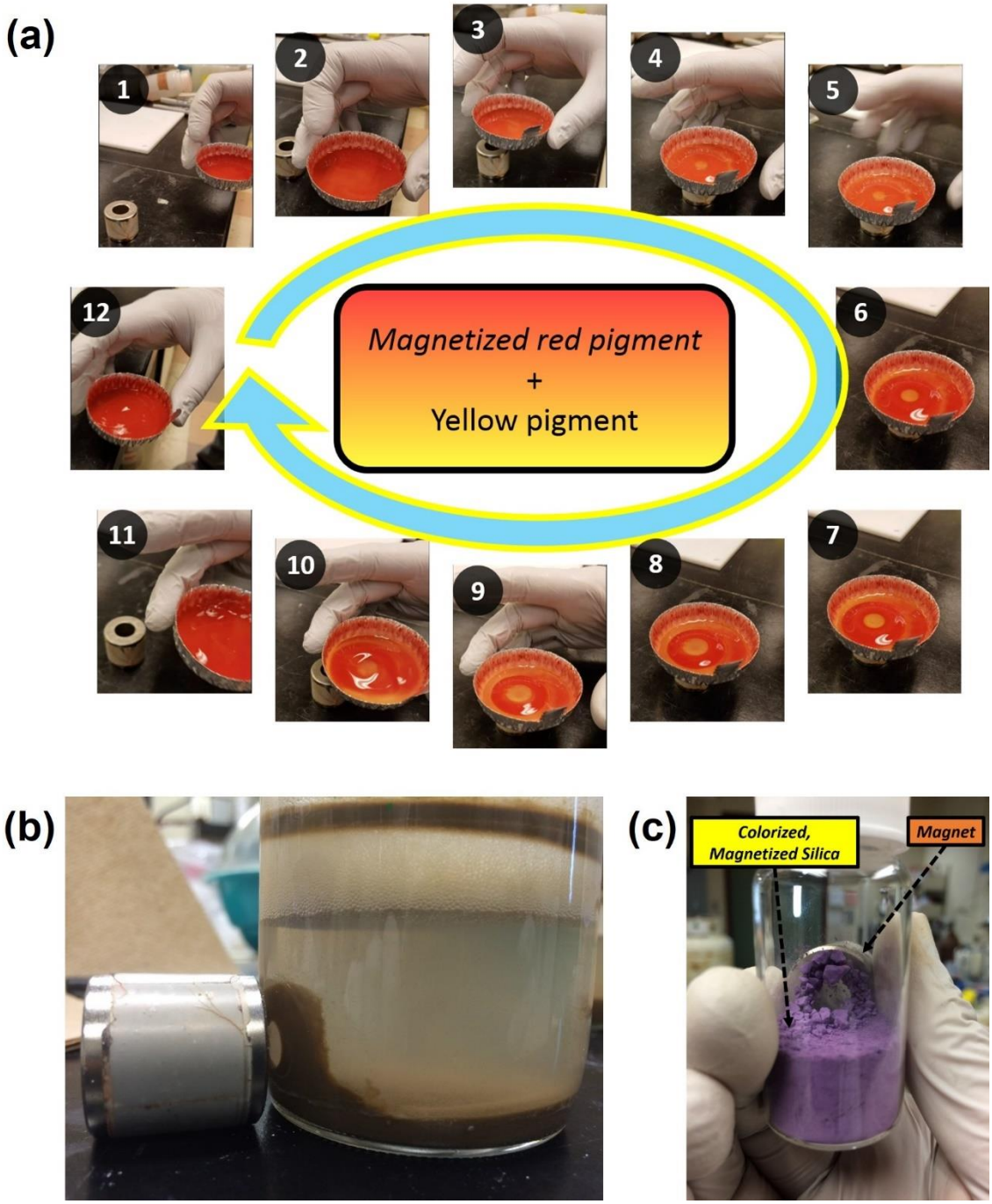

Figure 4.6: Surface magnetized red pigment mixed with non-magnetized yellow pigment to make an orange mixture can be reversibly separated with an applied magnet field (a). Magnetized silica particles aggregate reversibly in water (b) and can be colorized before being magnetized to end up with both color and texture changing functionality.

APPENDIX

A.1 Materials Magnetization Protocol

1. Weigh 2.5 g of alumina in an aluminum tray and keep in drying oven to prevent atmospheric water adsorption to the surface of the hygroscopic powder material.

2. Prepare a container with 75 mL distilled water and a stir bar. Place on a stir plate and increase stir speed until a vortex is visible touching the container bottom.

3. Remove alumina powder from drying oven and pour slowly into the stirring water. Avoid particle accumulation on side walls that may not get magnetized.

4. Stir alumina solution and prepare a centrifuge tube with 25 mL distilled water.

5. Add 0.1 mL of ferrofluid (EMG-705 for alumina) to the 25 mL distilled water. Use a transfer pipet to mix contents by squeezing the plastic bulb several times.

6. Use a transfer pipet to dropwise add diluted ferrofluid solution to the mixing alumina. Double check side walls to ensure no white alumina particles are aggregated and not being magnetized. The solution will change to coffee colored.

7. Stir mixture ≈ 6 hours to ensure total magnetization. Check for completion by turning off stirrer, waiting for particles to settle to the bottom and observing if the liquid above the particles is clear and no longer colored brown or black.

8. Remove stir bar and set up vacuum filtration with a large filter flask, vacuum adapter, Buchner funnel, and corresponding sized filter paper. Hook up the vacuum line to the filter flask, place the filter paper on the Buchner funnel and

turn on the vacuum first before wetting the filter paper stuck to the Buchner funnel with water to ensure a good seal.

9. Swirl to redisperse the magnetized alumina solution and add to the Buchner funnel. Use a squirt bottle to rinse magnetized particles from the bottom of the container. Foamy bubbles on side walls is surfactant, not particles, so this need not be rinsed and added to the Buchner funnel.

10. Use one full squirt bottle for every 4-5 containers to ensure all surfactant is completely rinsed off the magnetized particles. Carefully wipe away foamy bubbles from the Buchner funnel side walls.

11. Place aluminum foil on top of the Buchner funnel, poke holes in the top, and dry overnight in drying oven before transferring to a storage container for later use.

A.2 Freeze Casting and Magnetic Freeze Casting Protocols

1. Remove the plastic bottle which contains alumina grinding media and slurry components from the ball mill after 24 hours set at 15-16 on dial.

2. Using the cap to cover the bottle opening, avoid pouring out alumina balls while pouring out ≈ 15 mL slurry portions into separate 50 mL centrifuge tubes.

3. Stretch wrap centrifuge tube tops with Parafilm, poke two holes in top and place upright in Styrofoam holders to put in the bell vacuum. Add grease around the lid to ensure a good seal and confirm vacuum inlet valve is closed. Turn on vacuum, open valve and slowly open vacuum inlet port. Run vacuum for 15-20 minutes.

4. Turn on the power strip and flip both switches to the freeze casting control box. Press the furthest right button twice and furthest left button once to start a countdown of 10 minutes (display shows “00 09” to indicate start from 9 minutes and 59 seconds).

5. Pour liquid nitrogen into the Styrofoam container to the top black line on outside. Place Styrofoam lid on top to slow evaporation.

6. Wipe off copper finger top with a Kim Wipe and apply a small amount of Vaseline onto it. Wipe off copper coin with a Kim Wipe and apply with striated side down (polished side up) onto copper finger top.

7. Wipe off the inside of the medium sized PVC mold with a Kim Wipe and apply a uniformly thick layer along the edges of the smooth mold end. Place Vaseline applied side down onto the copper coin and make sure the Vaseline seal is good along all edges, but not covering too much of the copper coin.

8. Close the valve and turn off the switch for the vacuum at “00 03” on the display, which indicates more than 3 minutes are left on the countdown. Open the vacuum inlet port and remove degassed centrifuge tubes. Keep the centrifuge tube in the Styrofoam holder with cap on and place on shaker until “00 01” is on the display.

9. Carefully swirl the degassed slurry slowly and pour it into a medium sized plastic mold only up to the top tape edge (since pouring higher won’t freeze anyway). Transfer copper finger lid to Styrofoam container with liquid nitrogen and press lid down on all sides.

10. *For magnetic freeze casting*, set the magnetic field gap between the bar magnets using a digital caliper and then place the rig carefully around the slurry in the mold. Make sure the rig is oriented properly along the magnetic field direction.

11. Freeze casting starts when the display reaches “00 00” and then a new countdown of 18 minutes starts from 10 °C down to -170 °C (-10 °C per minute). Once the display reaches “00 00” again, a new countdown of 3 hours starts with “02 59” on the display. Samples are all done freeze casting at “02 30” or less on the display.

12. Label a small plastic tray with the date, slurry material vol%, magnetic field and sample number. Remove the mold that has the freeze cast sample within it from the copper finger and transfer the lid back to the empty Styrofoam container. Turn the control box two switches off/on to start warming up the copper cold finger.

13. Warm the frozen plastic mold by rubbing in your gloved hand for several minutes. Take out a small alumina crucible from the freezer and place it onto a labeled plastic tray. Use the freeze casting plunger tool (scalpel metal rod base standing upright that has been fixed in an epoxy filled plastic cap) to push out the freeze cast sample. Generally, the frozen sample can be extracted when the temperature setting on the display indicates the freezing stage has warmed up to ≈ -100 °C.

14. After the freeze cast sample is pushed out, quickly transfer it into the frozen alumina crucible with the pushed in end visible sticking up at the top. Leave it in the freezer until it is time to transfer all the samples at the same time to the sufficiently cooled down freeze dryer. Rinse the plastic mold and plunger tool.

15. Turn the control box two switches off/on again when the temperature display is at ≈ -50 °C, then press the furthest right button twice and the furthest left button once to start a new countdown of 10 minutes (display shows “00 09”).

16. Once the temperature reaches ≈ 0 °C, the copper coin and copper cold finger can be wiped off with Kim Wipes. Refill the liquid nitrogen up to the indicated line near the container top, reapply Vaseline to the bottom side of the coin in contact with the copper rod and along the inside walls plus bottom rim of the PVC mold, adjust the magnet gap distance (if needed), redisperse any sedimented slurry within the centrifuge tube using a thin wood stick and pour in the next sample.

17. Redisperse the slurry contents between freeze casting trials before pouring into the PVC mold to get samples with consistent slurry vol% and scaffold porosity.

A.3 Thermopolymer Shrink Wrap Protocol

1. Cut off scaffold top and bottom ends (≈ 5 mm) using a sectioning saw to leave behind only the middle section of the scaffold with the most uniform porosity.
2. Weigh the scaffold and measure cylinder dimensions (diameter, length) with calipers. Material density (ρ), measured mass (m), radius (r) and length (L) are used to calculate porosity using the below equations:

$$\rho_{actual} = \frac{m}{\pi r^2 L} \qquad porosity = 1 - \frac{\rho_{actual}}{\rho}$$

3. Cut a rectangular piece of polylactic acid (PLA) thermopolymer (≈ 50 μm thickness, R*PLA, Plastic Suppliers, Columbus, OH) with a new razor blade to approximately match the cylindrical dimensions for wrapping fully around the cut

scaffold. The sheet length should be the same as the cylinder height measured in the prior step (indicated as length, *L*). The sheet width requires solving for the cylinder lateral surface area ($A_l = 2\pi rh$), then using that area to determine sheet width ($w = A_l / h$). An additional lip (≈ 5 mm) should be added to the width and to the height to wrap the cylinder dimensions completely.

4. Use a disposable aluminum tray flipped over with the cut thermopolymer sheet laying down flat on top. Spray a few times with an aerosol adhesive (3M™ Repositionable 75 Spray Adhesive) and wrap the PLA film around the scaffold.
5. Place the wrapped scaffold inside a drying oven at 50 °C for ≈ 5 minutes to allow the wrap to shrink and laminate tightly around the scaffold.
6. Prepare the wrapped scaffold for Brazilian mechanical test with ASTM protocol (D3967−08). Thickness (cylinder height, indicated as length, *L*)-to-diameter ratio (t/D) for a specimen must be between 0.2-0.75, but aim for 0.7-0.75 to match prior experiments. Mark cut points on the wrapped scaffold to obtain 2-3 samples.
7. Use the sectioning saw to cut the scaffold into samples with the proper final thickness. Work carefully to avoid frayed edges or delamination of the wrap that may unseal or adversely affect subsequent Brazilian testing results. Remeasure cylinder dimensions (diameter, length) for each cut sample with calipers to obtain thickness-to-diameter ratio (t/D) values for critical tensile strength calculation.
8. Use a 3342 Instron materials testing machine (Instron, Norwood, MA) with a 500 N static load cell at a crosshead velocity of 0.005 mm/s to radially compress wrapped samples. Determine critical tensile strength (σ_t) with the below equation using max load (*P*), thickness (*L*) and diameter (*D*): $\sigma_t = \frac{2P}{\pi LD}$

A.4 Alginate and PEGDA Dual Network Hydrogel Infiltration Protocol

1. Add 2 g sodium alginate a small amount at a time (to avoid clumping) to a stirring ≈ 75 °C solution of 100 mL distilled water until it completely dissolves. Cool down and store the 2 wt% alginate solution in the fridge to avoid bacterial growth.
2. Add 15.817 g calcium acetate to 100 mL distilled water to make a 1 M calcium acetate solution that can be stored for later use.
3. Weigh the cut scaffold pieces with already measured thickness-to-diameter ratio (t/D = 0.7-0.75) dimensions before any infiltration occurs.
4. Place a small amount (1-2 mL) of 1 M calcium acetate solution in a plastic tray and dip the scaffold bottom for a second to wick solution up by capillary force. The scaffold top will appear shiny and is now "seeded" with calcium acetate.
5. Use a Kim Wipe to pat dry the outer scaffold surface to remove any remnant calcium acetate that may form a crystalline crust bound to phosphate in HA on the outside of the scaffold. Place the calcium acetate seeded scaffolds in a drying oven at ≈ 75 °C for at least 30 minutes.
6. Use two 10 mL luer lock connected syringes as a viscous fluid mixing system. Add 7 mL of 2 wt% alginate solution to one syringe port with piston removed, then close that port and open the other syringe port with piston removed to add 1 mL of 575 MW PEGDA. Add APS (4% aqueous solution, 500 μL) and TEMED (50 μL) to 8 mL hybrid hydrogel, which is enough for infiltration of 5 scaffolds.
7. Mix the viscous components together without introducing bubbles by pressing slowly on one syringe end while the other piston pops up. The alginate : PEGDA

(1:8) hybrid hydrogel has 7 mL of 2 wt% alginate solution (0.14 g alginate) which is an eighth by mass of 1 mL of 575 MW PEGDA (1.12 g PEGDA).

8. Degas hybrid hydrogel in a beaker within a bell vacuum at very low vacuum for 15 minutes. Watch out for the hybrid hydrogel climbing the walls and out of the beaker. Dip the calcium seeded scaffold bottom in the hybrid hydrogel and use a very low vacuum to slowly infiltrate the porous scaffold for 4 hours.
9. Completely submerge the PEGDA cured scaffolds with infiltrated hybrid hydrogel in 1 M calcium acetate for 18 hours to fully crosslink the alginate.
10. Afterwards pat dry and weigh the infiltrated scaffold to determine the total added weight for all the infiltrated contents.
11. Prepare the fully cured alginate and PEGDA hybrid hydrogel infiltrated scaffold with or without polymer wrap for Brazilian mechanical test with ASTM protocol (D3967−08). Use a 3342 Instron materials testing machine (Instron, Norwood, MA) with a 500 N static load cell at a crosshead velocity of 0.005 mm/s to radially compress wrapped samples. Determine critical tensile strength (σ_t) with the below equation using max load (P), thickness (L) and diameter (D): $\sigma_t = \frac{2P}{\pi LD}$

REFERENCES

[1] M.M. Porter, M. Yeh, J. Strawson, T. Goehring, S. Lujan, P. Siripasopsotorn, M.A. Meyers, J. McKittrick, Magnetic freeze casting inspired by nature, Mater. Sci. Eng. A-Struct. Mater. Prop. Microstruct. Process. 556 (2012) 741-750.

[2] M.M. Porter, Thesis: Bioinspired Design: Magnetic Freeze Casting, Materials Science and Engineering Program, University of California, San Diego, 2014, p. 242.

[3] M.M. Porter, L. Meraz, A. Calderon, H.J. Choi, A. Chouhan, L. Wang, M.A. Meyers, J. McKittrick, Torsional properties of helix-reinforced composites fabricated by magnetic freeze casting, Composite Structures 119 (2015) 174-184.

[4] M.M. Porter, P. Niksiar, J. McKittrick, Microstructural control of colloidal-based ceramics by directional solidification under weak magnetic fields, Journal of the American Ceramic Society (2016).

[5] R.M. Erb, R. Libanori, N. Rothfuchs, A.R. Studart, Composites reinforced in three dimensions by using low magnetic fields, Science 335(6065) (2012) 199-204.

[6] R.K. Nalla, J.J. Kruzic, R.O. Ritchie, On the origin of the toughness of mineralized tissue: microcracking or crack bridging?, Bone 34(5) (2004) 790-798.

[7] R.O. Ritchie, M.J. Buehler, P. Hansma, Plasticity and toughness in bone, Phys. Today 62(6) (2009) 41-47.

[8] Y. Seki, M.S. Schneider, M.A. Meyers, Structure and mechanical behavior of a toucan beak, Acta Mater. 53(20) (2005) 5281-5296.

[9] L. Feng, S.H. Li, Y.S. Li, H.J. Li, L.J. Zhang, J. Zhai, Y.L. Song, B.Q. Liu, L. Jiang, D.B. Zhu, Super-hydrophobic surfaces: From natural to artificial, Advanced Materials 14(24) (2002) 1857-1860.

[10] T.L. Sun, L. Feng, X.F. Gao, L. Jiang, Bioinspired surfaces with special wettability, Accounts Chem. Res. 38(8) (2005) 644-652.

[11] X.J. Feng, L. Jiang, Design and creation of superwetting/antiwetting surfaces, Advanced Materials 18(23) (2006) 3063-3078.

[12] E. Arzt, Biological and artificial attachment devices: Lessons for materials scientists from flies and geckos, Mater. Sci. Eng. C-Biomimetic Supramol. Syst. 26(8) (2006) 1245-1250.

[13] A.K. Geim, S.V. Dubonos, I.V. Grigorieva, K.S. Novoselov, A.A. Zhukov, S.Y. Shapoval, Microfabricated adhesive mimicking gecko foot-hair, Nature Materials 2(7) (2003) 461-463.

[14] E. Munch, M.E. Launey, D.H. Alsem, E. Saiz, A.P. Tomsia, R.O. Ritchie, Tough, Bio-Inspired Hybrid Materials, Science 322(5907) (2008) 1516-20.

[15] M.E. Launey, E. Munch, D.H. Alsem, H.B. Barth, E. Saiz, A.P. Tomsia, R.O. Ritchie, Designing highly toughened hybrid composites through nature-inspired hierarchical complexity, Acta Mater. 57(10) (2009) 2919-2932.

[16] M.E. Launey, E. Munch, D.H. Alsem, E. Saiz, A.P. Tomsia, R.O. Ritchie, A novel biomimetic approach to the design of high-performance ceramic-metal composites, J. R. Soc. Interface 7(46) (2010) 741-753.

[17] F. Jelínek, G. Smit, P. Breedveld, Bioinspired Spring-Loaded Biopsy Harvester—Experimental Prototype Design and Feasibility Tests, Journal of Medical Devices 8(1) (2014) 015002.

[18] F. Jelínek, J. Goderie, A. van Rixel, D. Stam, J. Zenhorst, P. Breedveld, Bioinspired Crown-Cutter—The Impact of Tooth Quantity and Bevel Type on Tissue Deformation, Penetration Forces, and Tooth Collapsibility, Journal of Medical Devices 8(4) (2014) 041009.

[19] M. Reich, A.B. Smith, Origins and biomechanical evolution of teeth in echinoids and their relatives, Palaeontology 52(5) (2009) 1149-1168.

[20] C.E. Killian, R.A. Metzler, Y. Gong, T.H. Churchill, I.C. Olson, V. Trubetskoy, M.B. Christensen, J.H. Fournelle, F. De Carlo, S. Cohen, J. Mahamid, A. Scholl, A. Young, A. Doran, F.H. Wilt, S.N. Coppersmith, P.U.P.A. Gilbert, Self-Sharpening Mechanism of the Sea Urchin Tooth, Advanced Functional Materials 21(4) (2011) 682-690.

[21] P. Trogu, Bionics and Design: Pure and Applied Research, Living Machines 2014: 3rd International Conference on Biomimetics and Biohybrid Systems Barcelona, Spain (2014).

[22] G. Scarpa, Modelli di Bionica, Capire la Natura Sttraverso i Modelli Bologna, Italy (1985).

[23] M.M. Porter, Adriaens D., Hatton R.L., Meyers M.A., M. J.M., Bioexploration: How engineering designs help elucidate the evolution of seahorse tails., SICB Annual Meeting, Society for Integrative and Comparative Biology West Palm Beach, FL (2015).

[24] Y. Ma, B. Aichmayer, O. Paris, P. Fratzl, A. Meibom, R.A. Metzler, Y. Politi, L. Addadi, P.U. Gilbert, S. Weiner, The grinding tip of the sea urchin tooth exhibits exquisite control over calcite crystal orientation and Mg distribution, Proc Natl Acad Sci U S A 106(15) (2009) 6048-53.

[25] A. Witze, NASA plans Mars sample-return rover, Nature 509(7500) (2014) 272.

[26] A. Witze, Mars rover facing harshest journey yet, Nature News Blog July 17 (2014).

[27] A. Witze, NASA announces instruments for 2020 Mars rover, Nature News Blog July 31 (2014).

[28] M.B. Frank, S.E. Naleway, T.S. Wirth, J.Y. Jung, C.L. Cheung, F.B. Loera, S. Medina, K.N. Sato, J.R.A. Taylor, J. McKittrick, A Protocol for Bioinspired Design: A Ground Sampler Based on Sea Urchin Jaws, Jove-Journal of Visualized Experiments (110) (2016) 1-8.

[29] N. Werkheiser, R. Mueller, Space Technology Game Changing Development: Additive Construction with Mobile Emplacement (ACME), NASA Facts (2015).

[30] P.J. Boston, M.V. Ivanov, C.P. McKay, ON THE POSSIBILITY OF CHEMOSYNTHETIC ECOSYSTEMS IN SUBSURFACE HABITATS ON MARS, Icarus 95(2) (1992) 300-308.

[31] A. Daga, C. Allen, M.M. Battler, J.D. Burke, I.A. Crawford, R.J. Léveillé, S.B. Simon, L.T. Tan, Lunar and Martian Lava Tube Exploration as Part of an Overall Scientific Survey, Annual Meeting of Lunar Exploration Analysis Group (LEAG) (2009).

[32] Honeybee Robotics: Pipe Inspection Robot, https://www.honeybeerobotics.com/portfolio/pipe-inspection-robot/.

[33] Xploration Station: Nature Knows Best, http://www.xplorationstation.com/show/Xploration-Nature-Knows-Best.

[34] Shark Wheel: The Difference, https://sharkwheel.com/the-difference/.

[35] S. Deville, Freezing Colloids: Observations, Principles, Control, and Use, Springer International Publishing2017.

[36] S.E. Naleway, Thesis: Harnessing Biology for Bioinspired Structural Materials with Intrinsic and Extrinsic Freeze Casting, Materials Science and Engineering Program, University of California, San Diego, 2016, p. 215.

[37] J.L. Kirschvink, J.L. Gould, Biogenic magnetite as a basis for magnetic-field detection in animals, Biosystems 13(3) (1981) 181-201.

[38] A.J. Kalmijn, I.F. Gonzalez, M.C. McClune, The physical nature of life, Journal of Physiology-Paris 96(5-6) (2002) 355-362.

[39] C. Walcott, R.P. Green, Orientation of homing pigeons altered by a change in direction of an applied magnetic-field, Science 184(4133) (1974) 180-182.

[40] J.L. Gould, J.L. Kirschvink, K.S. Deffeyes, Bees have magnetic remanence, Science 201(4360) (1978) 1026-1028.

[41] J.L. Kirschvink, A. Kobayashikirschvink, B.J. Woodford, Magnetite biomineralization in the human brain, Proc. Natl. Acad. Sci. U. S. A. 89(16) (1992) 7683-7687.

[42] R. Blakemore, Magnetotactic bacteria, Science 190(4212) (1975) 377-379.

[43] K. Inoue, K. Sassa, Y. Yokogawa, Y. Sakka, M. Okido, S. Asai, Control of crystal orientation of hydroxyapatite by imposition of a high magnetic field, Mater. Trans. 44(6) (2003) 1133-1137.

[44] S.H. Lee, L. Feng, J. Yin, J.S. Lee, X. Zhu, T.S. Suzuki, Y. Sakka, H. Tanaka, Dense SiC containing strongly aligned plate-like grains by magnetic treatment, Ceram. Int. 41(3) (2015) 5079-5084.

[45] M. Ozen, M. Mertens, F. Snijkers, G. Van Tendeloo, P. Cool, Texturing of hydrothermally synthesized BaTiO3 in a strong magnetic field by slip casting, Ceram. Int. 42(4) (2016) 5382-5390.

[46] Y. Sakka, T.S. Suzuki, Textured development of feeble magnetic ceramics by colloidal processing under high magnetic field, J. Ceram. Soc. Jpn. 113(1313) (2005) 26-36.

[47] T.S. Suzuki, Y. Sakka, Fabrication of textured titania by slip casting in a high magnetic field followed by heating, Jpn. J. Appl. Phys. Part 2 - Lett. 41(11A) (2002) L1272-L1274.

[48] T.S. Suzuki, Y. Sakka, Control of texture in ZnO by slip casting in a strong magnetic field and heating, Chem. Lett. (12) (2002) 1204-1205.

[49] T.S. Suzuki, T. Uchikoshi, Y. Sakka, Control of texture in alumina by colloidal processing in a strong magnetic field, Sci. Technol. Adv. Mater. 7(4) (2006) 356-364.

[50] D. Vriami, E. Beaugnon, J.P. Erauw, J. Vleugels, O. Van der Biest, Texturing of 3Y-TZP zirconia by slip casting in a high magnetic field of 17.4T, J. Eur. Ceram. Soc. 35(14) (2015) 3959-3967.

[51] Z.G. Yang, J.B. Yu, C.J. Li, Y.B. Zhong, W.D. Xuan, Z.M. Ren, Q.L. Wang, Y.M. Dai, H. Wang, Preparation of textured porous Al2O3 ceramics by slip casting in a strong magnetic field and its mechanical properties, Cryst. Res. Technol. 50(8) (2015) 645-653.

[52] H. Le Ferrand, F. Bouville, T.P. Niebel, A.R. Studart, Magnetically assisted slip casting of bioinspired heterogeneous composites, Nature Materials 14(11) (2015) 1172-+.

[53] R.M. Erb, K.H. Cherenack, R.E. Stahel, R. Libanori, T. Kinkeldei, N. Munzenrieder, G. Troster, A.R. Studart, Locally reinforced polymer-based composites for elastic electronics, ACS Appl Mater Interfaces 4(6) (2012) 2860-4.

[54] R. Libanori, R.M. Erb, A.R. Studart, Mechanics of Platelet-Reinforced Composites Assembled Using Mechanical and Magnetic Stimuli, Acs Applied Materials & Interfaces 5(21) (2013) 10794-10805.

[55] D. Carnelli, R. Libanori, B. Feichtenschlager, L. Nicoleau, G. Albrecht, A.R. Studart, Cement-based composites reinforced with localized and magnetically oriented Al2O3 microplatelets, Cement and Concrete Research 78 (2015) 245-251.

[56] R.M. Erb, J.S. Sander, R. Grisch, A.R. Studart, Self-shaping composites with programmable bioinspired microstructures, Nat Commun 4 (2013) 1712.

[57] R. Libanori, F.B. Reusch, R.M. Erb, A.R. Studart, Ultrahigh magnetically responsive microplatelets with tunable fluorescence emission, Langmuir 29(47) (2013) 14674-80.

[58] D. Kokkinis, M. Schaffner, A.R. Studart, Multimaterial magnetically assisted 3D printing of composite materials, Nature Communications 6 (2015) 10.

[59] J.J. Martin, B.E. Fiore, R.M. Erb, Designing bioinspired composite reinforcement architectures via 3D magnetic printing, Nature Communications 6 (2015) 7.

[60] U.G.K. Wegst, H. Bai, E. Saiz, A.P. Tomsia, R.O. Ritchie, Bioinspired structural materials, Nature Materials 14(1) (2015) 23-36.

[61] S. Weiner, H.D. Wagner, The material bone: Structure mechanical function relations, Annual Review of Materials Science 28 (1998) 271-298.

[62] M.E. Launey, M.J. Buehler, R.O. Ritchie, On the Mechanistic Origins of Toughness in Bone, in: D.R. Clarke, M. Ruhle, F. Zok (Eds.), Annual Review of Materials Research, Vol 40, Annual Reviews, Palo Alto, 2010, pp. 25-53.

[63] R.M.V. Pidaparti, C.H. Turner, Cancellous bone architecture: Advantages of nonorthogonal trabecular alignment under multidirectional joint loading, Journal of Biomechanics 30(9) (1997) 979-983.

[64] H.F. Zhang, I. Hussain, M. Brust, M.F. Butler, S.P. Rannard, A.I. Cooper, Aligned two- and three-dimensional structures by directional freezing of polymers and nanoparticles, Nature Materials 4(10) (2005) 787-793.

[65] S. Deville, E. Saiz, R.K. Nalla, A.P. Tomsia, Freezing as a path to build complex composites, Science 311(5760) (2006) 515-8.

[66] U.G. Wegst, M. Schecter, A.E. Donius, P.M. Hunger, Biomaterials by freeze casting, Philos Trans A Math Phys Eng Sci 368(1917) (2010) 2099-121.

[67] P.M. Hunger, A.E. Donius, U.G. Wegst, Platelets self-assemble into porous nacre during freeze casting, J Mech Behav Biomed Mater 19 (2013) 87-93.

[68] P.M. Hunger, A.E. Donius, U.G.K. Wegst, Structure-property-processing correlations in freeze-cast composite scaffolds, Acta Biomater. 9(5) (2013) 6338-6348.

[69] S.E. Naleway, K.C. Fickas, Y.N. Maker, M.A. Meyers, J. McKittrick, Reproducibility of ZrO2-based freeze casting for biomaterials, Materials Science & Engineering C-Materials for Biological Applications 61 (2016) 105-112.

[70] K. Araki, J.W. Halloran, Porous ceramic bodies with interconnected pore channels by a novel freeze casting technique, Journal of the American Ceramic Society 88(5) (2005) 1108-1114.

[71] K. Araki, J.W. Halloran, Room-temperature freeze casting for ceramics with nonaqueous sublimable vehicles in the naphthalene-camphor eutectic system, Journal of the American Ceramic Society 87(11) (2004) 2014-2019.

[72] R. Guo, C.-A. Wang, A. Yang, Piezoelectric Properties of the 1-3 Type Porous Lead Zirconate Titanate Ceramics, Journal of the American Ceramic Society 94(6) (2011) 1794-1799.

[73] E. Munch, E. Saiz, A.P. Tomsia, S. Deville, Architectural Control of Freeze-Cast Ceramics Through Additives and Templating, Journal of the American Ceramic Society 92(7) (2009) 1534-1539.

[74] M.M. Porter, J. McKittrick, M.A. Meyers, Biomimetic Materials by Freeze Casting, Jom 65(6) (2013) 720-727.

[75] M.M. Porter, R. Imperio, M. Wen, M.A. Meyers, J. McKittrick, Bioinspired Scaffolds with Varying Pore Architectures and Mechanical Properties, Advanced Functional Materials 24(14) (2014) 1978-1987.

[76] S.E. Naleway, C.F. Yu, M.M. Porter, A. Sengupta, P.M. Iovine, M.A. Meyers, J. McKittrick, Bioinspired composites from freeze casting with clathrate hydrates, Materials & Design 71 (2015) 62-67.

[77] Y.F. Tang, S. Qiu, C. Wu, Q. Miao, K. Zhao, Freeze cast fabrication of porous ceramics using tert-butyl alcohol-water crystals as template, J. Eur. Ceram. Soc. 36(6) (2016) 1513-1518.

[78] C. Tallon, R. Moreno, M.I. Nieto, Shaping of porous alumina bodies by freeze casting, Adv. Appl. Ceram. 108(5) (2009) 307-313.

[79] Y.M. Tan, O. Cervantes, S. Nam, J.D. Molitoris, J.P. Hooper, Dynamic fragmentation of cellular, ice-templated alumina scaffolds, Journal of Applied Physics 119(2) (2016) 8.

[80] S.M. Miller, X. Xiao, K.T. Faber, Freeze-cast alumina pore networks: Effects of freezing conditions and dispersion medium, J. Eur. Ceram. Soc. 35(13) (2015) 3595-3605.

[81] F. Bouville, E. Portuguez, Y.F. Chang, G.L. Messing, A.J. Stevenson, E. Maire, L. Courtois, S. Deville, Templated Grain Growth in Macroporous Materials, Journal of the American Ceramic Society 97(6) (2014) 1736-1742.

[82] F. Bouville, E. Maire, S. Meille, B. Van de Moortele, A.J. Stevenson, S. Deville, Strong, tough and stiff bioinspired ceramics from brittle constituents, Nature Materials 13(5) (2014) 508-514.

[83] H. Bai, Y. Chen, B. Delattre, A.P. Tomsia, R.O. Ritchie, Bioinspired large-scale aligned porous materials assembled with dual temperature gradients, Science advances 1(11) (2015) e1500849.

[84] H. Bai, F. Walsh, B. Gludovatz, B. Delattre, C.L. Huang, Y. Chen, A.P. Tomsia, R.O. Ritchie, Bioinspired Hydroxyapatite/Poly(methyl methacrylate) Composite with a Nacre-Mimetic Architecture by a Bidirectional Freezing Method, Advanced Materials 28(1) (2016) 50-56.

[85] A.H. Lu, E.L. Salabas, F. Schuth, Magnetic nanoparticles: synthesis, protection, functionalization, and application, Angew Chem Int Ed Engl 46(8) (2007) 1222-44.

[86] A.A. Neurauter, M. Bonyhadi, E. Lien, L. Nokleby, E. Ruud, S. Camacho, T. Aarvak, Cell isolation and expansion using Dynabeads((R)), in: A. Kumar, I.Y. Galaev, B. Mattiasson (Eds.), Cell Separation: Fundamentals, Analytical and Preparative Methods, Springer-Verlag Berlin, Berlin, 2007, pp. 41-73.

[87] M.R.S. McPhail, Jacob A.; He, Zhen; Chusei, Cahrles C., Charging Nanowalls: Adjusting the Carbon Nanotube Isoelectric Point via Surface Functionalization, J Phys Chem C 113 (2009) 14102-14109.

[88] G.E.H. Brown Jr., Victor E.; Casey, William H.; Clark, David L.; Eggleston, Carrick; Felmy, Andrew; Goodman, D. Wayne; Gratzel, Michael; Maciel, Gary; McCarthy, Maureen I.; Nealson, Kenneth H.; Sverjensky, Dimitri A.; Toney, Michael F.; Zachara, REVIEW: Metal Oxide Surfaces and Their Interactions with Aqueous Solutions and Microbial Organisms, Chemical Reviews 99 (1999) 77-174.

[89] M. Kosmulski, pH-dependent surface charging and points of zero charge. IV. Update and new approach, J Colloid Interface Sci 337(2) (2009) 439-48.

[90] A.P. Philipse, D. Maas, Magnetic colloids from magnetotactic bacteria: Chain formation and colloidal stability, Langmuir 18(25) (2002) 9977-9984.

[91] J.S. Andreu, J. Camacho, J. Faraudo, Aggregation of superparamagnetic colloids in magnetic fields: the quest for the equilibrium state, Soft Matter 7(6) (2011) 2336-2339.

[92] J. Faraudo, J.S. Andreu, J. Camacho, Understanding diluted dispersions of superparamagnetic particles under strong magnetic fields: a review of concepts, theory and simulations, Soft Matter 9(29) (2013) 6654-6664.

[93] P. Liu, J.W.J. de Folter, A.V. Petukhov, A.P. Philipse, Reconfigurable assembly of superparamagnetic colloids confined in thermo-reversible microtubes, Soft Matter 11(31) (2015) 6201-6211.

[94] J. Faraudo, J.S. Andreu, C. Calero, J. Camacho, Predicting the Self-Assembly of Superparamagnetic Colloids under Magnetic Fields, Advanced Functional Materials 26(22) (2016) 3837-3858.

[95] A.R. Studart, Biologically Inspired Dynamic Material Systems, Angewandte Chemie-International Edition 54(11) (2015) 3400-3416.

[96] D. Ghosh, M. Banda, H. Kang, N. Dhavale, Platelets-induced stiffening and strengthening of ice-templated highly porous alumina scaffolds, Scr. Mater. 125 (2016) 29-33.

[97] O.A. Graeve, A. Madadi, R. Kanakala, K. Sinha, Analysis of Particle and Crystallite Size in Tungsten Nanopowder Synthesis, Metall. Mater. Trans. A-Phys. Metall. Mater. Sci. 41A(10) (2010) 2691-2697.

[98] O.A. Graeve, H. Fathi, J.P. Kelly, M.S. Saterlie, K. Sinha, G. Rojas-George, R. Kanakala, D.R. Brown, E.A. Lopez, Reverse micelle synthesis of oxide nanopowders: Mechanisms of precipitate formation and agglomeration effects, Journal of Colloid and Interface Science 407 (2013) 302-309.

[99] C.I. Vargas-Consuelos, K. Seo, M. Camacho-Lopez, O.A. Graeve, Correlation between Particle Size and Raman Vibrations in WO3 Powders, J. Phys. Chem. C 118(18) (2014) 9531-9537.

[100] T.M. Nocera, J. Chen, C.B. Murray, G. Agarwal, Magnetic anisotropy considerations in magnetic force microscopy studies of single superparamagnetic nanoparticles, Nanotechnology 23(49) (2012) 495704.

[101] D.X. Chen, A. Sanchez, E. Taboada, A. Roig, N. Sun, H.C. Gu, Size determination of superparamagnetic nanoparticles from magnetization curve, Journal of Applied Physics 105(8) (2009) 6.

[102] H. Wang, Q.W. Chen, L.X. Sun, H.P. Qi, X. Yang, S. Zhou, J. Xiong, Magnetic-Field-Induced Formation of One-Dimensional Magnetite Nanochains, Langmuir 25(12) (2009) 7135-7139.

[103] M. Fitzner, G.C. Sosso, S.J. Cox, A. Michaelides, The Many Faces of Heterogeneous Ice Nucleation: Interplay Between Surface Morphology and Hydrophobicity, J. Am. Chem. Soc. 137(42) (2015) 13658-13669.

[104] S.J. Cox, S.M. Kathmann, B. Slater, A. Michaelides, Molecular simulations of heterogeneous ice nucleation. I. Controlling ice nucleation through surface hydrophilicity, J. Chem. Phys. 142(18) (2015) 5.

[105] K. Higashitani, K. Okuhara, S. Hatade, Effects of magnetic fields on stability of nonmagnetic ultrafine colloidal particles, Journal of Colloid and Interface Science 152(1) (1992) 125-131.

[106] X.-F. Pang, B. Deng, The changes of macroscopic features and microscopic structures of water under influence of magnetic field, Physica B: Condensed Matter 403(19–20) (2008) 3571-3577.

[107] R. Cai, H. Yang, J. He, W. Zhu, The effects of magnetic fields on water molecular hydrogen bonds, Journal of Molecular Structure 938(1–3) (2009) 15-19.

[108] S. Deville, E. Maire, A. Lasalle, A. Bogner, C. Gauthier, J. Leloup, C. Guizard, Influence of Particle Size on Ice Nucleation and Growth During the Ice-Templating Process, Journal of the American Ceramic Society 93(9) (2010) 2507-2510.

[109] T. Takenaka, K. Sakata, Grain orientation and electrical properties of hot forged Bi4Ti3O12 ceramics, Japanese Journal of Applied Physics 19(1) (1980) 31-39.

[110] Y. Yoshizawa, M. Toriyama, S. Kanzaki, Fabrication of textured alumina by high-temperature deformation, Journal of the American Ceramic Society 84(6) (2001) 1392-1394.

[111] T.S. Suzuki, Y. Miwa, S. Kawada, M. Kimura, T. Uchikoshi, Y. Sakka, Two-Dimensional Orientation in Bi4Ti3O12 Prepared Using Platelet Particles and a Magnetic Field, Journal of the American Ceramic Society 96(4) (2013) 1085-1089.

[112] W.W. Wu, Y. Sakka, T.S. Suzuki, G.J. Zhang, Microstructure and Anisotropic Properties of Textured ZrB2 and ZrB2-MoSi2 Ceramics Prepared by Strong Magnetic Field Alignment, Int. J. Appl. Ceram. Technol. 11(2) (2014) 218-227.

[113] D. Vriami, D. Damjanovic, J. Vleugels, O. Van der Biest, Textured BaTiO3 by templated grain growth and electrophoretic deposition, Journal of Materials Science 50(24) (2015) 7896-7907.

[114] L. Zhang, J. Vleugels, O. Van der Biest, Fabrication of textured alumina by orienting template particles during electrophoretic deposition, J. Eur. Ceram. Soc. 30(5) (2010) 1195-1202.

[115] H. Amorin, A.L. Kholkin, M.E.V. Costa, Templated grain growth of SrBi2Ta2O9 ceramics: Mechanism of texture development, Mater. Res. Bull. 43(6) (2008) 1412-1419.

[116] Y.F. Chang, S. Poterala, D. Yener, G.L. Messing, Fabrication of Highly Textured Fine-Grained alpha-Alumina by Templated Grain Growth of Nanoscale Precursors, Journal of the American Ceramic Society 96(5) (2013) 1390-1397.

[117] P.W. Hall, J.S. Swinnea, D. Kovar, Fracture resistance of highly textured alumina, Journal of the American Ceramic Society 84(7) (2001) 1514-1520.

[118] Y.M. Kan, P.L. Wang, Y.X. Li, Y.B. Cheng, D.S. Yan, Fabrication of textured bismuth titanate by templated grain growth using aqueous tape casting, J. Eur. Ceram. Soc. 23(12) (2003) 2163-2169.

[119] I.O. Ozer, E. Suvaci, B. Karademir, J.M. Missiaen, C.P. Carry, D. Bouvard, Anisotropic sintering shrinkage in alumina ceramics containing oriented platelets, Journal of the American Ceramic Society 89(6) (2006) 1972-1976.

[120] Y.K. Paek, E. Suvaci, G.L. Messing, Preparation and fracture behavior of alumina platelet reinforced alumina-monazite composites, Mater. Trans. 43(12) (2002) 3262-3265.

[121] M.M. Seabaugh, I.H. Kerscht, G.L. Messing, Texture development by templated grain growth in liquid-phase-sintered alpha-alumina, Journal of the American Ceramic Society 80(5) (1997) 1181-1188.

[122] M.D. Snel, J. van Hoolst, A.M. de Wilde, M. Mertens, F. Snijkers, J. Luyten, Influence of tape cast parameters on texture formation in alumina by templated grain growth, J. Eur. Ceram. Soc. 29(13) (2009) 2757-2763.

[123] E. Suvaci, M.M. Seabaugh, G.L. Messing, Reaction-based processing of textured alumina by templated grain growth, J. Eur. Ceram. Soc. 19(13-14) (1999) 2465-2474.

[124] K. Takatori, H. Kadoura, H. Matsuo, S. Arakawa, T. Tani, Microstructural evolution of high purity alumina ceramics prepared by a templated grain growth method, J. Ceram. Soc. Jpn. 124(4) (2016) 432-441.

[125] M. Wei, D. Zhi, D.G. Brandon, Microstructure and texture evolution in gel-cast alpha-alumina/alumina platelet ceramic composites, Scr. Mater. 53(12) (2005) 1327-1332.

[126] T. Carisey, A. Laugierwerth, D.G. Brandon, Control of texture in Al2O3 by gel casting, J. Eur. Ceram. Soc. 15(1) (1995) 1-8.

[127] T. Carisey, I. Levin, D.G. Brandon, Microstructure and mechanical properties of textured Al2O3, J. Eur. Ceram. Soc. 15(4) (1995) 283-289.

[128] M.T. Abba, P.M. Hunger, S.R. Kalidindi, U.G.K. Wegst, Nacre-like hybrid films: Structure, properties, and the effect of relative humidity, J. Mech. Behav. Biomed. Mater. 55 (2016) 140-150.

[129] T.P. Niebel, D. Carnelli, M.R. Binelli, R. Libanori, A.R. Studart, Hierarchically roughened microplatelets enhance the strength and ductility of nacre-inspired composites, J. Mech. Behav. Biomed. Mater. 60 (2016) 367-377.

[130] A.R. Studart, U.T. Gonzenbach, E. Tervoort, L.J. Gauckler, Processing routes to macroporous ceramics: A review, Journal of the American Ceramic Society 89(6) (2006) 1771-1789.

[131] M. Kamperman, A. Burns, R. Weissgraeber, N. van Vegten, S.C. Warren, S.M. Gruner, A. Baiker, U. Wiesner, Integrating Structure Control over Multiple Length Scales in Porous High Temperature Ceramics with Functional Platinum Nanoparticles, Nano Letters 9(7) (2009) 2756-2762.

[132] Z.C. Eckel, C.Y. Zhou, J.H. Martin, A.J. Jacobsen, W.B. Carter, T.A. Schaedler, 3D printing additive manufacturing of polymer-derived ceramics, Science 351(6268) (2016) 58-62.

[133] A.K. Plappally, I. Yakub, L.C. Brown, W.O. Soboyejo, A.B.O. Soboyejo, Physical Properties of Porous Clay Ceramic-Ware, J. Eng. Mater. Technol.-Trans. ASME 133(3) (2011) 9.

[134] M. du Preez, R.M. Conroy, J.A. Wright, S. Moyo, N. Potgieter, S.W. Gundry, Short Report: Use of Ceramic Water Filtration in the Prevention of Diarrheal Disease: A Randomized Controlled Trial in Rural South Africa and Zimbabwe, Am. J. Trop. Med. Hyg. 79(5) (2008) 696-701.

[135] V.A. Oyanedel-Craver, J.A. Smith, Sustainable colloidal-silver-impregnated ceramic filter for point-of-use water treatment, Environ. Sci. Technol. 42(3) (2008) 927-933.

[136] A.W. Smith, (inventor), Boeing, (assignee), Process for producing an anodic aluminum oxide membrane, U.S. patent 3,850,762 (1974 Nov 26).

[137] K.C. Popat, G. Mor, C. Grimes, T.A. Desai, Poly (ethylene glycol) grafted nanoporous alumina membranes, J. Membr. Sci. 243(1-2) (2004) 97-106.

[138] D. Ghosh, N. Dhavale, M. Banda, H. Kang, A comparison of microstructure and uniaxial compressive response of ice-templated alumina scaffolds fabricated from two different particle sizes, Ceram. Int. 42(14) (2016) 16138-16147.

[139] F. Bouville, E. Maire, S. Deville, Self-Assembly of Faceted Particles Triggered by a Moving Ice Front, Langmuir 30(29) (2014) 8656-8663.

[140] D. Ghosh, H. Kang, M. Banda, V. Kamaha, Influence of anisotropic grains (platelets) on the microstructure and uniaxial compressive response of ice-templated sintered alumina scaffolds, Acta Mater. 125 (2017) 1-14.

[141] M.B. Frank, S.E. Naleway, T. Haroush, C.-H. Liu, S.H. Siu, J. Ng, I. Torres, A. Ismail, K. Karandikar, M.M. Porter, O.A. Graeve, J. McKittrick, Stiff, porous scaffolds from magnetized alumina particles aligned by magnetic freeze casting, Materials Science and Engineering: C 77 (2017) 484-492.

[142] J. Aizenberg, P. Fratzl, New Materials through Bioinspiration and Nanoscience, Advanced Functional Materials 23(36) (2013) 4398-4399.

[143] M. Saterlie, H. Sahin, B. Kavlicoglu, Y.M. Liu, O. Graeve, Particle size effects in the thermal conductivity enhancement of copper-based nanofluids, Nanoscale Res. Lett. 6 (2011) 7.

[144] M.S. Saterlie, H. Sahin, B. Kavlicoglu, Y.M. Liu, O.A. Graeve, Surfactant Effects on Dispersion Characteristics of Copper-Based Nanofluids: A Dynamic Light Scattering Study, Chemistry of Materials 24(17) (2012) 3299-3306.

[145] H. Fathi, J.P. Kelly, V.R. Vasquez, O.A. Graeve, Ionic Concentration Effects on Reverse Micelle Size and Stability: Implications for the Synthesis of Nanoparticles, Langmuir 28(25) (2012) 9267-9274.

[146] J.T. Cahill, J.N. Ruppert, B. Wallis, Y.M. Liu, O.A. Graeve, Development of Mesoporosity in Scandia-Stabilized Zirconia: Particle Size, Solvent, and Calcination Effects, Langmuir 30(19) (2014) 5585-5591.

[147] V. Naglieri, H.A. Bale, B. Gludovatz, A.P. Tomsia, R.O. Ritchie, On the development of ice-templated silicon carbide scaffolds for nature-inspired structural materials, Acta Mater. 61(18) (2013) 6948-6957.

[148] P. Bowen, J. Sheng, N. Jongen, Particle size distribution measurement of anisotropic-particles cylinders and platelets - practical examples, Powder Technol. 128(2-3) (2002) 256-261.

[149] O. Hayakawa, K. Nakahira, M. Naito, J. Tsubaki, Experimental analysis of sample preparation conditions for particle size measurement, Powder Technol. 100(1) (1998) 61-68.

[150] B. Willie, G.N. Duda, R. Weinkamer, Bone Structural Adaptation and Wolff's Law, in: P. Fratzl, J.W.C. Dunlop, R. Weinkamer (Eds.), Materials Design Inspired by Nature: Function through Inner Architecture, Royal Soc Chemistry, Cambridge, 2013, pp. 17-45.

[151] R. Huiskes, If bone is the answer, then what is the question?, J. Anat. 197 (2000) 145-156.

[152] Y. Li, B.R. Ellingwood, Reliability of woodframe residential construction subjected to earthquakes, Struct. Saf. 29(4) (2007) 294-307.

[153] Y. Li, Y.J. Yin, B.R. Ellingwood, W.M. Bulleit, Uniform hazard versus uniform risk bases for performance-based earthquake engineering of light-frame wood construction, Earthq. Eng. Struct. Dyn. 39(11) (2010) 1199-1217.

[154] J.W. van de Lindt, Damage-based seismic reliability concept for woodframe structures, J. Struct. Eng.-ASCE 131(4) (2005) 668-675.

[155] S.L. Chen, C.M. Fan, J.L. Pan, Experimental Study on Full-Scale Light Frame Wood House under Lateral Load, J. Struct. Eng.-ASCE 136(7) (2010) 805-812.

[156] National Osteoporosis Foundation, https://www.nof.org/.

[157] Transitions Health and Fitness, http://www.transitionshealthandfitness.com.au/blog/01-healthy-bones-vs-osteoporosis.

[158] Bone Mass Measurement: What the Numbers Mean, https://www.niams.nih.gov/Health_Info/Bone/Bone_Health/bone_mass_measure.asp.

[159] University of Cambridge: Dissemination of IT for the Promotion of Materials Science (DoITPoMS), https://www.doitpoms.ac.uk/tlplib/bones/printall.php.

[160] X. Li, Y.-F. Feng, C.-T. Wang, G.-C. Li, W. Lei, Z.-Y. Zhang, L. Wang, Evaluation of Biological Properties of Electron Beam Melted Ti6Al4V Implant with Biomimetic Coating In Vitro and In Vivo, PLOS ONE 7(12) (2012) e52049.

[161] O.A. Tertuliano, J.R. Greer, The nanocomposite nature of bone drives its strength and damage resistance, Nature Materials 15(11) (2016) 1195-+.

[162] M.B. Frank, S. Hei Siu, K. Karandikar, C.-H. Liu, S.E. Naleway, M.M. Porter, O.A. Graeve, J. McKittrick, Synergistic structures from magnetic freeze casting with surface magnetized alumina particles and platelets, J. Mech. Behav. Biomed. Mater. (2017).

[163] W. Yang, C. Chao, J. McKittrick, Axial compression of a hollow cylinder filled with foam: A study of porcupine quills, Acta Biomater. 9(2) (2013) 5297-5304.

[164] W. Yang, J. McKittrick, Separating the influence of the cortex and foam on the mechanical properties of porcupine quills, Acta Biomater 9(11) (2013) 9065-74.

[165] Dogs and Porcupines, http://dogtime.com/dog-health/dog-behavior/18243-dogs-and-porcupines.

[166] Quora: What are biodegradable and non-biodegradable materials with examples?, https://www.quora.com/What-are-biodegradable-and-non-biodegradable-materials-with-examples.

[167] J.P. Gong, Y. Katsuyama, T. Kurokawa, Y. Osada, Double-network hydrogels with extremely high mechanical strength, Advanced Materials 15(14) (2003) 1155-+.

[168] J.Y. Sun, X.H. Zhao, W.R.K. Illeperuma, O. Chaudhuri, K.H. Oh, D.J. Mooney, J.J. Vlassak, Z.G. Suo, Highly stretchable and tough hydrogels, Nature 489(7414) (2012) 133-136.

[169] W. Yang, V.R. Sherman, B. Gludovatz, E. Schaible, P. Stewart, R.O. Ritchie, M.A. Meyers, On the tear resistance of skin, Nature Communications 6 (2015) 10.

[170] Wikipedia: Ceramic Water Filter, https://en.wikipedia.org/wiki/Ceramic_water_filter.

[171] Potters for Peace: Ceramic Water Filter Project, http://pottersforpeace.com/?page_id=63.

[172] Monolithic: Ceramic Water Filter, https://www.monolithicmarketplace.com/products/just-water-ceramic-drip-filter.

[173] NANOCERAM FILTERS Presentation, http://www.premium-water-filters.com/pdf/NanoCeram_Presentation_Argonide.pdf.

[174] NASA Environmental and Agricultural Resources Spinoff 2009: Nanofiber Filters Eliminate Contaminants, https://www.nasa.gov/pdf/413408main_Nanofiber.pdf.

[175] Argonide Corporation: Advances in Filtration Technology, http://slideplayer.com/slide/1677293/.

[176] J.B. Messenger, Cephalopod chromatophores: neurobiology and natural history, Biol. Rev. 76(4) (2001) 473-528.

[177] Monterey Bay Aquarium: Flamboyant Cuttlefish, https://www.montereybayaquarium.org/animal-guide/octopuses-and-kin/flamboyant-cuttlefish.

[178] You Shouldn't Eat That: Flamboyant Cuttlefish, http://myths-made-real.blogspot.com/2014/11/you-shouldnt-eat-that-flamboyant.html.